Constraining the Neutrino Mass Using Cyclotron Radiation Emission Spectroscopy

Ali Ashtari Esfahani

A dissertation
submitted in partial fulfillment of the
requirements for the degree of

Doctor of Philosophy

University of Washington

2020

Reading Committee:

Gray Rybka, Chair

R.G. Hamish Robertson

Alejandro Garcia

Program Authorized to Offer Degree:
Physics

University of Washington

Abstract

Constraining the Neutrino Mass Using Cyclotron Radiation Emission Spectroscopy

Ali Ashtari Esfahani

Chair of the Supervisory Committee:
Professor Gray Rybka
Physics Department

The existing prototype to demonstrate the viability of the Cyclotron Radiation Emission Spectroscopy (CRES) has been upgraded to incorporate tritium compatibility. The spectrum of the conversion electrons from ^{83m}Kr has been measured with great linearity and a precision of 2 eV over the energy range of 17−32. The first tritium beta-spectrum using CRES has also been measured to conclude an endpoint value of $E_0 = 18574.1 \pm (17.2)_{stat.} + \binom{+12.5}{-21.1}_{sys.}\ eV$. The recorded tritium spectrum is analyzed to set the first CRES limit on the neutrino mass, $m_\beta\ < 146\ eV\ \ (90\%\ C.L.)$.

TABLE OF CONTENTS

LIST OF FIGURES

ACKNOWLEDGMENTS

First and foremost I have to express my sincere gratitude to my advisor Gray Rybka for his continued support and encouragement during my time at University of Washington. I should also gratefully acknowledge Hamish Robertson for his guidance in this project and his influence on shaping my scientific personality.

During my time in Project 8, I had the privilege to work alongside great physicists from whom I learned a great deal. Martin Fertl, Mathieu Guigue, Walter Pettus, and Elise Novitski I thank you all for your help and mentorship. I should also thank my colleague and friend Christine Claessens who has motivated many ideas in this work.

Finally, I thank the entire CENPA faculty, staff, and students for providing a nurturing environment for the pursue of the world-class research taking place at this center.

DEDICATION

For my father, Mostafa Ashtari Esfahani

Chapter 1

INTRODUCTION

Neutrino physics has been one of the driving forces in the progress of particle physics. From the study of solar model in astrophysics to the study of nucleus structure in Nuclear physics, neutrinos provide unique avenues for investigation of new physics.

What follows in this chapter is a brief historical background with the emphasis on the importance of the search for the neutrino mass. We then discuss the current efforts in the field of neutrino mass measurement. Finally we introduce the Cyclotron Radiation Emission Spectroscopy and discuss the phased plan proposed by the Project 8 collaboration to construct the next generation of the direct neutrino mass search experiments.

1.1 Historical Background

In 1914 Chadwick used a magnetic spectrometer to measure the energy spectrum of the beta decay[12]. The observed continuous spectrum stands in contrast to the discrete nature of the alpha and gamma decays. Later experiments confirmed that the electron carries a fraction of the released energy in the decay[17][36]. This led to the speculation that the energy conservation might fail in the microscopic realm.

In an attempt to preserve the energy conservation, Wolfgang Pauli postulated the existence of a neutral spin-half particle in a famous letter in 1930. This new particle (later named ”neutrino” by Enrico Fermi) would carry the missing energy and escape the detection.

Enrico Fermi formulated his theory of beta decay based on this postulation. He deduced the functional form of the beta decay with the neutrino mass as a free parameter. He showed that the effect of the neutrino mass is pronounced at higher energies where the neutrino is almost at rest (Fig. 1.1). The maximum energy of the electron in this case is

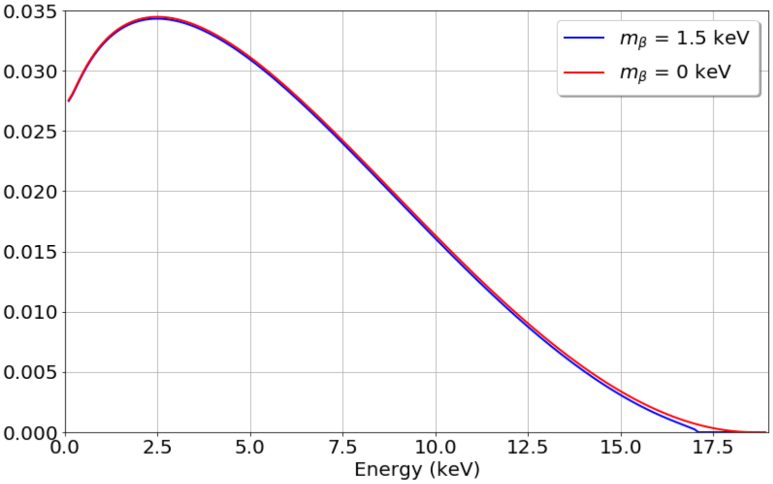

Figure 1.1: The effect of an exaggerated $m_\beta = 1.5$ keV on the tritium beta spectrum. The exact functional form used in this plot will be explained in Chapter 5.

$E_{max} = Q - m_e - m_\nu - E_{rec}$, where Q is the released energy in the decay process and E_{rec} is the recoil energy of the daughter nucleus.

The electron anti-neutrino was directly detected in 1953 by Cowan and Reines[51]. They used a 300 L tank of liquid scintillator to detect anti-neutrinos from the Hanford reactor. The detection technique was based on the

$$\overline{\nu}_e + p \longrightarrow e^+ + n \tag{1.1}$$

reaction. The measurement of the 511 keV photons from positron annihilation and the gamma rays from the neutron capture emitted a few microseconds later provided the signal for detecting the anti-neutrinos. The experiment was repeated in 1956 at the Savannah River reactor with 4200 L of liquid scintilator proving the existence of the neutrino particle [52]. The direct detection of muon and tau neutrinos in 1962 and 2001 completed the list of all known flavors of neutrinos[15][32].

Experimental measurements supported the case of mass-less neutrinos prior to the formation of the Standard model of particle physics. In this model neutrinos were three mass-less flavor states in correspondence to the three generations of the leptons. The surprising result of the Homestake experiment in the study of the solar neutrinos was the first in a series of experiments studying neutrinos from different sources which led to the discovery of the neutrino oscillation[13]. According to this model the neutrinos change their flavor state as they propagate in space. This is due to the fact that the neutrino mass states do not coincide with the flavor states. The detection of the neutrino oscillation of the atmospheric and solar neutrinos by Super-K and SNO experiments provided the ultimate proof for the neutrino oscillation conjecture[24][3].

The matrix which relates the mass and flavor states of neutrinos , Pontecorvo-Maki-Nakagawa- Sakata (PMNS) matrix, can be parameterized with three angles and a CP-violating phase,

$$\begin{bmatrix} \nu_e \\ \nu_\mu \\ \nu_\tau \end{bmatrix} = \begin{bmatrix} c_{12}c_{13} & s_{12}c_{13} & s_{13}e^{-i\delta_{\mathrm{CP}}} \\ -s_{12}c_{23} - c_{12}s_{23}s_{13}e^{i\delta_{\mathrm{CP}}} & c_{12}c_{23} - s_{12}s_{23}s_{13}e^{i\delta_{\mathrm{CP}}} & s_{23}c_{13} \\ s_{12}s_{23} - c_{12}c_{23}s_{13}e^{i\delta_{\mathrm{CP}}} & -c_{12}s_{23} - s_{12}c_{23}s_{13}e^{i\delta_{\mathrm{CP}}} & c_{23}c_{13} \end{bmatrix} \begin{bmatrix} \nu_1 \\ \nu_2 \\ \nu_3 \end{bmatrix}. \tag{1.2}$$

Where ν_1, ν_2, and ν_3 are the mass states and c_{ij} and S_{ij} are used to denote the $\cos\theta_{ij}$ and $\sin\theta_{ij}$. The current values of the three angles and the CP-violating phase are listed in Tbl. 1.1 [43].

The observation of the neutrino oscillation has proved the existence of at least two non-zero mass states for neutrinos. However the oscillation experiments are only sensitive to the difference between mass squared values (Tbl. 1.1). Moreover, two different mass ordering are possible for neutrinos due to the unknown sign of the Δm^2_{23}. The first scenario where the third neutrino mass state is the heaviest is named the normal ordering. In the other case the third neutrino mass state has the smallest value. This ordering is named the inverted mass ordering scenario. Furthermore, the oscillation experiments cannot be used for the absolute scale measurement of the neutrino mass. This search is an ongoing effort which we will review in the next section.

1.2 Neutrino Mass Measurements

One particular question of the neutrino physics with a long history in the past century is the measurement of the neutrino mass. Different areas of physics are sensitive to different

Parameter	Best fit	3σ
Δm^2_{21} $[10^{-5} eV^2]$	7.37	6.93 - 7.96
$\Delta m^2_{31(23)}$ $[10^{-3} eV^2]$	2.56 (2.54)	2.45 - 2.69 (2.42 - 2.66)
$\sin^2\theta_{12}$	0.297	0.250 - 0.354
$\sin^2\theta_{23}, \Delta m^2_{31(23)} > 0$	0.425	0.381 - 0.615
$\sin^2\theta_{23}, \Delta m^2_{31(23)} < 0$	0.589	0.384 - 0.636
$\sin^2\theta_{13}, \Delta m^2_{31(23)} > 0$	0.0215	0.0190 - 0.0240
$\sin^2\theta_{13}, \Delta m^2_{31(23)} < 0$	0.0216	0.0190 - 0.0242
δ_{CP}/π	1.38 (1.31)	2σ: (1.0 - 1.9) (2σ: (0.92 - 1.88))

Table 1.1: The best-fit values and 3σ allowed ranges of the 3-neutrino oscillation parameters, derived from a global fit of the current neutrino oscillation data. The values in parenthesis are corresponding to the inverted mass ordering scenario [43].

combinations of the mass states. In this section we briefly review the ongoing efforts.

Cosmological neutrinos have their mark on large structure formation in the universe. This signature can be investigated using cosmic microwave background, large structure of galaxy clusters, type Ia supernovae, and big bang nucleosynthesis data. These measurements are sensitive to the sum of mass states,

$$m_{tot} = \sum_{i=1,2,3} m_i. \tag{1.3}$$

One limit based on the combination of all available data is,

$$m_{tot} < 0.26\ meV/c^2\ (95\%\ C.L.)[41]. \tag{1.4}$$

It should be emphasised that this limit relies on the accuracy of the ΛCDM model of the universe.

The neutrinos from a supernova can also be utilized for a neutrino mass search. Measurements of the time of arrival and the energy of neutrinos lead to the determination of their mass. The detected neutrinos from SN 1987A conclude that

$$m_{\overline{\nu}_e} = \sqrt{\sum_{i=1,2,3} \left|U_{ei}\right|^2 m_i^2} < 5.7\ eV\ (95\%\ C.L.)\ [40]. \tag{1.5}$$

Another area of physics sensitive to the neutrino mass is the search for the beyond the Standard Model process of neutrino-less double beta decay. Detection of such an event proves the Majorana nature of the neutrino particles. This process if discovered is sensitive to,

$$m_{\beta\beta}^2 = \left|\sum_{i=1,2,3} U_{ei}^2 m_i\right|^2. \tag{1.6}$$

Currently the best limit is from the investigation of double beta decay in ^{136}Xe,

$$m_{\beta\beta} < 61 - 165\ meV/c^2\ (90\%\ C.L.)[25], \tag{1.7}$$

in which the range is due to the uncertainty in the nuclear matrix element. The search is also conducted using ^{130}Te and ^{76}Ge which resulted in independent limits[5][6][2]. In addition to the complexity introduced by the unknown nuclear matrix elements, this technique relies on the assumption that the neutrinos are Majorana fermions[1].

The direct search is another method for the search for the neutrino mass. Fig. 1.1 illustrates how a non-zero mass can reshape the electron's energy spectrum of the beta decay. The direct measurement of the neutrino mass is sensitive to the effective value,

$$m_\beta^2 = \sum_{i=1,2,3} \left|U_{ei}\right|^2 m_i^2. \tag{1.8}$$

This method only relies on the kinematics of the decay process and is therefore the most model independent technique for the neutrino mass measurement. This search can be carried via either the electron capture or the beta decay.

---

[1] Majorana fermion is a spin-half particle that is its own anti-particle.

Measurement of the electron capture on ^{163}Ho is one active area of research. The binding energy released by the capture of an electron increases the temperature of the detector which can be measured with different calorimeter detectors[26][27]. This method provides a measurement of the mass of the neutrinos in contrast with the beta decay measurement of the mass of anti-neutrino particle. Therefore these measurements along with the beta decay experiments can provide a test of CPT invariance.

Tritium is the most common element used in the direct search for the neutrino mass. This beta decay element with relatively low endpoint energy is historically used for putting the most stringent limits on the neutrino mass[10][11][42][56][34][7]. Currently, the KATRIN experiment has the best limit on the neutrino mass in the direct search where

$$m_\beta < 1.1\ eV/c^2\ (90\%\ C.L.)[4]. \tag{1.9}$$

The KATRIN collaboration utilizes the well-known MAC-E (Magnetic Adiabatic Collimation - Electrostatic) filter for measuring electron's energy. In this technique an electrostatic field is used to reflect low energy beta particles back to the source. An integral spectrum can be measured by altering this electrostatic field. However, an electric field is not enough for reaching a sufficient energy resolution. The reason lies in the fact that the electrons are emitted in different directions from the tritium nucleus. The electrostatic high-pass filter acts only on the longitudinal component of the electron energy and therefore electrons with larger transverse energy register as low energy electrons.

To solve this problem a magnetic field is added to the spectrometer. Electrons conserve their magnetic moment,

$$\mu = \frac{E_\perp}{B}, \tag{1.10}$$

in an adiabatically changing magnetic field. If the magnetic field decreases electron's transverse energy must decrease as well. The conservation of energy indicates that the decrease in the transverse part of the energy should cause an increase in the longitudinal energy of the electron. Hence the adiabatically decreasing magnetic field causes an energy transfer from the transverse to longitudinal components. The electrostatic field can now act on the

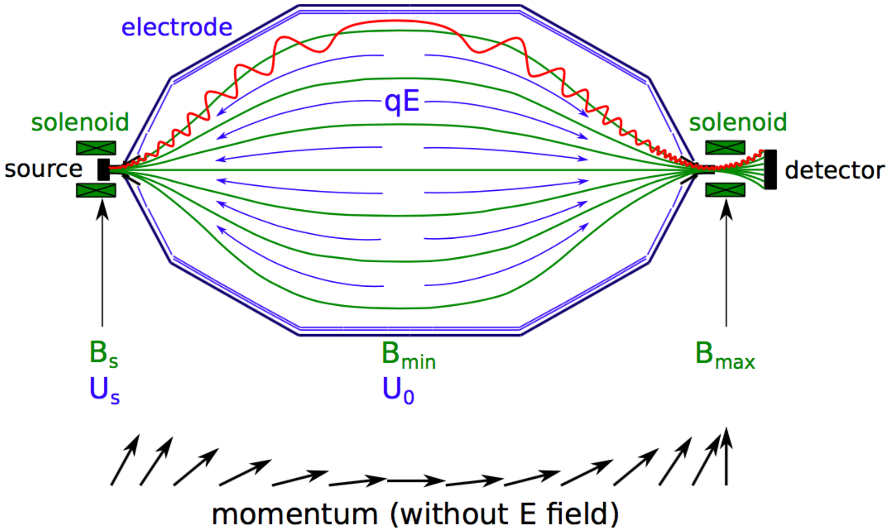

Figure 1.2: The basics of the KATRIN MAC-E filter. The magnetic field (shown in green) collimates the electron emitted at different directions from the source. The electric field (shown in blue) then reflects electrons with longitudinal energies less than qU_0 back to the source region. This figure is from [45].

collimated electrons and filter them solely based on their total energy. Fig. 1.2 shows the basics of the KATRIN MAC-E filter spectrometer.

The energy resolution of a MAC-E filter is,

$$\frac{\Delta E}{E} = \frac{B_{min}}{B_{max}}, \tag{1.11}$$

where the source and detector are placed in the maximum field region and the minimum magnetic field is placed at the center of the spectrometer. Achieving acceptable energy resolution therefore relies on a considerable difference in magnetic field. This difference forces a spatially extended spectrometer due to the conservation of the magnetic flux.

KATRIN's main spectrometer is a 23 m long vessel with a 10 m diameter which has a $\Delta E = 2.8\ eV$ energy resolution [4]. Construction and operation of this enormous spectrometer is a marvelous achievement for the KATRIN collaboration. KATRIN is projected to be sensitive to neutrino masses above 0.2 $\frac{eV}{c^2}$. The search for the neutrino mass beyond this limit demands the development of a new technique in the electron energy measurements. Project 8 collaboration proposing an alternative technique for measuring the electron energy which is going to be discussed in the next section.

1.3 Cyclotron Radiation Emission Spectroscopy (CRES)

Cyclotron Radiation Emission Spectroscopy is a technique for measuring relativistic electron's energy based on a proposal by Joseph Formaggio and Benjamin Monreal [44]. In this method the cyclotron frequency of an electron inside a magnetic field,

$$f_c = \frac{f_0}{\gamma} = \frac{1}{2\pi}\frac{eB}{m_e + K_e/c^2}, \tag{1.12}$$

is used for measuring its kinetic energy. In this equation f_0 is the non-relativistic cyclotron frequency, $\gamma = 1 + K_e/m_e c^2$ is the Lorentz factor, B is the magnetic field, and e, m_e, and K_e are electron's charge, mass, and kinetic energy. The cyclotron frequency is $\sim$ 26 GHz for the high-energy electrons of the tritium spectrum in a 1 T magnetic field.

This new technique has a number of advantages in comparison with the conventional MAC-E filter spectrometers. First, there is no need for transporting electrons from the decay region to the detector because the tritium gas is transparent to the cyclotron frequency of the radiation. Second, due to the recent advancements in the time measurement with the atomic clocks, the frequency is a quantity which can be measured with great precision. This accuracy can translate into excellent energy resolutions in any CRES-type experiment. Third, this method provides a simultaneous differential spectrum measurement which decreases the required running time and reduces the sensitivity of the measurement to the minor instabilities. Fourth, due to the availability of both temporal and frequential information, the pile-up is not a concern. Finally, any emitted electron from the surface of the experiment travels back to the surface before it can radiate enough power to be detected. Hence a low background is expected for the CRES-type experiments.

1.4 Project 8: A Phased Plan for the Neutrino Mass Measurement

The Project 8 collaboration is formed to utilize the cyclotron radiation emission spectroscopy for the search of the electron (anti)-neutrino mass in the full range allowed by the inverted mass hierarchy. To realize this goal a phased plan approach is deployed by the collaboration[21].

The first phase of the experiment demonstrated the viability of this technique by measuring the cyclotron radiation of the conversion electrons from ^{83m}Kr in a warm-bore superconductor NMR magnet[9]. This isotope of krypton is a proper source for testing the viability of the new technique because it provides mono-energetic electrons at 17.824 keV which is close to the tritium endpoint energy. The radiation is collected using a rectangular wave-guide in this phase.

Phase II of the experiment is where the first tritium spectrum is measured. For achieving this goal a number of upgrades has been done to the Phase-I detector. A new gas system also has been added to facilitate handling of the tritium gas. This phase is the main emphasis of this work.

The major upgrade in the Phase III is the use of antenna arrays for harvesting the free-space radiation from cyclotron electrons. This upgrade enables the collaboration to use a larger volume for acquiring more electron events. The projected sensitivity for this phase is $\sim 2\ eV/c^2$ which is planned to start data taking by 2022. The R&D efforts for this phase has already initiated. Fig. 1.3 shows a potential design with the patch antenna arrays and the trapping coils.

Ultimately, an atomic source of the tritium will be used in phase IV of the experiment. The molecular motions of the remaining molecules with the remaining He nucleus of the beta decay introduces systematic effects which can be avoided by employing atomic tritium. Fig. 1.4 illustrates the result of a study of the mass sensitivity of phase IV [2].

---

[2] This plot is the result of an analysis done by Hamish Robertson (rghr@uw.edu) and Talia Weiss (tweiss@mit.edu).

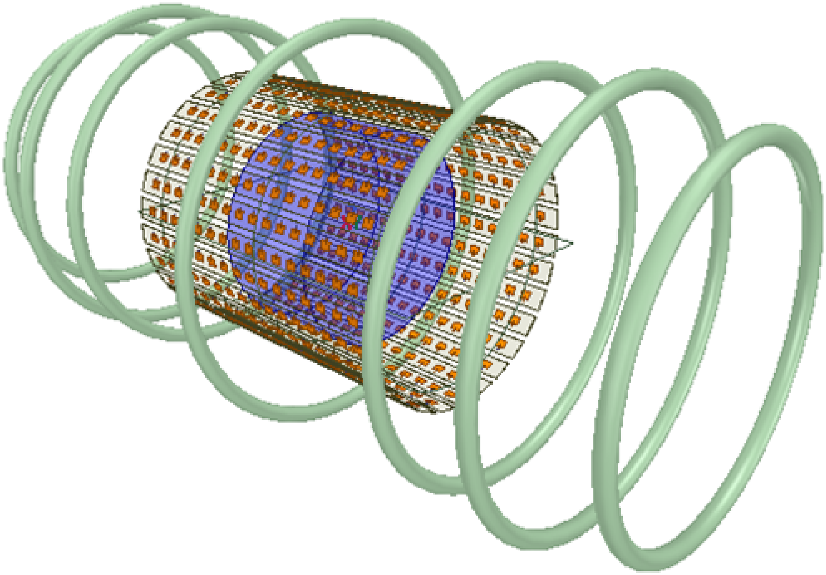

Figure 1.3: Potential design of the phase III with patch antenna arrays. The green rings are the trapping coils and the blue cylinder is the 200 cc gas cell.

The main topic of discussion in this dissertation is the design, construction, and data analysis of the second phase. In Chapter 2 we will briefly review the Phase-I apparatus and then explain in more details the upgrades done for the second phase of the experiment. Chapter 3 is devoted to the development of a phenomenological model for explaining the power spectrum of a CRES signal. This chapter will start with studying the electron motion and then concludes with the derivation of power spectral density of CRES radiation in a waveguide geometry. In Chapter 4 we will use this phenomenological model to analyze the krypton data taken as a calibration source. Finally, in Chapter 5 we will present the tritium spectrum recorded in the second phase of the experiment and the analysis leading to the first measurement of the tritium end-point energy and the derived constraint on the electron neutrino mass using the CRES technique.

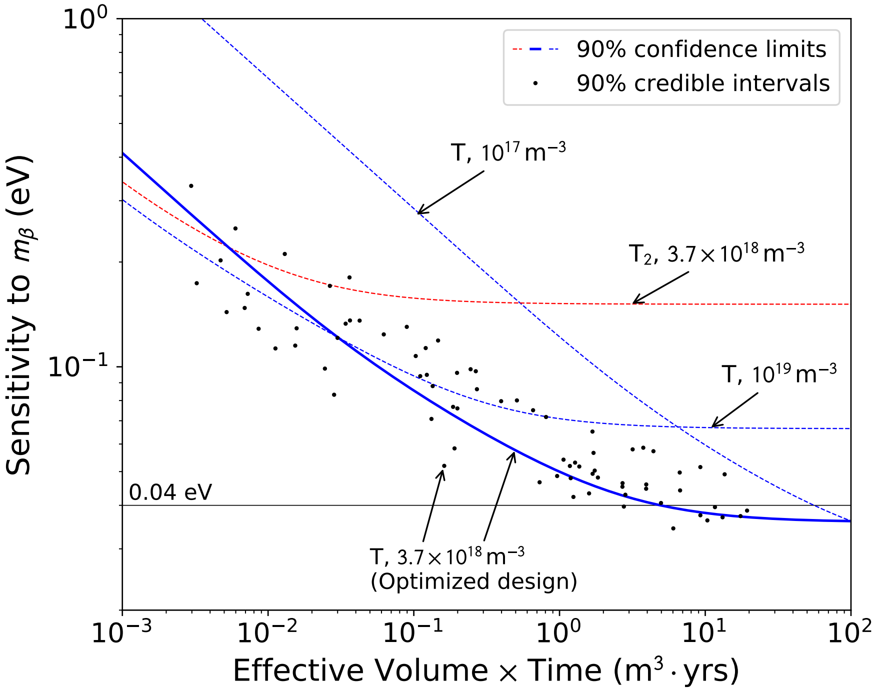

Figure 1.4: Sensitivity of the experiments with different densities of the molecular and atomic tritium. The horizontal line marks the design goal of project 8 collaboration. The lines are the result of an analytical calculation while the dots represent the outcomes of a Bayesian simulation.

Chapter 2

CRES DEMONSTRATOR APPARATUS

The apparatus for a CRES experiment includes four main sub-systems. First, a gas cell where the radioactive gas resides and emits electrons. Second, an RF receiver which receives, amplifies, digitizes, and records the emitted cyclotron power. Third, a gas system which feeds the gas cell with the right radioactive gas pressure and composition. Finally a magnet which produces the required background field for performing a CRES experiment.

In this chapter we briefly discuss the phase I design. Then we explain the phase II systems in more details and discuss the upgrades done by project 8 collaboration. A more detailed review of the phase I apparatus is presented in [33].

2.1 Magnet

The first two phases of Project 8 happened in a 200 MHz Bruker Spectrospin superconductor NMR magnet. The magnet coil is manufactured out of niobium-titanium alloy which acts as a superconductor below the critical temperature of 9.2 K. To maintain the superconducting state of the coil, it is submerged into a liquid helium bath. Since the liquid helium is an expensive cryogenic liquid, its boil-off is minimized by isolating it from room temperature by a reservoir of liquid nitrogen.

The magnet outline is shown in Fig. 2.1. It gets filled with liquid nitrogen twice a week. The liquid Helium gets recharged every seven to eight weeks.

Using the seven provided shimming coils, a 10 ppm-level homogeneity is achieved across the 52 mm diameter of the bore. A specifically designed NMR probe is used to map the field inside the magnet's bore. More details about the shimming and field homogeneity can be found in [33]. Fig. 2.2 shows a more recent measurement of magnetic field strength along

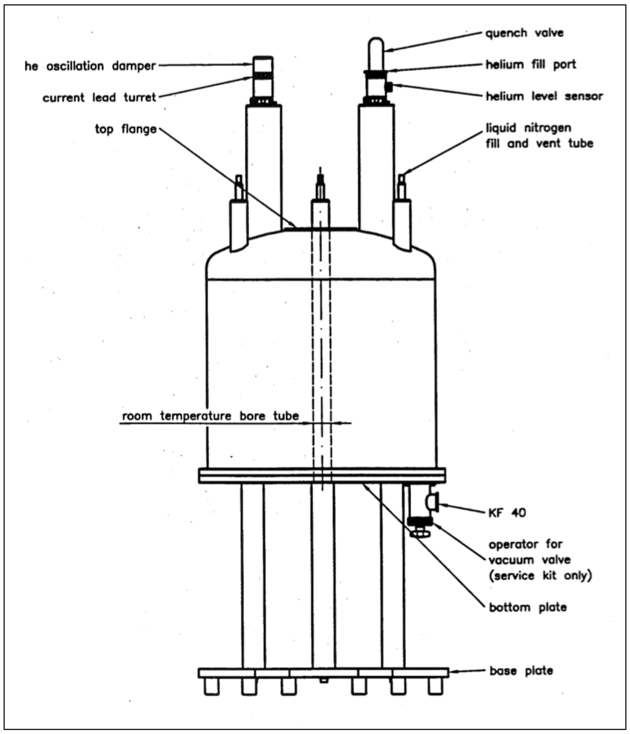

Figure 2.1: The 200 MHz spectrospin superconductor NMR magnet used in the first two phases of the Project 8.

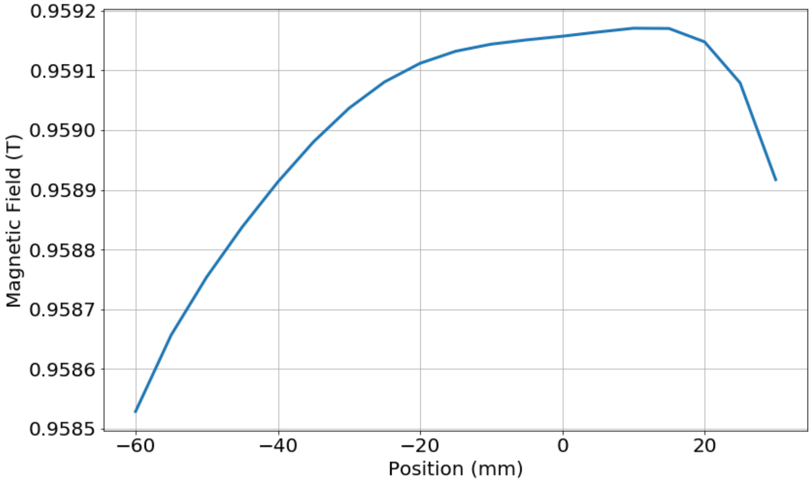

Figure 2.2: The magnetic field measurement at the center of the NMR magnet's bore, performed in April 2018.

the axis of the bore.

2.2 Gas Cell Design

The gas cell is the volume in which the radioactive decay happens. It confines the radioactive gas and transfers the radiated power from the cyclotron electrons to the receiver chain.

The design of the gas cell should satisfy a number of requirements. First, the cell should be an efficient microwave guide for the frequency region of interest. This necessity specifies the dimensions of the waveguide design. Second, the gas cell should be able to confine the radioactive gas inside the cell without disturbing its R.F. properties. Therefore a metallic waveguide design is chosen with the addition of two R.F. transparent windows at the two ends of the cell. The cell is built in room temperature and it should have the potential to be operational at hydrogen's boiling temperature[1]. And finally, the cell needs to be facilitated

---

[1] This is the lowest temperature that Project 8 can possibly measure a tritium spectrum at. At lower temperatures the tritium would liquefy and make it impossible to perform a CRES measurement.

with coils which can provide different magnetic bottle trap geometries. This need for a magnetic trap will be discussed in more details in section 2.2.3.

2.2.1 Wave-guide Design

The wave-guide design has to be optimized for electron energies in the range of 10 keV - 30 keV. These electrons radiate power in the K-band frequency range of microwave spectrum in the presence of a 1 T magnetic field. The k-band wavelength roughly defines cross sectional dimensions of the wave-guides to be 1 $cm - 2\ cm$.

The dimensions of the waveguide should be chosen with regard to a number of considerations. First, the volume of the waveguide directly affects the number of radioactive gas molecules in the cell at a given pressure and temperature. Therefore higher statistics can be achieved by designing a larger gas cell. However, increasing the cross sectional dimensions of a waveguide can introduce electron's coupling to non-fundamental modes in the wave-guide which will increase the complexity of the analysis. Increasing the length of the wave-guide is also not desirable due to the small region of constant field inside the NMR magnet's bore.

The other factor in deciding the right waveguide dimensions is the wave impedance[2]. The cyclotron electron can be seen as a fixed current source in the wave-guide. Therefore the radiated power from this source increases linearly with the wave impedance. Since the wave impedance increases in proximity of the cut-off frequency for TE modes in the wave-guide, selecting a cut-off frequency closer to the operational frequency might seem favorable. However, the wave attenuation also increases by picking a cut-off frequency close to the frequency range of interest (see Fig. 2.3).

With these regards, a WR-42 rectangular wave-guide is chosen for the first phase of the experiment. Fig. 2.4 displays the wave impedance for the first five modes of this wave-guide. The cut-off frequency for the fundamental mode is 14.051 GHz and the next mode emerges

---

[2] Wave impedance is defined as the ratio of the transverse component of the electric field to the transverse component of the magnetic field.

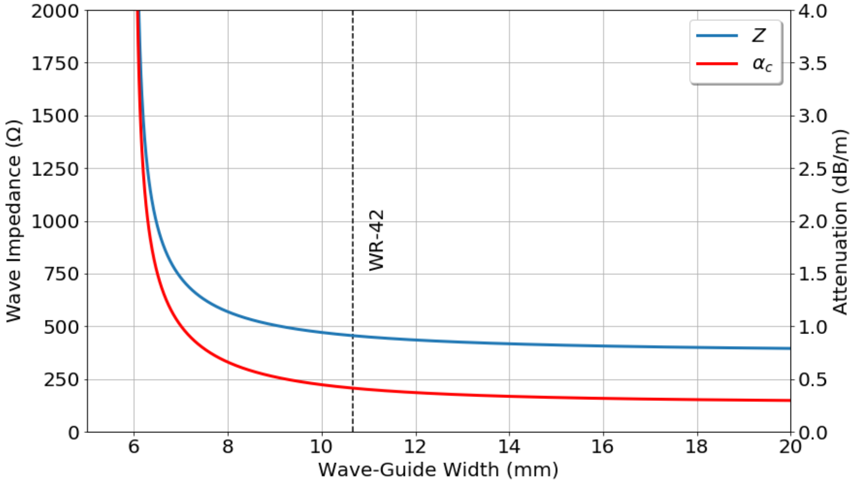

Figure 2.3: Wave impedance and attenuation at 25 GHz for the fundamental mode of a 0.17 inch high wave-guide vs. wave-guide width. The dashed line shows the WR-42 dimensions used in the first phase of the experiment. The material used in the attenuation calculation is aluminum which has a surface resistivity of 0.051 Ω at 25 GHz.

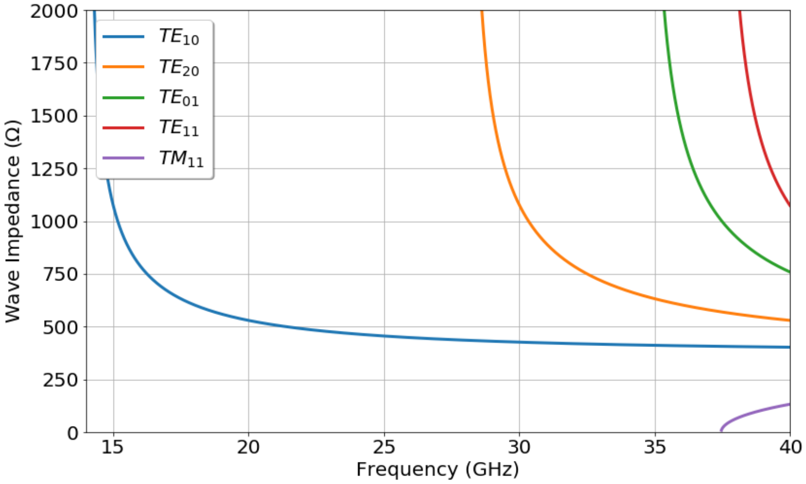

Figure 2.4: Wave impedance for the first five wave-guide modes of WR-42 as a function of operating frequency.

at 28.102 GHz. This ensures a single mode operation for the interested range of frequencies $(24.8 - 25.6\ GHz)$. The attenuation for this waveguide is also below 0.5 dB/m for the designed frequency range (see Fig. 2.5).

Fig. 2.6 shows the phase I gas cell manufactured out of aluminum. The cell is 76.2 mm long and it encloses 3.5 cm^3 of physical volume. Three trapping coils can be seen in the picture. The importance of these coils will be discussed in Sec. 2.2.3.

A circular wave-guide geometry is chosen for the second phase of the experiment. This upgrade is done based on two major consideration. First, since the radiated power of electron is proportional to $(\mathbf{J} \cdot \mathbf{E})^2 = (\mathbf{v} \cdot \mathbf{E})^2$ (Look at Eq. (3.40) and (3.44)), the fundamental mode of the circular waveguide can couple two times more efficiently to the cyclotron electron. Fig. 2.7 compares the mode coupling for the phase I rectangular and phase II circular gas cells [3]. The enhanced coupling in the circular design is due to the presence of two

---

[3] The exact definition and derivation of mode coupling will follow in the next chapter.

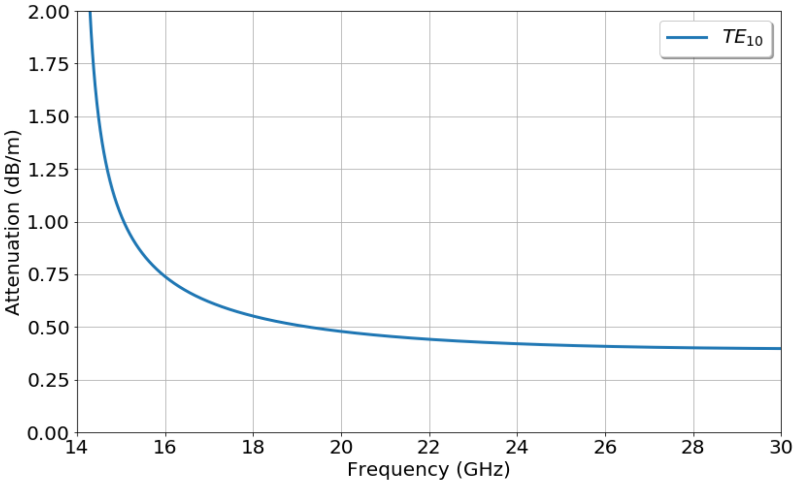

Figure 2.5: Wave attenuation for the fundamental mode of aluminum WR-42 as a function of operating frequency.

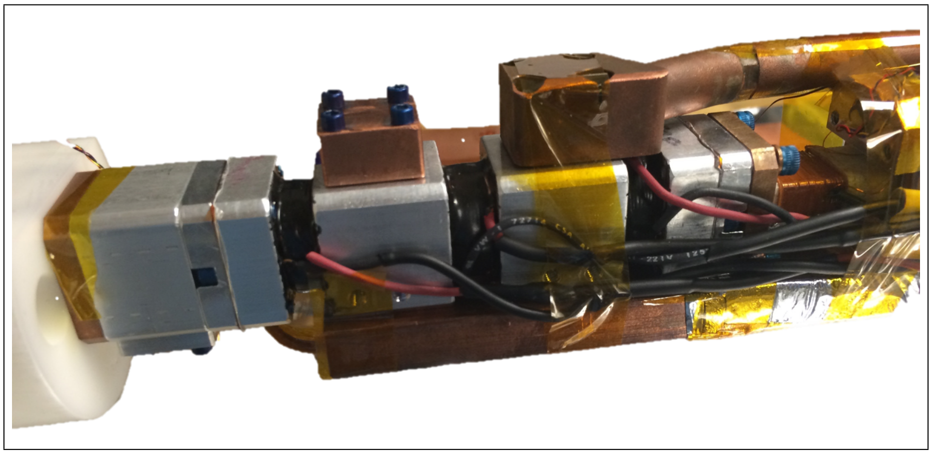

Figure 2.6: Phase I gas cell.

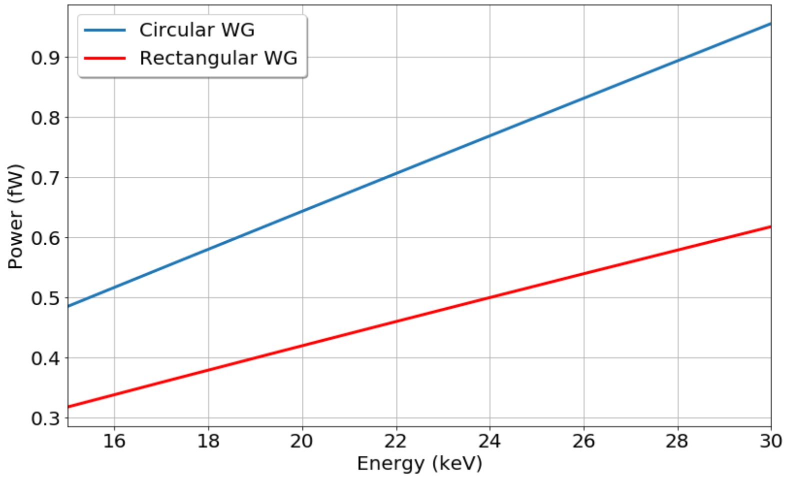

Figure 2.7: Electron's mode coupling comparison for rectangular and circular wave-guides used in the first and second phases of the experiment, as a function of electron's energy.

perpendicular electric fields in the fundamental mode of the circular waveguide while the electric field of rectangular wave-guide's fundamental mode has only one component along its smaller side. Second, the circular waveguide provides a larger cross section which results in an enlarged physical volume. This will increase the activity in the cell at a given pressure and temperature.

Fig. 2.8 illustrates the first five modes of the circular wave-guide used in the second phase of the experiment. Note that the TE_{11} and TM_{11} modes are doubly degenerate. It can be confirmed that the single mode operation is not any longer valid for the second phase of the experiment due to the proximity of TM_{01} to the fundamental mode of the circular wave-guide.

The change of the cut-off frequency of the wave-guide's fundamental mode from 14.1 GHz to 17.5 GHz in the circular design increases the wave impedance at the CRES signal's frequencies. Therefore the radiated power of the electron is enhanced in the new design. The increase in the attenuation of the wave is addressed by changing the wave-guide material from

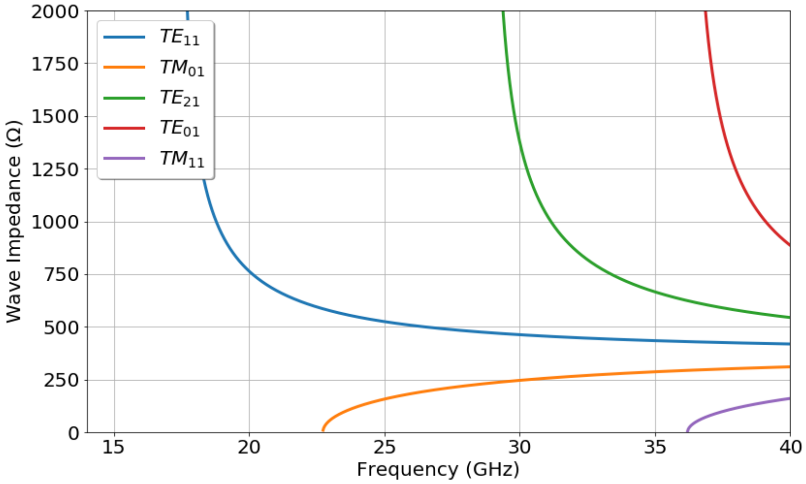

Figure 2.8: Wave impedance for the first five modes of a circular wave-guide with a 10.06 mm diameter, as a function of operating frequency.

Aluminium to Copper (see Fig. 2.9). Copper has a surface resistivity of 0.04 Ω which is 20% smaller than Aluminium. Fig. 2.10 illustrates that even with the higher cut-off frequency, the change of material and geometry keeps the attenuation lower than 0.25 dB/m, which is an improvement over the phase I design.

Fig. 2.11 shows the gas cell for the second phase of the experiment. It is 142.2 mm in length and encloses a physical volume of 45.6 cm^3. Although, the physical volume has increased by more than an order of magnitude, the activity scales with the effective gas volume which is a function of trapping geometries and signal to noise ratio.

2.2.2 Windows Design

To confine the radioactive gas inside the gas cell, the two ends of the cell must be closed. These caps should be RF transparent to avoid disturbing the CRES signal transmission to the receiver. The window transparency can be achieved by either making a thin window (smaller than $\lambda_{win}/10$) or tune the window's thickness to be a multiple of $\lambda_{win}/2$. The

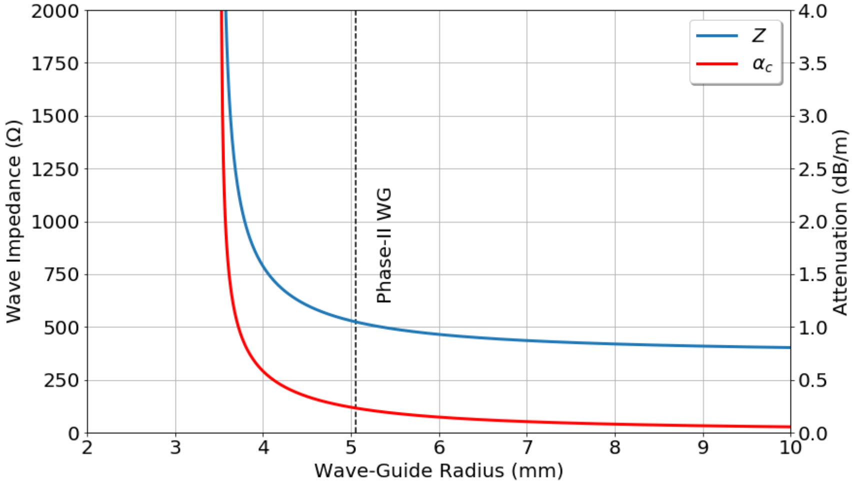

Figure 2.9: Wave impedance and attenuation at 25 GHz for the fundamental mode of a circular wave-guide vs. its radius. The dashed line shows the phase II wave-guide dimension. The material used in the attenuation calculation is copper which has a surface resistivity of 0.041 Ω at 25 GHz.

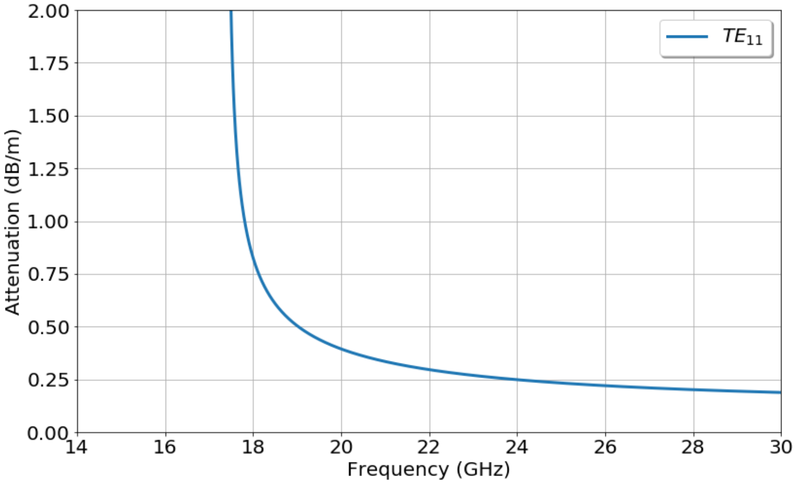

Figure 2.10: Wave attenuation for the fundamental mode of phase II wave-guide as a function of operating frequency.

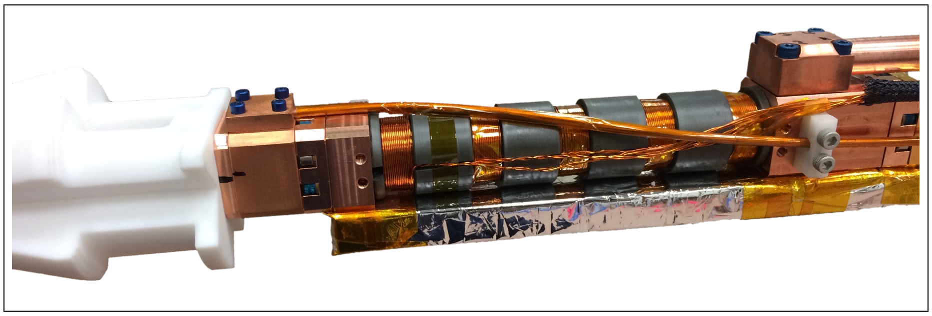

Figure 2.11: Phase II gas cell.

windows should also be mechanically stiff to stand 1 atm of pressure difference across their sides.

In the first phase of the experiment a 127 μm of polyimide window is clamped between two indium gaskets. This material can not be used in the second phase due to the diffusion of tritium into this thin film. CaF2 is picked as the material for manufacturing the windows based on the success of HFSS models and also proximity of its thermal expansion coefficients to the copper's [55]. However a thin layer of CaF2 cannot resist the pressure difference or the gaskets' force. Therefore a 2.4 mm thick window of CaF2 is chosen which corresponds to half a wavelength at the operational frequencies [4].

After installing the CaF2 windows, the RF transmission properties of the gas cell are measured with a network analyzer. The results shown in Fig. 2.12 assure a 1.2 GHz of 0.5 dB bandwidth.

2.2.3 Magnetic Bottle Design

Electrons with tens of kilo-electron volts energy travel tens of meters in a microsecond. The short observation time causes two main challenges. First, since the resolution of the

---

[4] CaF2 has a relative permittivity of 6.5 at temperatures lower than 100 K [30]

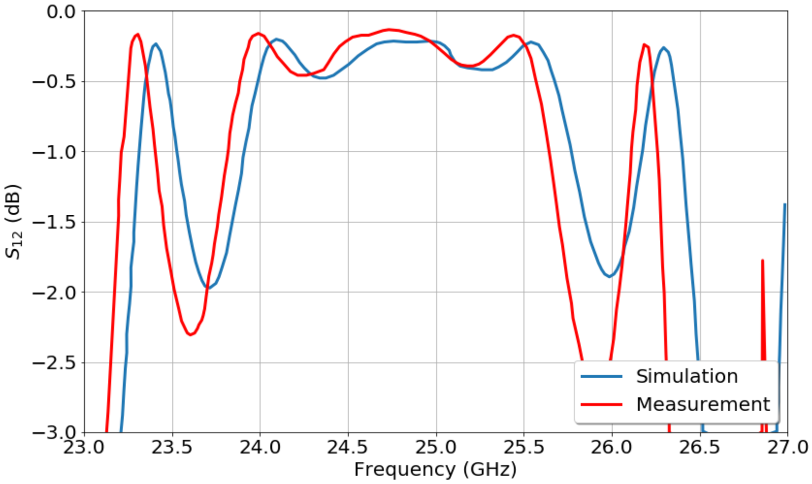

Figure 2.12: The transmission coefficient from simulation and measurement, for the full gas cell assembly with two CaF2 windows. The discrepancy might be the result of a slight difference in CaF windows width and/or dielectric constant.

frequency measurement is inversely proportional to the observation time,

$$\Delta f \propto \frac{1}{\Delta t}, \tag{2.1}$$

tracking the electron for a short period of time will limit the energy resolution of the experiment,

$$\Delta E = (E + mc^2)\frac{\Delta f_c}{f_c}. \tag{2.2}$$

Second, detecting a short duration signal is an impossible task for the event reconstruction algorithms. Therefore, the electron ought to be confined in the gas cell for a longer period of time. This suggests the use of some trapping technique in the gas cell. Since the known Penning trap method disturbs the electron's energy, it is not a viable option for a CRES experiment with the main goal of measuring electron's energy. Thus a pure magnetic trap is a must in Project 8.

A magnetic bottle trap is the simple trapping technique used in Project 8. To understand the working principle of this trap, one needs to consider an electron moving inside a varying magnetic field region. The electron's energy can be rewritten in terms of its velocity along the magnetic field and perpendicular to it,

$$E = \frac{1}{2} m_e v_0^2 \cos^2(\theta) + \frac{1}{2} m_e v_0^2 \sin^2(\theta), \tag{2.3}$$

where θ is called the pitch-angle defined as the angle between the magnetic field and the electron's velocity. The second term can be rewritten in terms of electron's magnetic moment,

$$E = \frac{1}{2} m_e v_0^2 \cos^2(\theta) + \mu B, \tag{2.4}$$

with the magnetic moment defined as,

$$\mu = \frac{m_e v_0^2 \sin^2(\theta)}{2B}. \tag{2.5}$$

In the adiabatic regime, where the change in the magnetic field is slow compared to the cyclotron frequency, the magnetic moment is a constant of motion. Therefore, as the electron traverses to regions with higher magnetic field, its pitch-angle increases. If the pitch-angle approaches 90 degrees, the electron will change its direction of motion. Hence, electrons with pitch-angle close to 90 degrees, can be trapped in a region of low magnetic field. The condition for trapping electrons can be calculated with the adiabaticity assumption,

$$\theta_{bot} > \sin^{-1} \sqrt{1 - \Delta B / B_{max}}, \tag{2.6}$$

where θ_{bot} is the value of electron's pitch-angle at the bottom of the trap. Since a greater range of pitch-angles can be trapped with a deeper trap, more events are expected in these traps [5].

The valley in the magnetic field required for trapping electrons, can be achieved by using simple coils. In the first phase of the experiment three trapping coils are wrapped around the gas cell (see Fig. 2.6). These coils can provide different trap depths in two different trapping

---

[5] A more systematic way of discussing electron's motion in a region of varying magnetic field is presented in the next chapter.

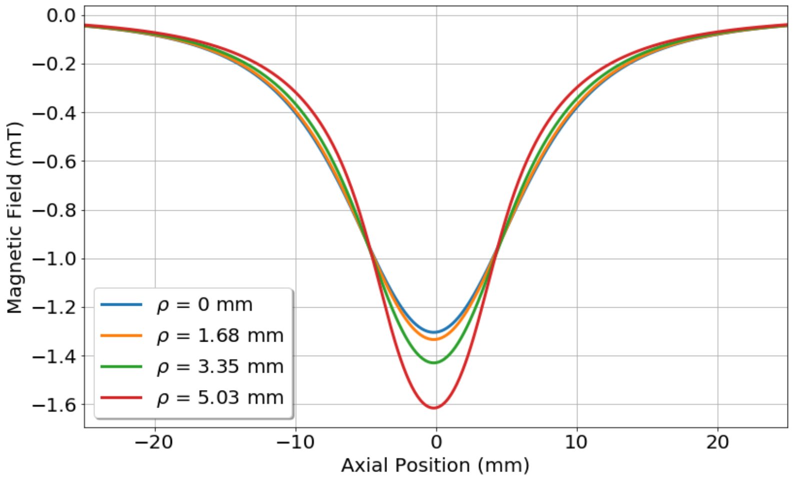

Figure 2.13: The field profiles of a single coil running at 0.3 Amp, along its axis at different radii. The coil is running at *harmonic* mode and the background field is set to zero.

geometries. First, utilizing a single trap with a polarity opposite to the background field makes a short magnetic bottle trap. This trapping geometry is named “Harmonic Trap” due to its resemblance to a harmonic potential. Running two coils with polarities along the background field makes a longer trap which is named “Bathtub Trap”.

In the second phase of the experiment five trapping coils are wound around a Macor support structure placed on the cell. AWG 26 wire gauge is used to wind the coils. There are four layers of wires in every single coil. The first three layers are formed with 16 turns while the last layer has 14 turns. Fig. 2.13 shows the magnetic profile of a coil with a 0.3 Amp current at different radii inside the cell.

The choice of material for the support structure is made due to Macor’s high heat conductivity of 1 $\frac{W}{m.K}$ at 100 K [35]. The coils are 7.62 mm long and the outer radius of the support structure is 7.44 mm. Thus the area of the coil in contact with the support structure is 356.2 mm^2. Therefore, the 1 mm thick Macor support structure can conduct 0.36 W of heat in a situation with 1 K temperature difference. Since the coils’ resistances are 0.4 Ω, even a 1 K temperature difference provides enough cooling for the coils at 1 *Amp*. Varnish is added between the coil layers to assist the heat transfer out of the coil structure.

To insure the effectiveness of the heat conductance a test was performed in which the cell was cooled down with liquid nitrogen. The coils were run with currents while observing their temperature. We concluded that running the coils with currents as high as 1 Amp does not increase the cell temperature by more than 5 K.

2.3 Receiver

The radiation power from a single cyclotron electron in a 1 T field is around 1 fW. This low intensity radiation necessitates an efficient receiver chain with low noise temperature and a high value of gain.

Project 8 receiver is composed of three different sections. The first section is designed to propagate the microwave power from the electron in the gas cell to the cryogenic amplifiers residing outside of the magnetic field region. The signal is then amplified using two stages of low noise amplifiers. In the next step the signal is down-converted from K band to L band of the microwave spectrum. Further amplification and conversion follows from this stage to match the signal to the dynamic range of the data acquisition systems.

In the following sections, we explain the receiver chain for the first two phases of the experiment in more details.

2.3.1 Phase I Receiver

Since the phase I gas cell is manufactured from a WR-42 waveguide, the natural choice for propagating the RF power to the amplifier stage is the same waveguide model. A 1.2 m WR-42 copper waveguide is what we use for the purpose of transferring the signal out of the field region.

In the next step two LNF-LNC22-40WA amplifiers are used to amplify the signal (Fig. 2.14). The amplifiers are cooled down to $\sim$ 40 K with a single-stage Gifford-McMahon cooler. Each one of the amplifiers add a $\sim$ 28 dB gain to the signal [22].

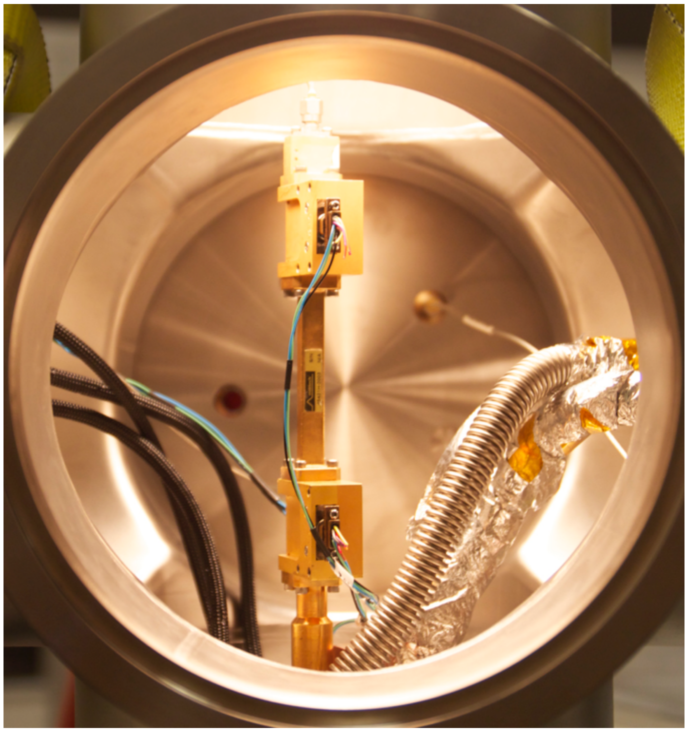

Figure 2.14: Two stages of low noise amplifiers connected with a WR-28 waveguide.

The input port of the amplifiers is a WR-28 type wave-guide. Therefore a waveguide taper is added prior to the first amplifier in order to convert WR-42 to WR-28 waveguide. Another WR-28 waveguide with gold coating connects the two amplifiers.

In order to increase the signal to noise ratio, a copper plate is added to the other side of the gas cell. This plate act as an RF reflector which increases the signal power by 3 dB.

The combination of the gas cell and the receiver chain up to, and including, the amplifier stage is called the CRES insert. The insert is connected to a Cryomech AL60 cryogenic refrigerator. The whole insert is attached to a copper bus bar which in addition to providing the mechanical support, increases the heat conductance between the insert and the cold head. A heater is connected next to the gas cell to increase its temperature for avoiding krypton freeze at $\sim 120\ K$.

The signal has gained enough power to enter the room temperature after the two low noise amplifiers . An adaptor is used to send the signal from the WR-28 to a coaxial cable. Afterward, a 24.2 GHz Exodus Dynamics EDPLO-3000-24.20 phased lock oscillator is used to down-convert the signal from the K band to L band of the microwave spectrum. Next, the signal is sent to a Tektronix real-time spectrum analyzer, RSA6100B to be digitized and recorded.

2.3.2 Phase II Receiver

In the second phase of the experiment the gas cell is upgraded to a circular waveguide as was discussed in Sec. 2.2.1. In order to use the same piece of WR-42 waveguide for propagating the microwave power out of the magnetic field region, a quarter-wave-plate is attached to the gas cell. The plate converts the circular polarization of the cyclotron radiation signal to a linearly polarized microwave. A transition piece then transfers the power from the circular waveguide to the WR-42.

By investigating the noise sources in the first phase, we found that a significant source of the frequential dependency in the noise was the back scattering of amplifiers' noise from the RF reflector. To terminate this noise a cryogenic circulator is added before the waveguide taper. The second port of the circulator is attached to a terminator. Hence, any RF signal radiating from the amplifiers will be terminated without disturbing the power transition from the gas cell into the amplifier stage.

As it was mentioned in the last section, the gas cell's temperature is required to be kept above krypton freezing point. Therefore a heater is connected near the gas cell. However the heat from this heater increases the amplifier's temperature and therefore increases the thermal noise. To stop this heat to reach the amplifiers, a gold coated stainless steel WR-42 waveguide is added before the circulator. The poor thermal conductivity of stainless steel halts the heat from the heater to warm up the amplifiers and the circulator. The gold coat is added to maintain low RF attenuation.

Another significant upgrade in the phase II insert is the replacement of the RF reflector with a terminator. This change is done, in spite of the obvious loss in the signal to noise ratio, to avoid the complexity associated with the patterns caused by the interference of the reflected and the propagated waves. In the next chapter we will discuss this phenomenon in more details.

A cone shaped design is chosen for the terminator to provide a gradual change in the impedance and thus to decrease the reflection (Fig. 2.15). A mixture of stycast 1266 epoxy with superfine natural graphite spherical powder is used to build the terminator. These materials are chosen due to their non-magnetic and dissipative features.

Three terminator with 0%, 10%, and 20% graphite concentration by weight are casted. Next, the RF reflection of these three terminator is measured in the frequency range of interest. Plot 2.16 shows the reflection coefficients of the three manufactured terminators and compares them with an ANNE-50L+12 GHz SMA terminator [6]. The terminator with 20% graphite concentration is chosen because of its least frequency dependent attenuation.

After the amplifier stage, the signal enters the room temperature where it is down-converted by 24.5 GHz. A directional coupler then sends the signal into the two separate

---

[6] The terminator is designed for 12 GHz. That is the reason for the imperfect termination at 24-26.5 GHz frequency range.

Figure 2.15: The cone shaped terminator manufactured for the second phase of the experiment. A mixture of epoxy and graphite is used to cast the terminator.

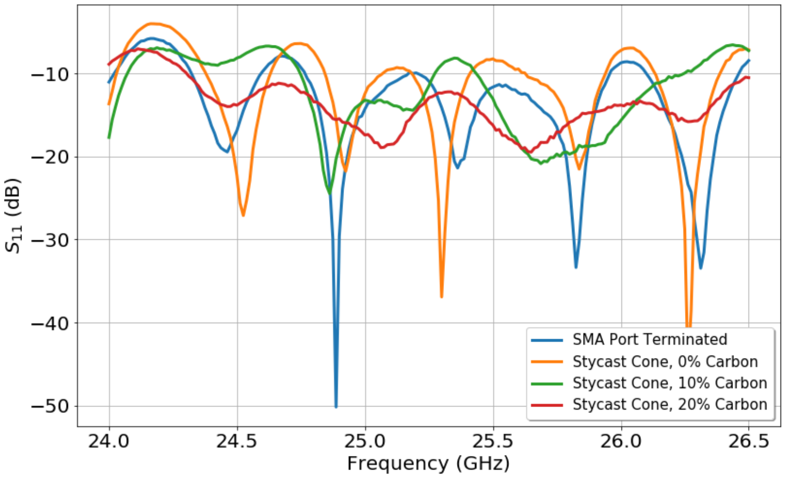

Figure 2.16: Comparison of reflection coefficient for three manufactured terminators with Stycast epoxy and different carbon concentrations, and an SMA terminator.

data acquisition systems. The uncoupled port is connected to an 8-bit ROACH2 digitizer which is the main *Data Acquisition* system used in the second phase of the experiment. The coupled port is connected to the RSA which is used in the first phase of the experiment.

In order to measure the gain and the noise temperature of this complicated receiver chain, the heater is used to change the terminator's temperature. Then the power spectral density of the RF background is recorded. The frequency dependent behavior is used to investigate impedance mismatches. This study leads to the addition of the circulator to the second phase's design.

The temperature dependent changes in the recorded spectrum is used to estimate the gain and the noise temperature of the receiver. This is done by developing a thermal model for the insert and utilizing a Y-factor method. In this technique the output noise power of the receiver is measured at different terminator's temperatures. Fitting these measurements with the functions from the thermal model provides information on the noise temperature and the receiver gain at different frequency ranges. Fig. 2.17 illustrates the system gain and Fig. 2.18 shows its noise temperature obtained from Y-factor method [7].

2.4 Field Shifting Solenoid

In the last section we showed that the receiver system's noise and gain vary with frequency. The signal to noise ratio variations in the frequency range of interest for tritium beta-decay measurement, leads to a systematic effect in the count rates at different energy bins.

One strategy to investigate this systematic effect is to use an electron source with a non-varying count rate in the energy range under study. However, there were no suitable electron sources found. Another strategy is to use a mono-energetic electron source at different magnetic field backgrounds. With an altering magnetic field, the cyclotron frequency of the electron can be changed in the frequency range of interest.

We use the K shell conversion electrons from ^{83m}Kr with 17.83 keV energy, to map the

---

[7] The Y-factor measurement and analysis is done by Raphael Cervantes (raphaelc@uw.edu).

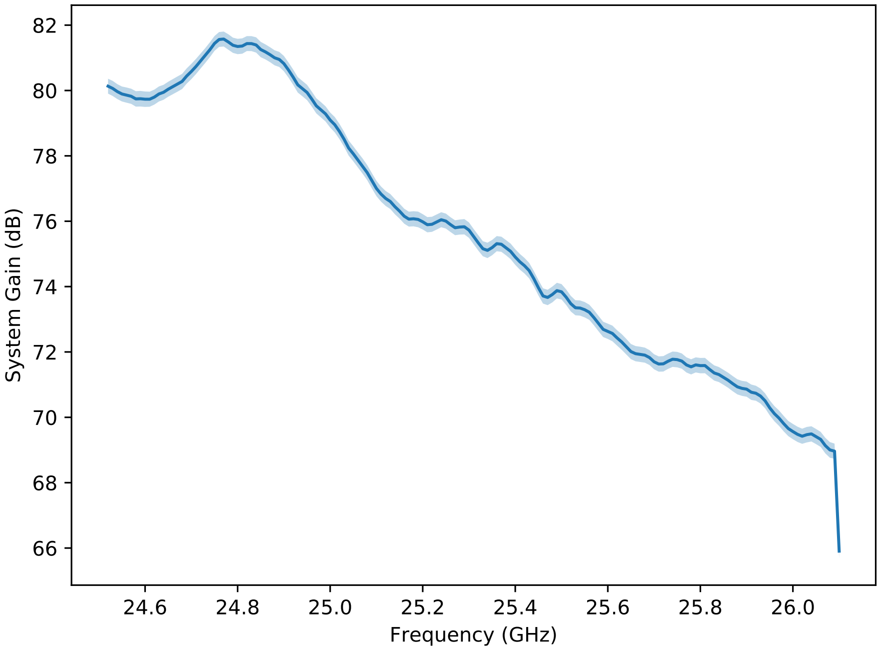

Figure 2.17 asurements.

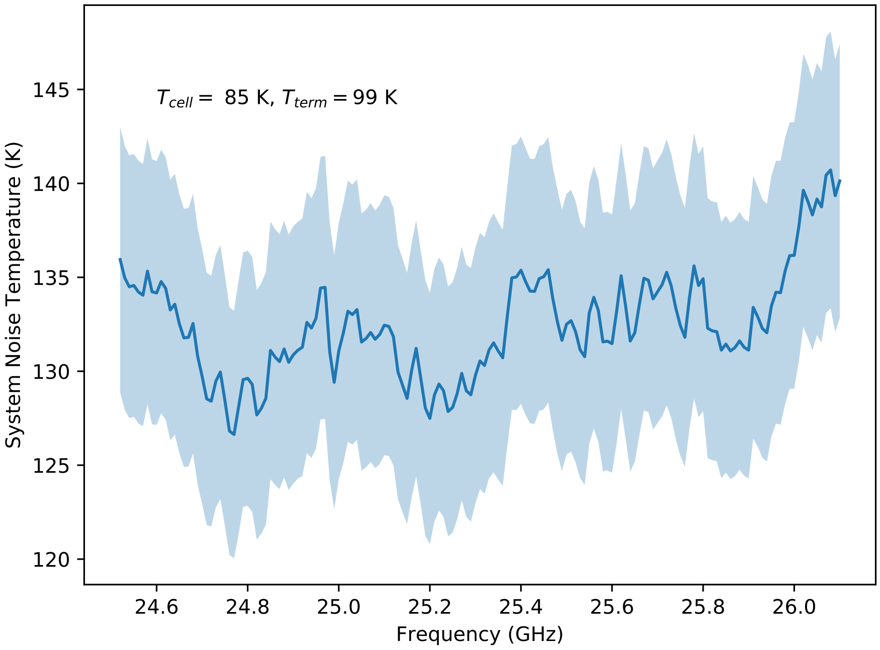

Figure 2.18: The receiver system noise temperature obtained from the Y-factor method measurements for the normal operating temperatures.

Figure 2.19: The field shifting solenoid designed to change the background field, and hence the cyclotron frequency of mono-energetic electrons from ^{83m}Kr. This coil is used in the study of frequency-dependent systematic effects introduced by the complicated receiver chain. The pipes are welded to the solenoid to cool it down during high current runs.

system response at different frequencies by changing the background field. Fig. 2.19 shows the solenoid designed to shift the background magnetic field in the gas cell. This solenoid has a 34.3 cm long coil supported from the bottom of the NMR magnet. Five rounds of copper tubing are welded to the bottom of the solenoid in order to run cooling water and prevent overheating. The coil is manufactured from two layers of AWG 24 wire potted with varnish.

Fig. 2.20 shows a simulation of the magnetic field generated by the field shifting solenoid running at 1 Amp [8]. The 1 Amp current generates a 4.9 mT field which is enough to move the 17.83 keV line by $\sim$ 130 MHz in the frequency domain. Furthermore, the coil is designed long enough so that the field variation along the whole gas cell length is less than 0.04 mT.

2.5 Gas System

In the last two sections the gas cell and the receiver chain for detecting the CRES signal were discussed. In this section we explain the gas system which has the burden of feeding the gas cell with the radioactive gas.

---

[8] The exact number of rounds of the coil is unknown. The estimate is based on the solenoid length and the wire's outer diameter.

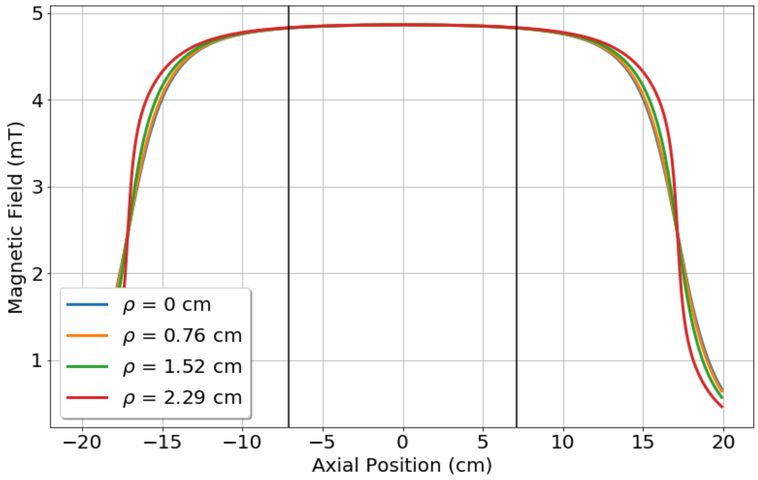

Figure 2.20: The magnetic field generated by the field shifting solenoid running at 1 *Amp* at different radii. Vertical lines display the position of the gas cell inside the field.

The first phase of Project 8 utilized mono-energetic conversion electrons emitted from ^{83m}Kr to demonstrate the viability of CRES technique. Phase I gas system is designed to deliver krypton gas to the gas cell. A low background gas pressure is a key required feature of this system. Electrons scatter off the residual gas in the presence of a non-negligible gas pressure. A higher probability of scattering decreases the observation time for electrons. This affects the efficiency of track reconstruction and also diminishes energy resolution as it was discussed in Section 2.2.3.

The second phase of Project 8 utilizes tritium gas as a beta decay source. Delivering tritium to the gas cell and regulating its pressure is one of the milestones in the second phase of the project. The phase I gas system is designed to deliver ^{83m}Kr and is not capable of handling tritium. Therefore, a brand new system is built. Since mono-energetic conversion electrons from ^{83m}Kr are crucial calibration tools, the new design is made in a way to address difficulties in handling tritium and krypton simultaneously.

In addition to the low background pressure requirement, the system should be facilitated with the capacity to regulate the tritium pressures in the gas cell. A higher tritium pressure results in a higher event rate in the spectrum. Nevertheless, a high tritium pressure decreases the mean free time of the electrons which reduces the number of detectable electrons due to limited radiated energy. Adjusting the tritium pressure assists us to find the optimum pressure for the greatest number of detectable events in the tritium beta-decay spectrum.

In this section we first briefly describe the phase I gas system. Then we discuss the combined Kr/T_2 gas system built for the second phase of the project.

2.5.1 Phase I Gas System

The phase I gas system utilizes a Pfeiffer HiCube 80 Eco turbo-molecular pump to reach UHV pressures. However, this pump cannot be used during data taking. To pump on the background pressure without pumping the radioactive gas, two SAES GP-50 non-evaporable getter (NEG) are used. Pressures lower than 5×10^{-7} Pa are reached with utilizing these two chemical getters.

The meta-stable krypton isotope used in Project 8 has a short half life of 1.8 hours. Hence, a continuous source of ^{83m}Kr is needed in the system. ^{83}Rb is selected as an active source of ^{83m}Kr. This choice is based on the high branching ratio of ^{83}Rb to ^{83m}Kr. ^{83}Rb also has a longer half lifetime of 86 days. A chloride salt of Rb is the chemical substance used in the source. RbCl is adsorbed onto Zeolite beads with 2 mm diameters. The beads are transferred in to a stainless steel ampoule. The decayed noble atoms of krypton do not bind to Zeolite matrix. Therefore, they will diffuse out of the Zeolite in to the system. A more detailed review of the phase I gas system is presented in [33].

2.5.2 Phase II Combined Kr/T_2 Gas System

Fig. 2.21 shows the valve schematics for the combined Kr/T_2 gas system. The system can be understood by regarding the three distinct sections. The combined gas manifold attaches the radioactive sources to the system. A similar ^{83}Rb source is used to feed the cell with ^{83m}Kr gas.

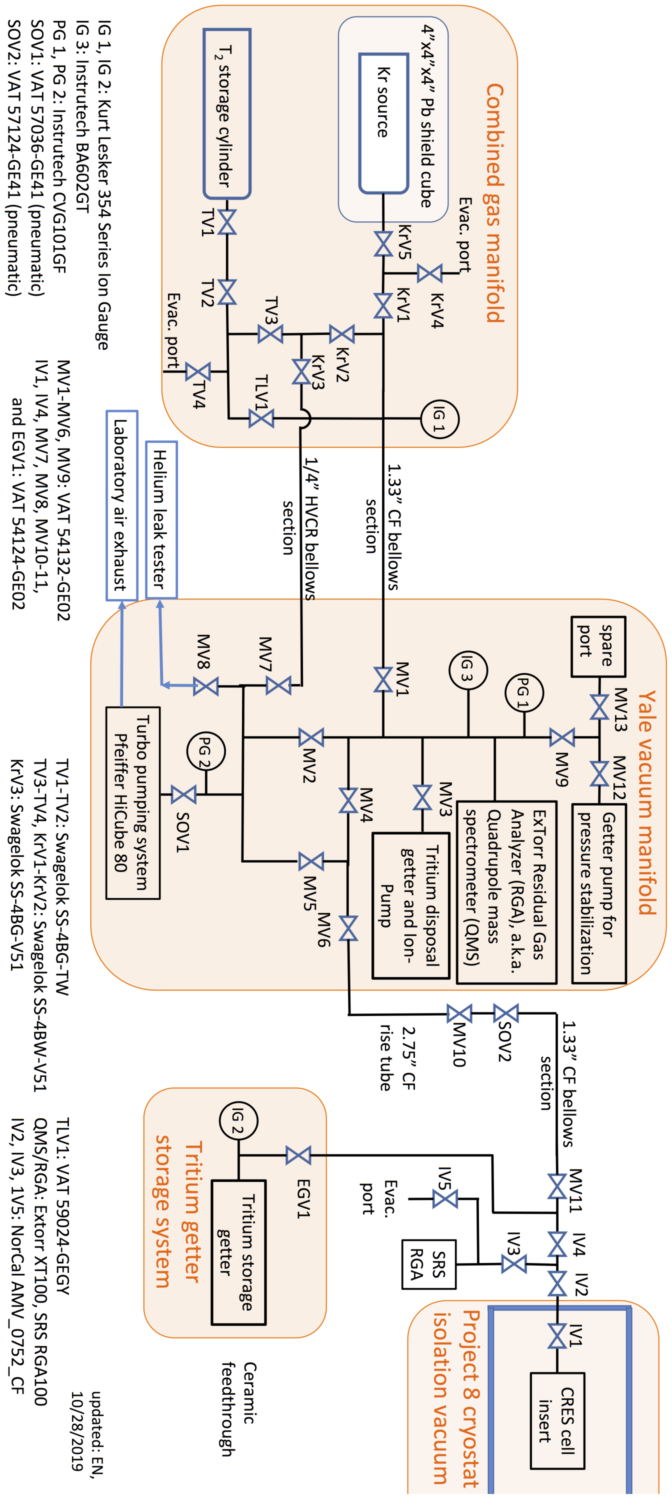

Figure 2.21: Valve Schematics for the combined Kr/T_2 gas system. The three main sections are represented. The red lines show the locations for bi-weekly swipe tests.

Figure 2.22: The cylinder built for storing $2Ci$ of tritium. The VCR valves are welded to the cylinder for safety reasons. They also facilitate a controlled release of tritium into the gas system.

A cylinder, shown in Fig. 2.22, is designed to store 2 Ci of tritium gas. Two VCR full metal valves are welded to the cylinder with a small volume between them. This specific configuration is designed to facilitate a controlled release of the gas in to the system. In the first step, the gas is expanded in to the volume in between the two valves by opening the first one. The second valve can then be opened after the closure of the first one to release a controlled amount of the tritium gas in to the system.

The second part of the system is the Yale vacuum manifold which contains the measurement devices and pumps. Two Instrutech CVG101 convection gauges are measuring pressures in the range of 1.3×10^{-4} $mbar$ to 1.33 $mbar$. An Instrutech BA602 ion-gauge is added to measure low pressures down to 5.3×10^{-10} $mbar$. An EXtorr XT100 residual gas analyzer is also attached to the system for partial pressure measurements.

A Pfeiffer HiCube 80 is the main pump used to reach pressures below 1.3×10^{-9} $mbar$ after baking the system. In addition to the mechanical *Turbo Molecular Pump*, two non-evaporable getters are added to this manifold. The disposal getter is a NEXTorr D 100-5 NEG, designed initially to pump the tritium out of the system after the conclusion of the tritium runs. Since pumping on a tritiated system with the Turbo Molecular Pump rises safety concerns, the disposal getter is additionally is used to reduce the background pressure in the presence of residual tritium gas in the system. This pump is equipped with a diode ion-pump which is a useful instrument for pumping the noble gases in cases where the mechanical pump cannot be used.

Another non-evaporable getter pump is designed to produce a relatively high background pressure ($1 - 3 \times 10^{-6}$ $mbar$) of hydrogen gas. The purpose of increasing the background pressure is to simulate the tritium run conditions for calibration runs. The main objective is to find the maximum pressure at which the track and event reconstruction algorithms can efficiently find electrons. One of the two SAES GP-50 NEGs from the phase I gas system is connected to the Yale manifold to produce this hydrogen background. The pressure is controlled through a P.I.D. loop which controls the current injected into the chemical pump's activation filament.

The last section of the gas system is the tritium getter storage system which we will explain separately in the following section.

Tritium getter storage system

Regulating the tritium pressure in the gas cell is one of the main objectives of the new gas system design. While a higher pressure of tritium results in a higher number of beta-decay electrons, it decreases the observation time which reduces the probability of detection. Thus, a SAES st-172 zirconium based chemical getter (referred to as disposal getter from this point) is placed adjacent to the gas cell. This type of non-evaporable getter controls the pressure

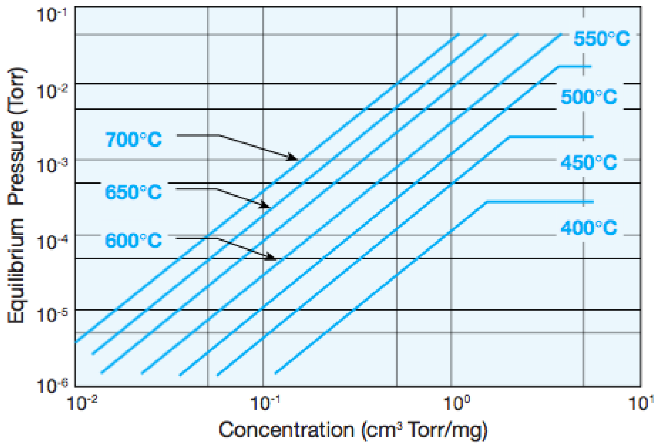

Figure 2.23: The H2 equilibrium pressures of St 172 as a function of the hydrogen concentration in the gettering material at different working temperatures.

of hydrogen via

$$H_2 + 2ZrAl \underset{desorption}{\overset{absorption}{\rightleftharpoons}} 2(ZrAl - H) \tag{2.7}$$

diffusion reaction. Heating the getter increases the desorption rate in comparison with the absorption rate and releases hydrogen into the gas cell. For hydrogen isotopes in a metallic getter, the equilibrium pressure, P, can be derived from Sieverts' law in which

$$\ln P = A + 2\ln q - \frac{B}{T}. \tag{2.8}$$

Here q is the hydrogen concentration in the metallic alloy, T is the temperature, and A and B are specific constants which should be measured for each getter separately. Fig. 2.23 illustrates how the equilibrium pressure varies with temperature at different hydrogen concentrations in these getters [1].

Nitrogen, oxygen, carbon-monooxide, and carbon-dioxide can be pumped with this zirconium based getter through surface sorption at room temperature. Increasing the getter's temperature causes a diffusion of these gases into the bulk. These gases form stable chemical compounds that cannot be decomposed even at high temperatures. Hence the process of pumping these gases is an irreversible interaction.

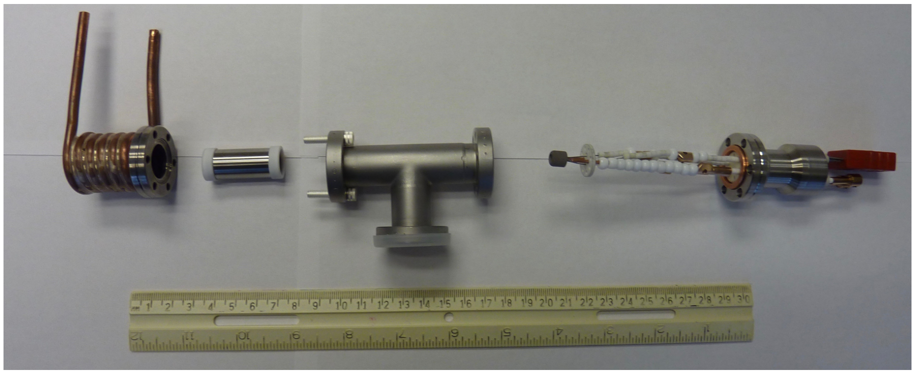

Figure 2.24: The tritium getter storage system before the final assembly. Two sets of wires connect the getter's heater and a C-type thermocouple to a feed-through connector. A copper tube is welded around the mini-conflat half-nipple to cool down the system with water.

The getter additionally absorbs water vapor by cracking it to hydrogen and oxygen molecules. The getter also absorbs hydrocarbons through similar cracking of these molecules to hydrogen and carbon. However hydrocarbon molecules can only be cracked at temperatures above $300°C$ [1].

The storage getter is placed in a mini-conflat half nipple. A copper tube is welded around this part that runs water to cool down the half nipple while the getter is running at high temperatures. The delicate filament connectors are clamped into two small copper tubes which are connected to a leak tight feed-through. A C-type thermocouple is placed inside the donut shaped storage getter for measuring its temperature. This sensor is also connected to the feed-through using Tungsten and Rhenium connectors[9]. Ceramic beads are used to cover the connectors to avoid any undesirable contact. Fig. 2.24 shows this setup before the final assembly.

A Kurt.J Lesker 354 series ion-gauge is added to the getter compartment to measure the released pressure of tritium. This ion-gauge provides the feedback measurement to regulate the pressure using a PID loop.

---

[9] Using different conductors would make additional thermocouples at the connection spots.

D_2 Tests

A series of tests are run to investigate the performance of the storage getter. The tritium runs were avoided at this point due to safety concerns related to handling a tritiated getter material.

A bottle of deuterium is connected to TV4 before installing the tritium cylinder (Fig. 2.21). A small pressure of deuterium gas is expanded into the region between TLV1, TV3, and TV2. Then the leak valve, TLV1, was gradually opened to released deuterium while the storage getter was heated to the designed operational temperature of $400°C$. This process continued until an equilibrium pressure of 2.2×10^{-6} *torr* is achieved.

In the next step the storage getter is cooled down to room temperature. Afterward, the filament's current is incremented with 0.5 *amps* steps. The partial pressures of hydrogen isotopes measured with the residual gas analyzer are plotted in Fig. 2.25. An obvious increase in the partial pressures can be observed. The main gas component is D_2 with a smaller partial pressure of HD in the system. There is also a small concentration of H_2 inside the storage getter.

The KJL ion-gauge measurement can be used to find the equilibrium pressure for each step with a given current[10]. Since the thermocouple temperature measurement depends on the thermal coupling between the thermocouple and the surface of the getter, it cannot be trusted as an accurate measurement. The filament resistance is a more precise measure of the getter temperature. The filament's resistance can be estimated using its voltage and current at each step. Regarding the temperature coefficient for Molybdenum resistance ($\alpha = 0.00482$)[11], a more accurate measurement for getter's temperature is attainable.

Fig. 2.26 shows the equilibrium pressure in the system as a function of getter's temperature. The data is fitted with the Sievert's law, Eq.(2.8), to get the empirical coefficients. According to the SAES st 172 getter's manual the value for the temperature coefficient (b

---

[10] The residual gas analyzer data cannot be used due to the unknown normalization scheme.

[11] https://pubs.acs.org/doi/abs/10.1021/je60025a028

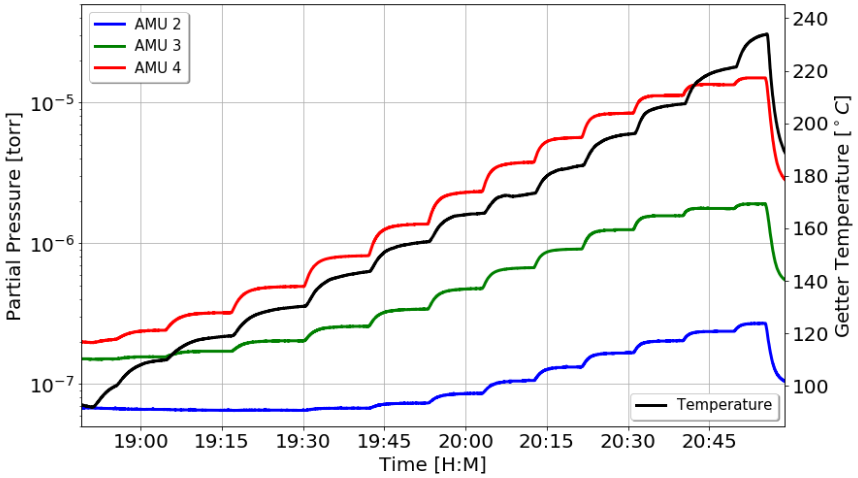

Figure 2.25: The measured partial pressures of hydrogen isotopes at different getter temperatures. The temperature measurement is from the c-type thermocouple touching the interior surface of the getter.

in Eq.(2.8)) is 5730 K which is in agreement with our measured value of 5712 ± 43 K. The concentration of deuterium in the getter can also be estimated using the fit. Comparing Eq.(2.8) with the value of $a = 4.45$ from the manual to Fig. 2.26 concludes the concentration of deuterium to be 2.3 ± 0.1 $LTorr/g$. The HI/7.5-7 model getter's mass that we are using is 550 mg. Therefore the total concentration of deuterium in the getter is 4.2 ± 0.2 $LTorr$.

After reaching equilibrium at the highest current, the getter is cooled down to the normal operating temperature. We run the getter at this temperature to assess the partial pressures' stability for several hours. Fig. 2.27 shows the partial pressure developments over a three days time period. The temperature is stable within 1% and the deuterium pressure varies at the ∼ 2% level. Note that this stable condition is reached without the support of any control system.

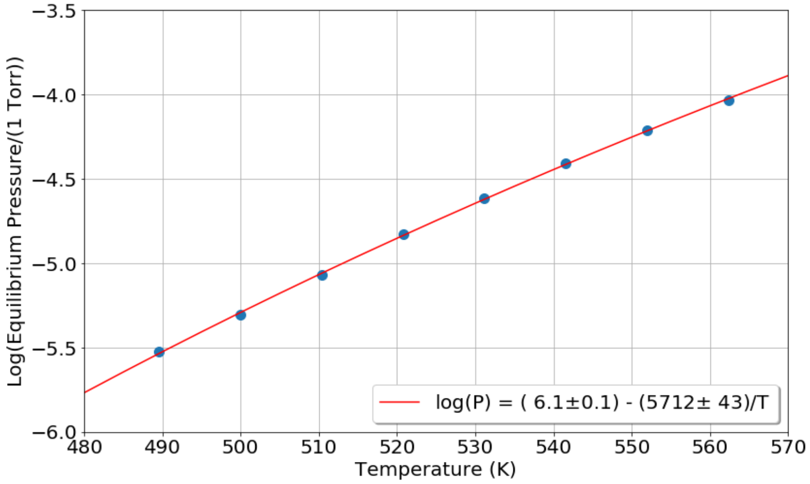

Figure 2.26: The equilibrium pressure vs. temperature for 8 different values of current feeding the storage getter's filament. The data is fitted with the Sievert's law (Eq. (2.8).)

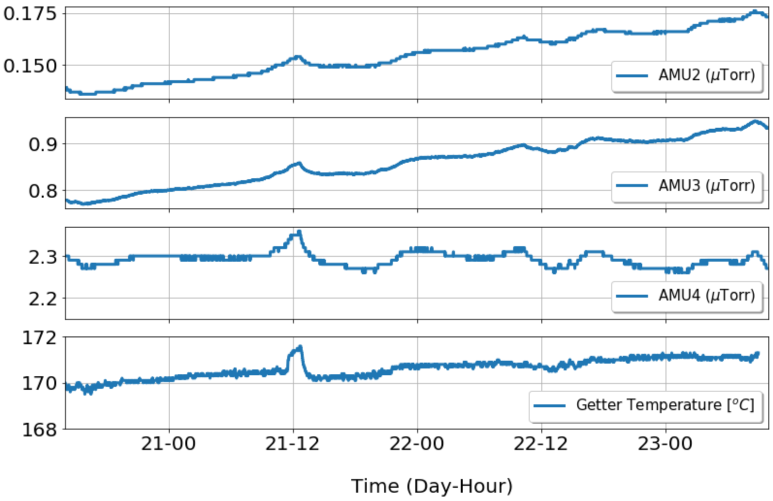

Figure 2.27: The partial pressure stability of hydrogen isotopes over a time period of three days. A constant current is running through the getter filament.

T_2 Runs

After the conclusion of deuterium test, the tritium cylinder is connected to the system. Tritium is released by opening TV1 and expanding the gas to the small volume in between the two valves, closing TV1, and then opening TV2. Fig. 2.28 shows the evolution of the partial pressures of the hydrogen isotopes. Note that the plot is showing the partial pressures at the end of the filling process where the pressures are low enough to run the residual gas analyzer.

As tritium is released into the system, the storage getter, which is at room temperature, pumps on the T_2, TH, and H_2 molecules. However the gas with atomic mass 3 is not pumped by the getter. The only gas with atomic mass 3 which cannot be pumped by a NEG is ^3He.

^3He is the product of tritium beta-decay and its presence in the tritium bottle is expected. We used our ion-pump at the end of each cycle to pump the ^3He out of the system without wasting any tritium.

After filling the getter with tritium we close MV11 to isolate the insert and the tritium getter storage system. The pressure then is increased to 2.2×10^{-6} $torr$ and tritium run starts.

One challenge in maintaining an acceptable tritium activity in the gas cell is the rise of background pressure. This rise eventually surpasses the pressure set point and turns off the voltage in the storage getter's filament and stops the release of tritium into the gas cell. ^3He is the major gas contributing to this background pressure. There are two sources of ^3He which gradually increase the background pressure. First, the tritium deposited on the stainless-steel walls of the getter compartment during the tritium fill releases ^3He into the system. Second, the ^3He gas from the decay of the tritium molecules inside the getter, leaks out of the storage getter and contribute to the background pressure.

To address the first source of ^3He, we bake the getter compartment and the connections to the gas cell. Fig. 2.29 shows the background pressure built-up as we close MV11, before and after the bake. It can be seen that the rate of the increase in the background pressure

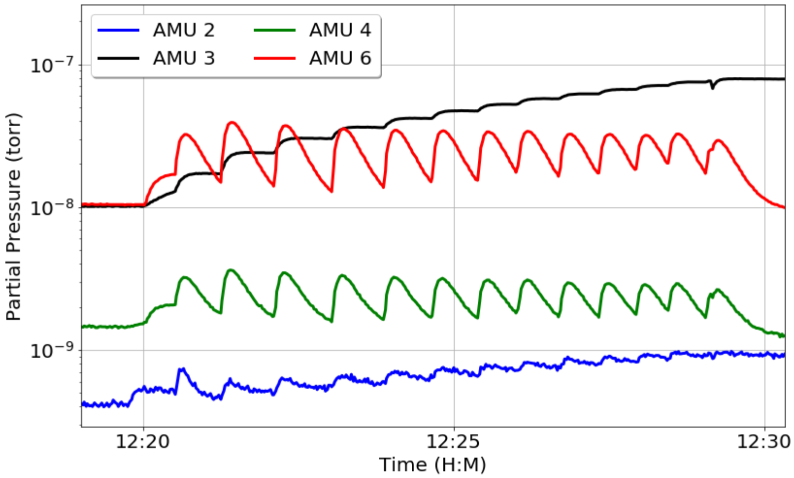

Figure 2.28: The partial pressures of hydrogen isotopes and ^3He in the gas system while the getter is being loaded with tritium from the source cylinder. Hydrogen isotopes are being pumped by the getter while the ^3He pressure is increasing after each filling cycle.

drastically decreases. There is also a factor of 2 improvement in the equilibrium background pressure.

To pump the ^3He out of the storage getter we initially reactivate the getter to release a large pressure of ^3He into the getter compartment. We then cool down the getter to reabsorb the tritium. Because the getter cannot reabsorb the ^3He, we use the ion-pump to pump the ^3He out of the system.

This technique is shown to be ineffective after we have stored the tritium inside the getter for months. Therefore, a continuous pump on the gas cell with the ion-pump is suggested. To reduce the amount of tritium pumped with the disposal getter and the ion-pump, a non-conventional path from the cell to the ion-pump is chosen. The ion-pump section is isolated from the cell and then they are connected via the leak valve (TLV1 in 2.21) in the combined gas manifold [12]. The leak valve can be controlled to optimize for the amount of helium and

---

[12] The exact valve configuration:

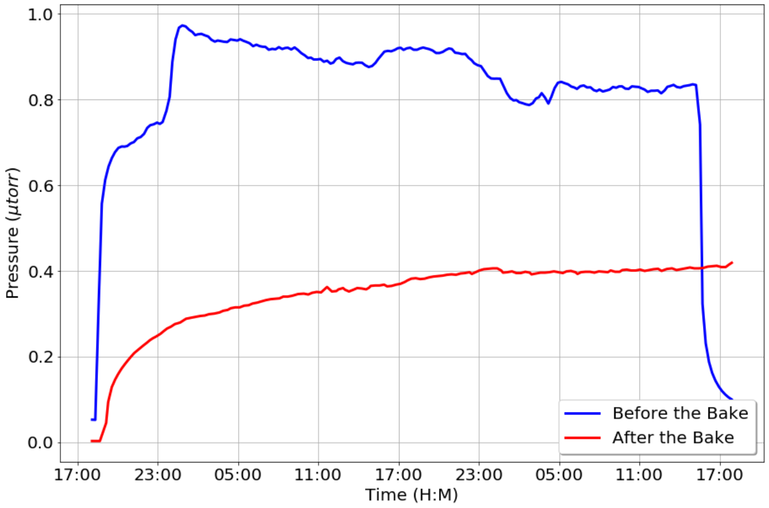

Figure 2.29: The background pressure evolution in the tritium getter storage system before and after baking the system.

tritium pumping.

The main concern in this new gas system configuration is a high pumping rate of tritium. This has the potential to pump all the loaded tritium out of the disposal getter. To measure the tritium pump rate, the valve to the ion pump is closed (MV3 in Fig. 2.21) and the ExTorr residual gas analyzer is used to measure the pressure rise in the tritium gas. The highest rate of increase is caused by AMU 4 (TH) which is $2.5 \times 10^{-9} mBar/min$. Using an upper estimate of 10 L for the gas system volume, the amount of tritium pumped with the ion-pump is estimated to be bellow 34 mCi/yr. The initial tritium activity loaded into the storage getter is 2 Ci. Therefore this rate of tritium pumping is not a concern.

An SRS RGA100 residual gas analyzer is attached next to the getter compartment 2.21.

Open valves: IV3, IV4, MV11, SOV2, MV10, MV6, MV5, MV7, KrV3, TV3, TLV1, MV1, MV3, MV12, KrV5

Closed valves: IV2, IV5, MV4, MV2, SOV1, MV8, TV4, TV2, TV1, KrV2, KrV1, KrV4, MV9, MV13

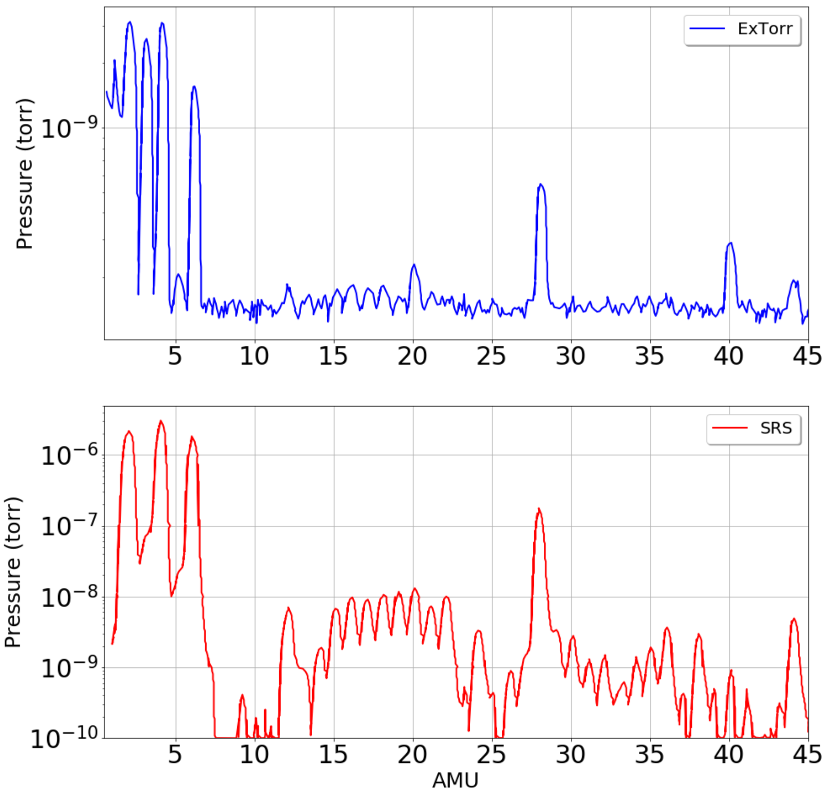

Figure 2.30: The gas composition measured by ExTorr and SRS (look at Fig. 2.21) residual gas analyzers during the tritium data taking. The SRS spectrum illustrates the presence of ^3He, HT, H_2 and T_2 in the gas cell with a small partial pressure of CO.

This residual gas analyzer provides more accurate measurement of the gas composition inside the gas cell due to its proximity to it.

This new configuration is used in the main tritium data taking campaign. The gas composition remains stable over more than two months of tritium data taking. Fig. 2.30 compares the gas composition measured by the two residual gas analyzers during the normal tritium data taking.

Chapter 3

PHENOMENOLOGY OF THE CYCLOTRON ELECTRON RADIATED POWER

The cyclotron frequency of an electron in a constant magnetic field follows the simple relation introduced in Eq. 1.12. However, in the realistic case there are a number of effects that break down this simplistic model.

First, the electron motion inside a magnetic trap is more complicated than a pure cyclotron motion. This motion causes the electron to observe different regions of the background field. Hence, the cyclotron frequency of the electron depends on the electron motion inside the trap. This motion also changes the spectral features of cyclotron radiation via the Doppler effect. Second, to have a reliable power calculation the Maxwell equations inside a wave-guide needed to be solved.

In this chapter we first discuss the electron motion inside a magnetic trap. Afterward we use this motion to calculate the CRES spectrum of an electron inside a wave-guide. The model presented in this chapter assists us to fully understand the CRES features in a wave-guide and to take the full advantage of this technique [1].

3.1 Electron's Motion Inside a Magnetic Trap[2]

In the last chapter we showed the importance of a magnetic bottle trap for detecting electron's cyclotron radiation in Project 8. The non-uniformity in the magnetic field not only confines the electron but also introduces nontrivial motions. In this section we will study the electron motion inside a magnetic bottle trap in more details.

---

[1] Some of the content of this chapter is published in [19]

[2] The method used in this section for studying the electron motion inside a non-uniform magnetic field is based on discussions presented in the first chapter of [46] and the second chapter of [23].

3.1.1 Charged Particle in a Non-Uniform Magnetic Field

To find electron's motion in a magnetic field, we need to solve the Lorentz equation in the absence of the electric field [3],

$$\frac{d^2\mathbf{r}}{dt^2} = \frac{e}{\gamma m}\frac{d\mathbf{r}}{dt} \times \mathbf{B}(\mathbf{r}), \tag{3.1}$$

in which γ is the lorentz factor. Solving this equation in the most generic case is challenging. However in the case of slow changes in the magnetic field over a single cyclotron radius,

$$\rho_c \equiv \frac{\gamma m v_0}{eB_0} << L, \tag{3.2}$$

where L is the characterstic length of changes in the magnetic field, we can decouple electron's motion into a fast cyclotron circulation and a slow gyro-center drift,

$$\begin{aligned} \mathbf{r} &= \mathbf{R}(t) + \boldsymbol{\rho}(\mathbf{R}, \mathbf{U}, t, \phi), \\ \mathbf{v} &= \mathbf{U}(t) + \mathbf{u}(\mathbf{R}, \mathbf{U}, t, \phi), \end{aligned} \tag{3.3}$$

in which R and U describe the drift motion while r and u model the fast cyclotron motion. Here we introduced an independent variable ϕ to describe the periodic cyclotron motion. The periodicity of gyration radius and velocity functions with respect to their last variable enforces,

$$\langle \mathbf{u} \rangle = \langle \boldsymbol{\rho} \rangle = 0, \tag{3.4}$$

where angular brackets represent the average over a 2π period in ϕ.

A step by step solution of electron's motion is presented in Appx. A. In that appendix we calculate the first non-zero term for all the quantities in Eq. 3.3. The electron's fast motion can be described by building an orthonormal basis $(\mathbf{e}_1, \mathbf{e}_2, \tilde{\mathbf{b}} \equiv \tilde{\mathbf{B}}/\tilde{B})$ (Eq. A.16),

$$\begin{aligned} \boldsymbol{\rho} &= \rho_c \left[-\mathbf{e}_1 \cos(\Omega_c t + \phi_0) + \mathbf{e}_2 \sin(\Omega_c t + \phi_0)\right] + \mathcal{O}(\epsilon) \\ \mathbf{u} &= v_0 \left[\mathbf{e}_1 \sin(\Omega_c t + \phi_0) + \mathbf{e}_2 \cos(\Omega_c t + \phi_0)\right] + \mathcal{O}(\epsilon). \end{aligned} \tag{3.5}$$

These equations describe a simple cyclotron motion as expected.

---

[3] The intrinsic magnetic moment of the electron is neglected in this calculation.

To find the electron's secular motion, we separate the parallel and perpendicular components. For the parallel part we get (Eq. A.28),

$$\frac{dU_{\parallel}}{dt} = -\frac{\boldsymbol{\mu}}{\gamma m} \cdot \boldsymbol{\nabla} B + \mathcal{O}(\epsilon). \tag{3.6}$$

This equation illustrates that there is an effective force exerted on the electron via the gradient in the magnetic field. This effective force explains the fundamentals of magnetic trapping. Electrons in a local minimum of the magnetic field can be confined using this effective force.

The perpendicular component of the electron's motion is (Eq. (A.32)),

$$\boldsymbol{U}_{\perp} = \frac{\mu}{\gamma m \Omega_c} \boldsymbol{b} \times \boldsymbol{\nabla} B + \gamma \frac{U_{\parallel}^2}{\Omega_c} \boldsymbol{b} \times (\boldsymbol{b} \cdot \boldsymbol{\nabla}) \boldsymbol{b} + \mathcal{O}(\epsilon^2). \tag{3.7}$$

The first term in the above equation is called the "magnetic drift". The non-uniformity in the magnetic field induces a motion which is perpendicular to both the local magnetic field and its gradient. The second term in Eq. (3.7) is known by the name of "curvature drift". This motion is caused by the curvatures in the field lines. This force can be understood by noting that the quantity $(\boldsymbol{b} \cdot \boldsymbol{\nabla})\boldsymbol{b}$ is the curvature vector pointing to the center of the Osculating circle. Therefore this motion is perpendicular to both magnetic field direction and its curvature vector. Combining the two drift velocities gives the general relation,

$$\boldsymbol{v}_{drift} = \frac{u^2/2 + U_{\parallel}^2}{B \Omega_c} \boldsymbol{b} \times \boldsymbol{\nabla} B. \tag{3.8}$$

for the perpendicular component of the secular motion's velocity (Eq. (A.34)).

3.1.2 Electron Motion in a Magnetic Bottle Trap

A magnetic bottle consists of a local minimum in the magnitude of the background magnetic field. If we define an electron's instantaneous pitch-angle, $\theta(t)$, as the angle between the local magnetic field and the electron's momentum, and write down the effective force in Eq. (3.6) as a potential term, the energy for an electron undergoing cyclotron motion can be written as

$$\begin{aligned} E_e &= K_{e\parallel} + \Phi_{magnetic} \\ &= \frac{1}{2}\frac{p_0^2}{m_e}\cos^2\theta(t) + \mu(t)B(t), \end{aligned} \tag{3.9}$$

where p_0 is the magnitude of the electron's initial momentum and μ is the equivalent magnetic moment of the electron, given by

$$\mu(t) = \frac{1}{2}\frac{p_0^2}{m_e}\frac{\sin^2\theta(t)}{B(t)}. \tag{3.10}$$

In the adiabatic regime, where the change in the magnetic field direction is slow compared with the cyclotron frequency, an electron's equivalent magnetic moment is a constant of motion. Electrons with pitch-angles of $90 + \delta\theta$ or $90 - \delta\theta$ degrees have the same motion; therefore we only consider electrons with pitch-angles between 0 and 90 degrees. The pitch-angle approaches 90 degrees for an electron exploring regions of increasing magnetic field, whereas the pitch-angle decreases for an electron approaching the bottom of the trap. For every electron, we define the pitch-angle at the bottom of the trap to be θ_{bot}. Due to conservation of energy, the condition on pitch-angle for a trapped electron is

$$\theta_{bot} \geq \sin^{-1}\left(\sqrt{1 - \frac{\Delta B}{B_{\max}}}\right), \tag{3.11}$$

where $B_{\max}$ is the maximum value of the magnetic field and ΔB is the trap depth.

The trapped electron undergoes an axial motion inside the trap, the frequency of which can be found from Eq. (3.9),

$$\Omega_a^{-1} = \frac{2}{\pi}\int_0^{z_{max}} \frac{\mathrm{d}z}{\sqrt{\frac{2}{m}(E_e - \mu B(z))}}, \tag{3.12}$$

where z_{max} is the maximum axial distance traveled by the electron inside the trap. To further discuss the electron's motion, we consider two specific trap examples. First, we consider an idealized harmonic trap geometry for which an analytical solution is possible. Then we provide a recipe for numerical calculation for any trap geometry. We will use this recipe to study a more realistic trap geometry used in Project 8.

Harmonic Trap

The simplest magnetic bottle is realized with a single trapping coil producing a field anti-parallel to a background field. This geometry can be approximated by an axially parabolic field,

$$\begin{aligned} B_z &= a(\rho) + b(\rho)z^2 \\ B_\rho &= B_\rho(z,\rho). \end{aligned} \tag{3.13}$$

The two Maxwell's equation for magnetic field can be utilized to find the unknowns in the above equation and show that,

$$\begin{aligned} B_z &= B_0\left(1 - \frac{1}{2}\frac{\rho^2}{L_0^2} + \frac{z^2}{L_0^2}\right) \\ B_\rho &= -B_0\frac{\rho z}{L_0^2}. \end{aligned} \tag{3.14}$$

Here L_0 is the characteristic length of the trap. Note that this approximation is accurate for trapped electrons with pitch-angles close to 90 degree that cannot travel to high field regions (Fig. 3.1). For the harmonic field approximation, electrons undergo simple harmonic motion in the axial direction,

$$z(t) = z_{\max}\sin(\Omega_a t), \tag{3.15}$$

in which the axial frequency is determined by the axial velocity of electron at the bottom of the trap,

$$\Omega_a = \frac{v_0 \sin\theta_{\mathrm{bot}}}{L_0}. \tag{3.16}$$

The maximum displacement for the electron is $z_{\max} = L_0 \cot\theta_{\mathrm{bot}}$. Note that electron's axial motion is indifferent to its radial position.

As a result of the axial motion, the magnetic field experienced by the electron changes over time. The change in the magnetic field causes a modulation in frequency of electron's cyclotron motion. For data acquisition systems with time resolution smaller than axial motion's period, an averaged cyclotron frequency is observed. This frequency can be found

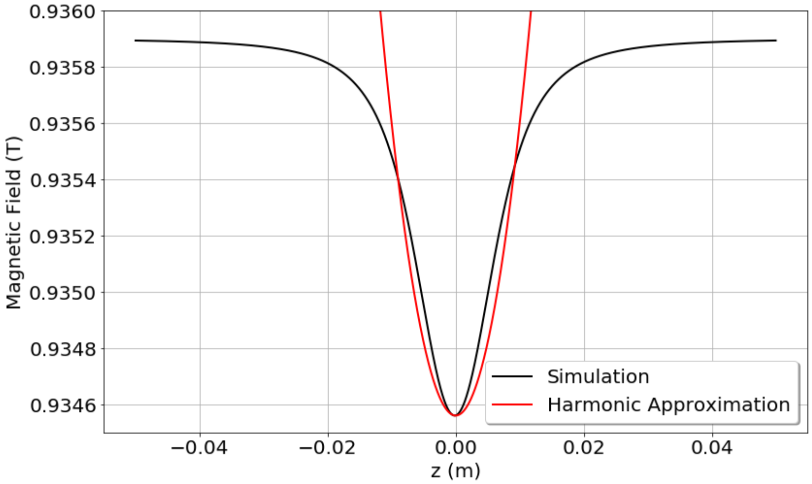

Figure 3.1: Magnetic field profile of a single harmonic trap (black) and the harmonic field approximation given by Eq. 3.14 (red).

by using the magnetic profile by Eq. (3.14) and the electron's equation of axial motion given in Eq. (3.15).

$$\Omega_0 = \frac{eB_0}{\gamma m_e}\left(1 - \frac{\rho^2}{2L_0^2} + \frac{z_{max}^2}{2L_0^2}\right). \tag{3.17}$$

The drift motion for the electron can also be found from Eq. (3.8). For a strong background field the unit vector $\boldsymbol{b}$ can be approximated by $\boldsymbol{e}_3$. Hence,

$$\begin{aligned} \boldsymbol{b} \times \boldsymbol{\nabla} B &= \boldsymbol{e}_3 \times \left(\frac{\partial B}{\partial \rho}\hat{\boldsymbol{\rho}}\right) \\ &= \frac{\partial B}{\partial \rho}\hat{\boldsymbol{\phi}}. \end{aligned} \tag{3.18}$$

Adding the field approximation given in Eq. (3.14) we have,

$$\boldsymbol{b} \times \boldsymbol{\nabla} B = \frac{B_0^2 \rho}{B L_0^2}\left[-1 + \frac{\rho^2}{2L_0^2}\right]\hat{\boldsymbol{\phi}}. \tag{3.19}$$

Because the drift velocity is slow compared to the axial motion, we need to average the above term over a full axial motion's period. However, since ρ does not change in axial motion, the averaged drift velocity is,

$$\boldsymbol{v}_{drift} = \frac{v_0^2 \rho}{L_0^2 \Omega_c} (\sin^2(\theta_{bot})/2 + \cos^2(\theta_{bot})) \left[-1 + \frac{\rho^2}{2L_0^2} \right] \hat{\boldsymbol{\phi}}, \tag{3.20}$$

in which we assumed $\frac{B_0}{B} \simeq 1$. Note that the drift velocity has only a component in ϕ direction which will not change the radial position of the electron. The frequency of this drift motion can be found next,

$$\Omega_m = \frac{v_0^2}{L_0^2 \Omega_c} (\sin^2(\theta_{bot})/2 + \cos^2(\theta_{bot})) \left| -1 + \frac{\rho^2}{2L_0^2} \right| \tag{3.21}$$

Fig.3.2 illustrates how the electron's averaged cyclotron frequency, axial frequency, and drift motion's frequency change with its pitch-angle and radial position in the trap.

Numerical Calculation for a Real Trap Geometry

The trapping field in project 8 apparatus is generated by a number of magnetic coils. The field profile for these traps can be approximated by an array of perfect current coils (Fig. 2.13) for which the exact field profile in known. This field profile can be used to find the frequencies of electron's different motions.

The first step in this calculation is to solve electron's equation of axial motion. Because the relativistic effects are small, we can use the classical equation of motion. Furthermore, because the magnetic field is stationary, the well known relation can be used where,

$$t = \int_{z_0(0)}^{z_0(t)} \frac{\mathrm{d}z'}{\sqrt{\frac{2}{m}(K_e - \mu B(z'))}}. \tag{3.22}$$

The above integral can be used to find the time that it takes the electron to travel from $z(0) = 0$, at the center of the trap to $z(T/4) = z_{max}$. This time is a quarter of axial motion's period, hence,

$$\Omega_a^{-1} = \frac{2}{\pi} \int_0^{z_{max}} \frac{\mathrm{d}z}{\sqrt{\frac{2}{m}(E_0 - \mu B(z))}}. \tag{3.23}$$

Utilizing this information about electron's axial motion, we can find the value of magnetic field at any given time. This knowledge helps us to find the cyclotron frequency at any given

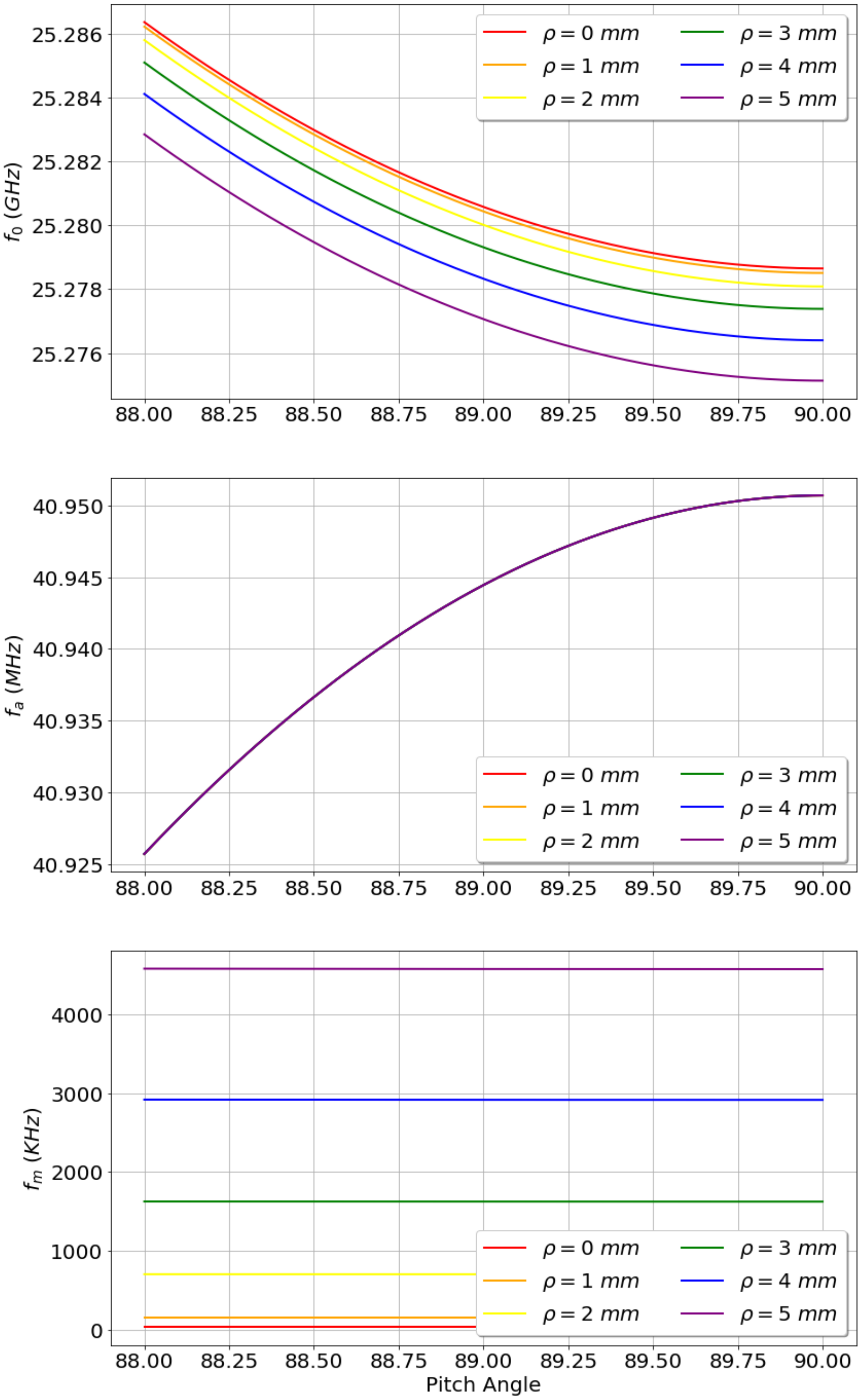

Figure 3.2: Electron's averaged cyclotron frequency (top), axial frequency (middle), and drift motion frequency (bottom) as a function of its pitch-angle for different values of electron radial position inside a harmonic trap.

time. Integrating over the cyclotron frequency gives the cyclotron phase where,

$$\Phi_c(t) = \int_0^t \frac{eB(t')}{\gamma m_e} \mathrm{d}t'. \tag{3.24}$$

One important quantity in this calculation is the averaged value of electron's cyclotron frequency. In the next section we show that this averaged cyclotron frequency is what the data acquisition system assigns to each electron event. The value for the averaged cyclotron frequency is,

$$\Omega_0 = \frac{\Phi_c(T_a)}{T_a}, \tag{3.25}$$

in which T_a is the axial motion's period. Finally, the drift motion's frequency can also be found,

$$\Omega_m = \langle \frac{v_0^2}{L_0^2 \Omega_c} \left(\sin^2(\theta_{bot})/2 + \cos^2(\theta_{bot}) \right) \frac{\partial B}{\partial \rho} \hat{\boldsymbol{\phi}} \rangle, \tag{3.26}$$

in which $\langle ... \rangle$ represents averaging over an axial period. Fig.3.3 shows the frequencies of electron's cyclotron, axial, and drift motions as a function of its pitch-angle at different radii.

3.2 Power Spectral Features of a CRES Signal[4]

In the last section we discussed the motion of an electron in a magnetic bottle trap. This motion has an effect on the signal detected by the receiver via the coupling to the waveguide modes.

Here, a detailed study of power spectrum of a CRES signal in a waveguide is presented. This model provides the knowledge of the rich structure of the signal which can assists us to extract kinematic parameters of the trapped electrons.

---

[4] Here we follow the conventions introduced in section 8.12 of [29]

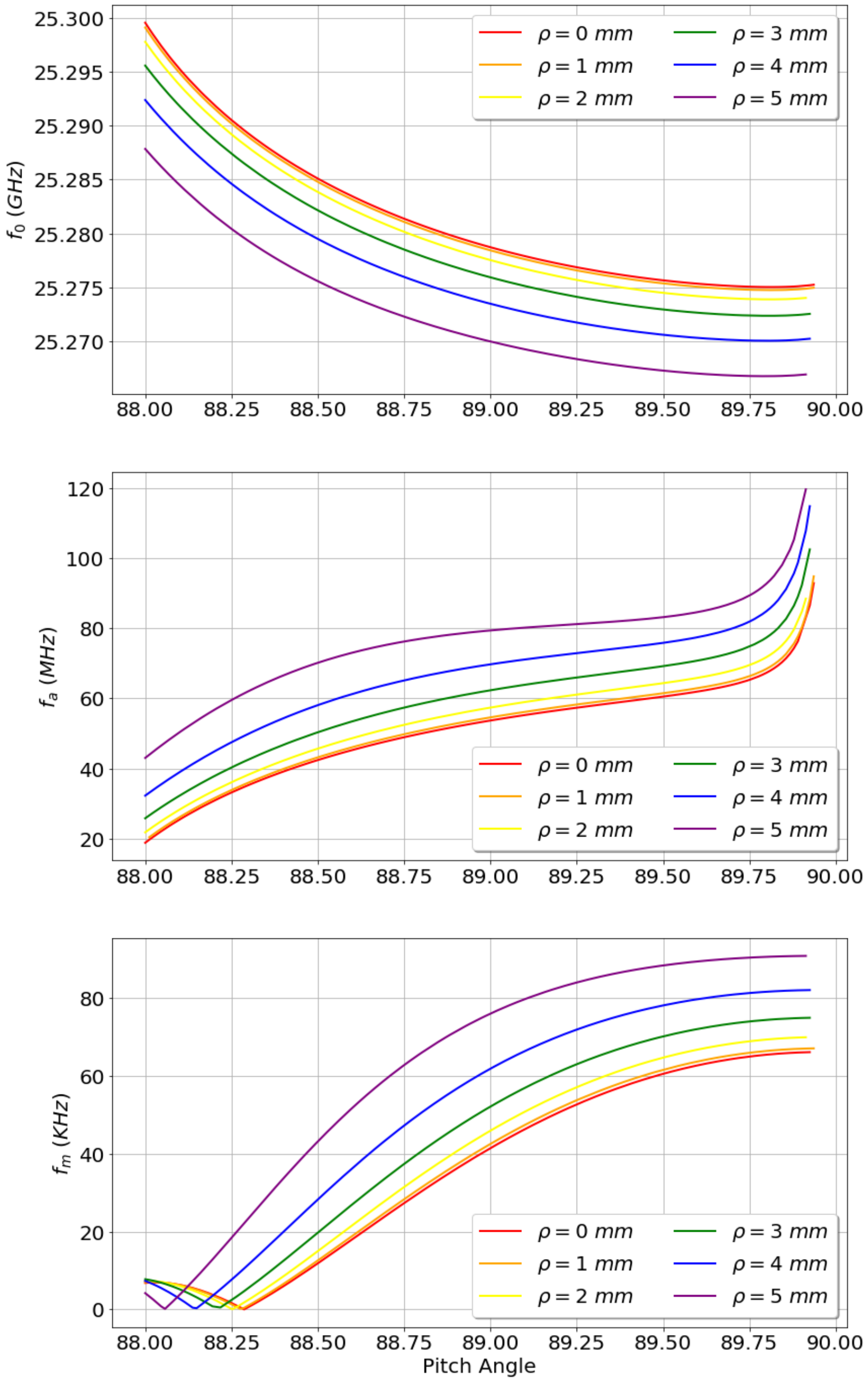

Figure 3.3: Electron's averaged cyclotron frequency (top), axial frequency (middle), and drift motion frequency (bottom) as a function of its pitch-angle for different values of electron radial position inside a phase II trapping coil running at 0.3 *Amps* (Fig. 2.13). The zeros in the drift motion's frequency indicate a reversal in electron direction of drift motion.

3.2.1 Fields in a Waveguide with a Localized Current Source

To find the power radiated in a waveguide, one needs to solve the Maxwell equations in the presence of a source,

$$\begin{aligned}\nabla^2\mathbf{E}(\mathbf{r},t)-\frac{1}{c^2}\frac{\partial^2\mathbf{E}(\mathbf{r},t)}{\partial t^2}&=\frac{1}{\epsilon_0}\nabla\rho(\mathbf{r},t)+\mu_0\frac{\partial\mathbf{J}(\mathbf{r},t)}{\partial t}\\ \nabla^2\mathbf{H}(\mathbf{r},t)-\frac{1}{c^2}\frac{\partial^2\mathbf{H}(\mathbf{r},t)}{\partial t^2}&=\nabla\times\mathbf{J}(\mathbf{r},t).\end{aligned}\tag{3.27}$$

Here we assume that there is no net charge in the waveguide and the fields are generated by a localized current source.

Since the source is localized in the waveguide, the Maxwell equations in Eq. (3.27) reduce to wave equations in the absence of source. These equations were studied thoroughly in [29]. The solutions can be summarized in the form

$$\begin{aligned}\mathbf{E}^{\pm}_{\lambda}(\mathbf{r},t,\omega)&=(\mathbf{E}_{t\lambda}(\mathbf{r}_t)\pm E_{z\lambda}(\mathbf{r}_t)\;\hat{\mathbf{z}})\,e^{i(\pm k_\lambda z-\omega t)}\\ \mathbf{H}^{\pm}_{\lambda}(\mathbf{r},t,\omega)&=(\mathbf{H}_{t\lambda}(\mathbf{r}_t)\pm H_{z\lambda}(\mathbf{r}_t)\;\hat{\mathbf{z}})\,e^{i(\pm k_\lambda z-\omega t)},\end{aligned}\tag{3.28}$$

in which

$$\mathbf{H}_{t\lambda}(\mathbf{r}_t)=\pm\frac{1}{Z_\lambda}\hat{\mathbf{z}}\times\mathbf{E}_{t\lambda}(\mathbf{r}_t),\tag{3.29}$$

where the signs indicate the direction of propagation.

A convenient normalization can be introduced, where

$$\int_{\mathcal{A}}\mathbf{E}_{t\lambda}\cdot\mathbf{E}_{t\mu}\mathrm{d}a=\delta_{\lambda\mu}.\tag{3.30}$$

Eq.(3.29) then implies

$$\int_{\mathcal{A}}\mathbf{H}_{t\lambda}\cdot\mathbf{H}_{t\mu}\mathrm{d}a=\frac{1}{Z_\lambda^2}\delta_{\lambda\mu}.\tag{3.31}$$

Another equation that can be deduced from Eq.(3.30) which is useful in power calculation is

$$\int_{\mathcal{A}}\mathbf{E}_{t\lambda}\times\mathbf{H}_{t\mu}\mathrm{d}a=\frac{1}{Z_\lambda}\delta_{\lambda\mu}.\tag{3.32}$$

These relations also constrain the parallel components of electric and magnetic fields

$$\begin{aligned} &TM\ Modes: \\ &\int_{\mathcal{A}} E_{z\lambda}\cdot E_{z\mu}\mathrm{d}a = -\frac{\gamma_\lambda^2}{k_\lambda^2}\delta_{\lambda\mu} \\ &TE\ Modes: \\ &\int_{\mathcal{A}} H_{z\lambda}\cdot H_{z\mu}\mathrm{d}a = -\frac{\gamma_\lambda^2}{Z_\lambda^2 k_\lambda^2}\delta_{\lambda\mu}, \end{aligned} \tag{3.33}$$

with γ_λ being the mode eigenvalues.

These normalized fields can be used to write a generic solution to source free Maxwell equations,

$$\begin{aligned} \mathbf{E}^{\pm}(\mathbf{r},t) &= \sum_\lambda \int_{-\infty}^{\infty} A_\lambda^{\pm}(\omega)\mathbf{E}_\lambda^{\pm}(\mathbf{r},t,\omega)\mathrm{d}\omega \\ \mathbf{H}^{\pm}(\mathbf{r},t) &= \sum_\lambda \int_{-\infty}^{\infty} A_\lambda^{\pm}(\omega)\mathbf{H}_\lambda^{\pm}(\mathbf{r},t,\omega)\mathrm{d}\omega. \end{aligned} \tag{3.34}$$

The fields are then fully described by the *field amplitude*, $A_\lambda^{\pm}(\omega)$.

To relate the field amplitudes to the current density, $\mathbf{J}$, we introduce a form of Poynting's theorem using the source free Maxwell equations for $\mathbf{E}_\lambda^{\pm}$ and $\mathbf{H}_\lambda^{\pm}$ and Maxwell equations in the presence of the source for $\mathbf{E}$ and $\mathbf{H}$,

$$\nabla\cdot\big(\mathbf{E}\times\mathbf{H}_\lambda^{\pm} - \mathbf{E}_\lambda^{\pm}\times\mathbf{H}\big) = \mathbf{J}\cdot\mathbf{E}_\lambda^{\pm}. \tag{3.35}$$

Taking the volume integral of the two sides of the above equation and utilizing the divergence theorem gives,

$$\int_S \big(\mathbf{E}\times\mathbf{H}_\lambda^{\pm} - \mathbf{E}_\lambda^{\pm}\times\mathbf{H}\big)\cdot\mathbf{n}\ \mathrm{d}a = \int_V \mathbf{J}(\mathbf{r},t)\cdot\mathbf{E}_\lambda^{\pm}\mathrm{d}^3\mathbf{r} \tag{3.36}$$

Now we place the surface, S, so it includes the walls of the waveguide and the two cross section surfaces S_+ and S_- respectively to the right and left of the source. Assuming a perfect conductor for the waveguide's wall and choosing the lower signs in Eq.(3.36), the surface integral on the wall vanishes and we get

$$\begin{aligned} \int_S \big(\mathbf{E}\times\mathbf{H}_\lambda^{\pm} - \mathbf{E}_\lambda^{\pm}\times\mathbf{H}\big)\cdot\mathbf{n}\ \mathrm{d}a &= \int_{S_+} \big(\mathbf{E}^{+}\times\mathbf{H}_\lambda^{-} - \mathbf{E}_\lambda^{-}\times\mathbf{H}^{+}\big)\cdot\hat{\mathbf{z}}\ \mathrm{d}a \\ &+ \int_{S_-} \big(\mathbf{E}^{-}\times\mathbf{H}_\lambda^{-} - \mathbf{E}_\lambda^{-}\times\mathbf{H}^{-}\big)\cdot(-\hat{\mathbf{z}})\ \mathrm{d}a. \end{aligned} \tag{3.37}$$

The second integral is equal to zero. Using Eq.(3.32), the first integral can be calculated,

$$\int_{S_+} \left(\mathbf{E}^+ \times \mathbf{H}_\lambda^- - \mathbf{E}_\lambda^- \times \mathbf{H}^+\right) \cdot \hat{\mathbf{z}} \, \mathrm{d}a = \frac{2}{Z_\lambda} \int_{-\infty}^{\infty} A_\lambda^+(\omega) e^{i(k_\lambda z - \omega t)} \, \mathrm{d}\omega. \tag{3.38}$$

By introducing *Mode Excitation*,

$$B_\lambda^\pm(t) = \int_{-\infty}^{\infty} A_\lambda^\pm(\omega) e^{i(k_\lambda z - \omega t)} \, \mathrm{d}\omega, \tag{3.39}$$

we find that,

$$B_\lambda^\pm(t) = \frac{Z_\lambda}{2} \int_V \mathbf{J}(\mathbf{r}, t) \cdot \mathbf{E}_\lambda^\mp(\mathbf{r}, t, \omega) \mathrm{d}^3\mathbf{r}, \tag{3.40}$$

in which the relation for the lower signs can be proved by choosing the upper signs in Eq.(3.36).

Taking the Fourier transform of the mode excitation we get

$$\tilde{B}_\lambda^\pm(\omega) = \frac{1}{2\pi} \int_{-\infty}^{+\infty} B_\lambda^\pm(t) e^{i\omega t} \mathrm{d}t = A_\lambda^\pm(\omega) e^{\pm i k_\lambda z}. \tag{3.41}$$

Using the above equation we can finally find the field amplitudes

$$\tilde{A}_\lambda^\pm(\omega) = \frac{Z_\lambda}{4\pi} \int_V \int_{-\infty}^{\infty} \mathbf{J}(\mathbf{r}, t) \cdot \mathbf{E}_\lambda^\mp(\mathbf{r}, t, \omega) \; \mathrm{d}t \mathrm{d}^3\mathbf{r}. \tag{3.42}$$

In conclusion, to find the fields in a waveguide in the presence of a localized current source, one needs to find the propagating modes and normalize them according to Eq.(3.30). Then Eq.(3.42) gives the field amplitude associated with the current $\mathbf{J}(\mathbf{r}, t)$. And finally the fields can be found by replacing the field amplitudes in Eq.(3.34).

3.2.2 Radiated Power in a Waveguide

Power is the relevant quantity which is used to detect electrons as we will show in the next chapter. To find the radiated power we simply use the Poynting vector theorem where

$$P^\pm(t) = \int_{\mathcal{A}} \mathbf{E}^\pm(\mathbf{r}, t) \times \mathbf{H}^{*\pm}(\mathbf{r}, t) \cdot (\pm\hat{\mathbf{z}}) \, \mathrm{d}a. \tag{3.43}$$

Replacing the fields from Eq.(3.34) and using the normalization relation in Eq.(3.32), the radiated power is,

$$P^\pm(t) = \sum_\lambda \frac{1}{Z_\lambda} \left|B_\lambda^\pm(t)\right|^2. \tag{3.44}$$

The power can also be studied in the frequency domain. To that aim we define the power spectral density,

$$\tilde{P}^{\pm}(\omega) = \frac{2\pi}{T}\sum_{\lambda}\frac{1}{Z_\lambda}\left|\tilde{B}^{\pm}_{\lambda}(\omega)\right|^2. \tag{3.45}$$

Note that the 2π factor comes from the convention we choose in defining the Fourier transform,

$$\begin{aligned} f(\omega) &= \frac{1}{2\pi}\int_{-\infty}^{+\infty} f(t)e^{i\omega t}\mathrm{d}t, \\ f(t) &= \int_{-\infty}^{+\infty} f(\omega)e^{-i\omega t}\mathrm{d}\omega. \end{aligned} \tag{3.46}$$

With this choice, we can prove that

$$\int_{-\infty}^{+\infty} |f(t)|^2\,\mathrm{d}t = 2\pi\int_{-\infty}^{+\infty} |f(\omega)|^2\,\mathrm{d}\omega. \tag{3.47}$$

The 2π factor on the right hand side of the above equation is the reason for the inclusion of the 2π factor in the definition of power spectral density in Eq.3.45.

3.2.3 Power Spectral Density of a Trapped Electron

In this section we use the proved relations in the last two sections to find the Power Spectral Density of a single electron in a magnetic bottle trap. The current for this single electron in the trap can be written as

$$\mathbf{J}(\mathbf{r},t) = -e\mathbf{v}(t)\delta^3(\mathbf{r}-\mathbf{r}_0(t)). \tag{3.48}$$

In the last chapter we decoupled the electron's motion into three distinct periodic motions. If we assume that the time slot in which the FFT is performed is much smaller than the period of the drift motion, the effect of these two motions can be ignored in a single FFT. Therefore the electron's velocity can be written as

$$\begin{aligned} \mathbf{v}_t(t) &= v_0\sin\theta(t)\left(\cos\Phi_c(t)\hat{\mathbf{r}}_{t1} + \sin\Phi_c(t)\hat{\mathbf{r}}_{t2}\right) \\ v_z(t) &= v_0\cos\theta(t). \end{aligned} \tag{3.49}$$

To find the power, the dot product of electron's velocity and the electric field should be found,

$$\begin{aligned}\mathbf{v}\cdot(\mathbf{E}_{t\lambda}\pm E_{z\lambda}\hat{\mathbf{z}}) = v_0\sin\theta(t)\,(E_{1\lambda}(x,y)\cos(\Phi_c(t))+\\ E_{2\lambda}(x,y)\sin(\Phi_c(t)))\pm\cos\theta(t)E_{z\lambda}(x,y).\end{aligned} \tag{3.50}$$

The z component is equal to zero for Transverse Electric (TE) modes and small in Transverse Magnetic (TM) modes for electrons with pitch-angles close to 90 degree. Hence,

$$\mathbf{v}\cdot(\mathbf{E}_{t\lambda}\pm E_{z\lambda}\hat{\mathbf{z}}) \simeq \frac{v_0}{2}\sin\theta(t)\left((E_{1\lambda}-\mathbf{i}E_{2\lambda})e^{\mathbf{i}\Phi_c(t)}+(E_{1\lambda}+\mathbf{i}E_{2\lambda})e^{-\mathbf{i}\Phi_c(t)}\right). \tag{3.51}$$

Using Eq. (3.42) we can write,

$$\begin{aligned}\tilde{A}^{\pm}_{\lambda}(\omega) &= \frac{Z_\lambda}{4\pi}\int_V\int_{-\infty}^{\infty} -e\mathbf{v}\cdot\mathbf{E}^{\mp}_{\lambda}(\mathbf{r},t,\omega)\ \delta^3(\mathbf{r}-\mathbf{r}_0(t))\ \mathrm{d}t\mathrm{d}^3\mathbf{r}\\ &= -\frac{eZ_\lambda}{4\pi}\int_{-\infty}^{\infty}\mathbf{v}\cdot\mathbf{E}^{\mp}_{\lambda}(\mathbf{r}_0,t,\omega)\mathrm{d}t.\end{aligned} \tag{3.52}$$

The value of electric field should be found at electron's position. However, since the cyclotron radius is much smaller than the waveguide dimensions, the fields can be approximated by their values at the electron's gyro-center. The phase oscillation induced by $\sin\theta(t)$ is also small compared with $\Phi_c(t)$ and can be neglected. Therefore,

$$\begin{aligned}\tilde{A}^{\pm}_{\lambda}(\omega) = -\frac{eZ_\lambda v_0}{8\pi}\sin\theta\Bigg[(E_{1\lambda}-\mathbf{i}E_{2\lambda})\int_{-\infty}^{\infty}e^{\mathbf{i}\Phi_c(t)}e^{\mp\mathbf{i}k_\lambda z_c(t)}e^{\mathbf{i}\omega t}\mathrm{d}t\\ +(E_{1\lambda}+\mathbf{i}E_{2\lambda})\int_{-\infty}^{\infty}e^{-\mathbf{i}\Phi_c(t)}e^{\mp\mathbf{i}k_\lambda z_c(t)}e^{\mathbf{i}\omega t}\mathrm{d}t\Bigg].\end{aligned} \tag{3.53}$$

where the electric fields are calculated at electron's gyro-center.

$z_c(t)$ and $\Phi_c(t)-\Omega_0 t$ are periodic with the electron's axial motion's frequency Ω_a. Therefore these terms can be expanded in two Fourier series

$$e^{i\Phi_c(t)-i\Omega_0 t} = \sum_{m=-\infty}^{\infty}\alpha_m e^{im\Omega_a t} \tag{3.54}$$

and

$$e^{ik_\lambda z_c(t)} = \sum_{m=-\infty}^{\infty}\beta_m(k_\lambda)e^{im\Omega_a t}. \tag{3.55}$$

As a result, the exponential term in Eq. (3.53) can be written as

$$e^{i\Phi_c(t)+ik_\lambda z_c(t)} = \sum_{n=-\infty}^{\infty} a_n(k_\lambda) e^{i(\Omega_0+n\Omega_a)t}, \tag{3.56}$$

in which

$$a_n(k_\lambda) = \sum_{m=-\infty}^{\infty} \alpha_m \beta_{n-m}(k_\lambda). \tag{3.57}$$

These coefficients, a_n, can be computed from a decomposition of the axial motion and the cyclotron phase evolutions into harmonics of the axial frequency. This greatly simplifies the study of the radiated power spectral density. Based on Eq. (3.57), we get

$$\begin{aligned} e^{i\Phi_c(t)-ik_\lambda z_0(t)} &= \sum_{n=-\infty}^{\infty} a_n(-k_\lambda) e^{i(\Omega_0+n\Omega_a)t}, \\ e^{-i\Phi_c(t)-ik_\lambda z_0(t)} &= \sum_{n=-\infty}^{\infty} a_n^*(k_\lambda) e^{-i(\Omega_0+n\Omega_a)t}, \\ e^{-i\Phi_c(t)+ik_\lambda z_0(t)} &= \sum_{n=-\infty}^{\infty} a_n^*(-k_\lambda) e^{-i(\Omega_0+n\Omega_a)t}. \end{aligned} \tag{3.58}$$

Expanding the exponential terms in Eq.(3.53) and using the above Fourier series results in

$$\begin{aligned} \tilde{A}_\lambda^{\pm}(\omega) = -\frac{eZ_\lambda v_0}{2} \Bigg[&(E_{1\lambda} - iE_{2\lambda}) \sum_{n=-\infty}^{\infty} a_n(\mp k_\lambda) \delta(\omega + \Omega_0 + n\Omega_a) \\ &+ (E_{1\lambda} + iE_{2\lambda}) \sum_{n=-\infty}^{\infty} a_n^*(\pm k_\lambda) \delta(\omega - \Omega_0 - n\Omega_a) \Bigg], \end{aligned} \tag{3.59}$$

where $\sin(\theta)$ has been approximated by 1. Next, the power spectral density for the waveguide mode λ, can be calculated using the power spectral density definition in Eq. (3.45). Utilizing conventional techniques of handling δ^2 functions and the relationship between the wavenumber and frequency, we get

$$\begin{aligned} \tilde{P}_\lambda^{\pm}(\omega) = P_{0,\lambda} &\sum_{n=-\infty}^{\infty} \left| a_n \left(\pm \frac{\Omega_0 + n\Omega_a}{v_{p,\lambda}} \right) \right|^2 \\ &\times \left[\delta(\omega - (\Omega_0 + n\Omega_a)) + \delta(\omega + \Omega_0 + n\Omega_a) \right], \end{aligned} \tag{3.60}$$

where $P_{0,\lambda}$ is defined as

$$P_{0,\lambda} = \frac{e^2 v_0^2 Z_\lambda}{8} \left[E_{1\lambda}^2 + E_{2\lambda}^2 \right], \tag{3.61}$$

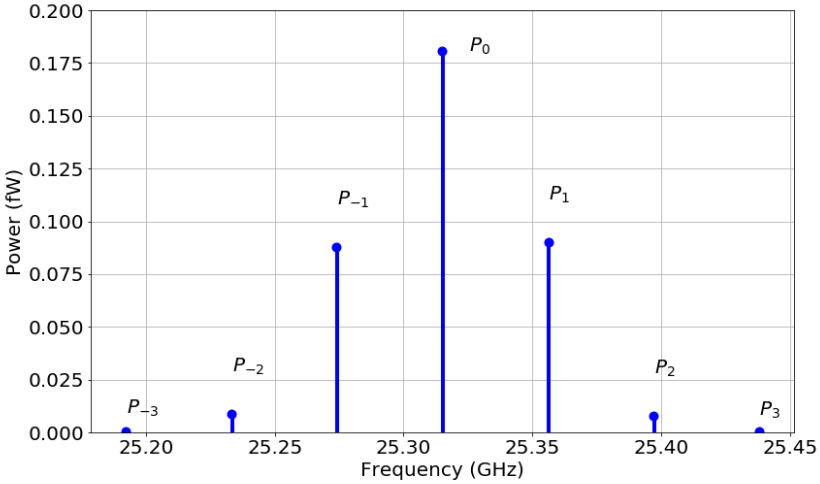

Figure 3.4: The power spectral density for a 17.83 keV electron with a 89.5 degree pitch-angle, trapped in an ideal harmonic trap with $L_0 = 0.3\ m$ in the phase-I waveguide.

and $v_{p,\lambda}$ is the phase velocity in the waveguide for the mode λ. Note that there are possible cross terms between the n^{th} positive and the m^{th} negative frequencies when $n + m = -\frac{2\Omega_0}{\Omega_a}$. Because of the small values of a_ns for large ns, these terms can be neglected.

The measured power spectrum exhibits a comb structure in the frequency domain as shown in Fig. 3.4. For an electron with no axial motion, all the power radiates with a frequency Ω_0. An electron with pitch-angle other than 90 degrees at the bottom of the trap, undergoes axial motion, and as a result some power radiates at the harmonic frequencies which are $n\Omega_a$ away from Ω_0. Eq. (3.60) indicates that the power in the n^{th} harmonic is

$$P_{n\pm} = P_{0,\lambda} \left| a_n \left(\pm \frac{\Omega_0 + n\Omega_a}{v_{p,\lambda}} \right) \right|^2 . \tag{3.62}$$

The signs indicate the direction of power radiation.

It is also beneficial to find the total radiated power of the electron. Assuming a single mode coupling for the electron in the waveguide, we get

$$P_{tot} = P_{0,\lambda} \sum_{i\in\{-1,+1\}} \sum_{n=-\infty}^{\infty} \left| a_n \left(i\frac{\Omega_0 + n\Omega_a}{v_{p,\lambda}} \right) \right|^2 . \tag{3.63}$$

Multiplying Eq.3.56 with its complex conjugate gives

$$1 = \sum_{n=-\infty}^{\infty} \sum_{m=-\infty}^{\infty} a_n(k_\lambda) a_m^*(k_\lambda) e^{i(n-m)\Omega_a t}. \tag{3.64}$$

Performing an integral over the electron's axial period proves that

$$1 = \sum_{n=-\infty}^{\infty} \sum_{m=-\infty}^{\infty} a_n(k_\lambda) a_m^*(k_\lambda) \frac{1}{T_a} \int_0^{T_a} e^{i(n-m)\Omega_a t} dt. \tag{3.65}$$

Hence,

$$1 = \sum_{n=-\infty}^{\infty} \left| a_n(k_\lambda) \right|^2 . \tag{3.66}$$

Using the above result we can find the electron's total radiated power

$$P_{tot} = 2P_{0,\lambda}. \tag{3.67}$$

Note that this result does not depend on any specific trapping geometry. This shows that as the power in the main peak decreases, other peaks in the power spectrum should gain power in order for the total power to remain unchanged. As we will discuss in the next chapter, this result shows that the total radiated power, which manifests in track slope, is independent of electron's pitch-angle[5]. This will assist us in handling trapping related systematics that will be introduced in the next chapter.

3.2.4 Power in particular waveguide geometries

To find the electron's radiated power in a given waveguide geometry, the mode coupling coefficients, $P_{0,\lambda}$, should be calculated. Detailed calculations of $P_{0,\lambda}$ for two interesting examples are presented in Appx. C. For the TE_{10} mode in a rectangular waveguide we get

$$P_{0,TE_{10}} = \frac{Z_{10} e^2 v_0^2}{4wh} \cos^2\left(\frac{\pi x_c}{w}\right), \tag{3.68}$$

---

[5] The validity of this statement depends on the validity of Eq. (3.59) in which we approximated $\sin(\theta)$ by one. This is not valid for deep traps with the potential to trap electrons with lower pitch-angles.

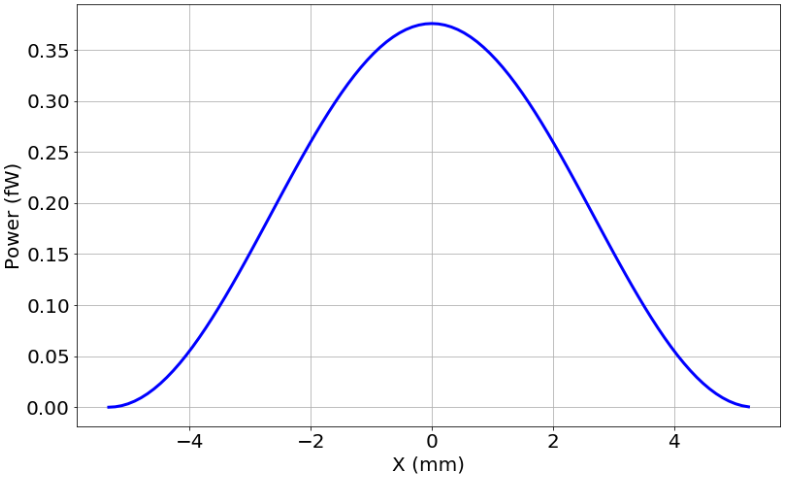

Figure 3.5: A 17.83 keV electron's mode coupling to the fundamental mode of the phase-I rectangular waveguide.

in which Z_{10} is the TE_{10} mode impedance, v_0 is the electron velocity, w and h are the waveguide's width and height, defined to be along x and y directions respectively, and x_c is the x position of the electron's gyrocenter. Fig.3.5 illustrates how the electron's coupling changes along the waveguide axis.

For the TE_{11} mode in a circular waveguide we get

$$P_{0,TE_{11}} = \frac{Z_{11}e^2v_0^2}{8\pi\alpha}\left(J_1'^2(k_c\rho_c) + \frac{1}{k_c^2\rho_c^2}J_1^2(k_c\rho_c)\right), \tag{3.69}$$

in which Z_{11} is the TE_{11} mode impedance, ρ_c defines the radial position of the gyrocenter of the electron in cylindrical coordinates, k_c is the wavenumber for the cutoff frequency of the mode, and α is a constant defined in Eq. (C.8).

It is also beneficial, as we will discuss in the next chapter, to find the mode coupling for the second mode in a circular waveguide. For TM_{01} mode we get,

$$P_{0,TM_{01}} = \frac{Z_{01}e^2v_0^2}{16\pi\beta}J_0'^2(k_c\rho), \tag{3.70}$$

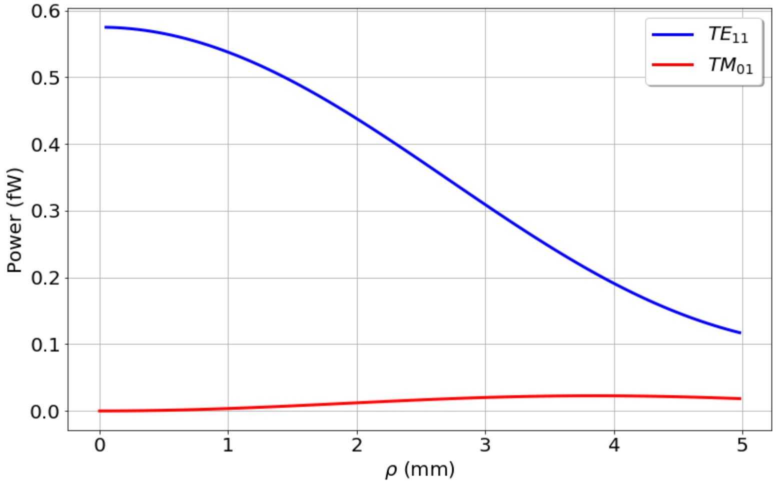

Figure 3.6: A 17.83 keV electron's mode coupling to the two first modes of the phase II circular waveguide.

where β is a constant defined in Eq.(C.12). Fig.3.6 compares the mode couplings of an electron to the first two modes of the phase II circular waveguide.

3.2.5 Effects of Waveguide Reflection

In our discussion of waveguides we have assumed infinite length, whereas any experimental realization of a CRES experiment must be finite in length. Allowing that one end of the waveguide must have a receiver, we are left with several options for the treatment of signals at the other end.

One option is to add a second receiver. The signal observed by each receiver is then available for analysis, at the cost of supporting two receiver systems. Another option is to install a terminator on one end of the waveguide. The receiver will detect only half of the electron's radiated power and the signal will be the same as the case of the infinite waveguide. The final option is to install a conductive short to the end of the waveguide, reflecting signals back to the receiver. The first two options have been already analyzed. In this section we calculate the effects of the short on the power spectral density of the CRES signal.

The total mode excitation at the receiver, $\tilde{B}_\lambda(\omega)$, is a superposition of the direct wave, $\tilde{B}^+_\lambda(\omega)$, and the reflected wave, $\tilde{B}^-_\lambda(\omega)$. The reflection induces a phase shift of 180 degrees on the reflected wave. As a consequence, the total mode excitation at the receiver can be written as

$$\begin{aligned}\tilde{B}_\lambda(\omega) &= \tilde{B}^+_\lambda(\omega) + \tilde{B}^-_\lambda(\omega)e^{i\pi} \\ &= \tilde{B}^+_\lambda(\omega) - \tilde{B}^-_\lambda(\omega).\end{aligned} \tag{3.71}$$

Using the definition of $\tilde{B}^\pm_\lambda(\omega)$ given by Eq. (3.2.1), we get

$$\tilde{B}_\lambda(\omega) = A^+_\lambda(\omega)e^{ik_\lambda z_r} - A^-_\lambda(\omega)e^{ik_\lambda(2|z_s - z_t| + z_r)}, \tag{3.72}$$

where the expression is being evaluated at the receiver's position, z_r, and z_s and z_t are the positions of the reflector and the trap center respectively. The power spectral density then follows by using Eq. (3.45),

$$\begin{aligned}P_\lambda(\omega) = 4P_{0,\lambda} \sum_{n=-\infty}^{\infty} & \left| a_n\left(\frac{\Omega_0 + n\Omega_a}{v_{p.\lambda}}\right)\right|^2 \\ & \cos^2\left[(z_t - z_s)\frac{\Omega_0 + n\Omega_a}{v_{p.\lambda}}\right] \\ & \left[\delta(\omega - (\Omega_0 + n\Omega_a)) + \delta(\omega + \Omega_0 + n\Omega_a)\right].\end{aligned} \tag{3.73}$$

Here we assumed that the trap is symmetric, in which case $a_n(-k)$ can be written in terms of $a_n(k)$ as in Eq. (B.8) (see Appx. B).

This power spectrum still has a comb structure, similar to the one in the absence of a reflector at the end of the waveguide. However, the amplitude of each peak is now modulated with an extra $\cos^2$ factor, which depends on the distance between the reflector and trap center, $z_t - z_s$. Therefore, while the introduction of a reflector increases the total power collected by the receiver, it also introduces a frequency-dependent amplitude for each peak in the power spectrum.

3.2.6 Trapping Geometries

In the last Sections, we built the foundation for calculating the CRES signal's spectral features. From the obtained equations, it is clear that it is impossible to extract a simple analytical solution that is valid and usable for every trap configuration. Therefore, in this section we describe a step-by-step procedure to obtain the spectral properties of a CRES signal. We will then apply this procedure to the idealized harmonic trap geometry. Then we derive numerical solutions for a more complicated geometry following these steps:

- An appropriate field approximation $B(z)$ must be found. In some cases, where the expression of the exact magnetic field is complex, one can consider using a piecewise approximation of the field.

- With the assumed field profile, the electron's equation of axial motion, Eq. (3.9), can be solved. Since the effective potential in this equation depends only on the axial position of the electron, we can find a general solution,

$$t = \int_{z_0(0)}^{z_0(t)} \frac{\mathrm{d}z'}{\sqrt{\frac{2}{m}(K_e - \mu B(z'))}}. \tag{3.74}$$

- Once the axial motion of the electron is calculated, the axial frequency follows. For the special case of a symmetric trap, we find

$$\Omega_a^{-1} = \frac{2}{\pi} \int_0^{z_{max}} \frac{\mathrm{d}z}{\sqrt{\frac{2}{m}(E_0 - \mu B(z))}}. \tag{3.75}$$

- Once the axial position of the electron is found at any given time, the value of the magnetic field experienced by the electron at that time, $B(t)$, follows. Finally, the cyclotron phase is found to be

$$\Phi_c(t) = \int_0^t \frac{eB(t')}{\gamma m_e} \mathrm{d}t'. \tag{3.76}$$

- To find the power in each peak, the Fourier coefficients introduced in Eq. (3.56) should be determined by
$$a_n = \frac{1}{T_a}\int_0^{T_a} e^{i(\Phi_c(t)+k_\lambda z(t))}e^{-i(\Omega_0+n\Omega_a)t}\mathrm{d}t, \tag{3.77}$$
in which Ω_0 is the average cyclotron frequency given by
$$\Omega_0 = \frac{\Phi_c(T_a)}{T_a}. \tag{3.78}$$

- The power in each peak of the spectrum can be determined, using Eq. (3.62),
$$P_n = P_{0,\lambda}|a_n|^2. \tag{3.79}$$

- Finally, the total power radiated by the electron can be calculated by summing over the power of all peaks. This power defines the track slope that will be introduced in the next chapter.

Power spectrum in a "harmonic trap"

The harmonic trap geometry was introduced in Sec.3.1.2. In that section we showed that electron's axial position follows simple harmonic motion (Eq.(3.15)). The equation of axial motion can be used to find the magnetic field seen by the electron as a function of time, where
$$B_z(t) = B_0\left(1 - \frac{\rho^2}{2L_0^2} + \frac{z_{\mathrm{max}}^2}{2L_0^2} - \frac{z_{\mathrm{max}}^2}{2L_0^2}\cos(2\Omega_a t)\right). \tag{3.80}$$
Therefore the cyclotron frequency of a trapped electron inside the harmonic trap is
$$\Omega_c(t) = \frac{eB_0}{\gamma m_e}\left(1 - \frac{\rho^2}{2L_0^2} + \frac{z_{\mathrm{max}}^2}{2L_0^2} - \frac{z_{\mathrm{max}}^2}{2L_0^2}\cos(2\Omega_a t)\right). \tag{3.81}$$
The last term describes the modulation in frequency and the first three terms determine the average cyclotron frequency,
$$\Omega_0 = \frac{eB_0}{\gamma m_e}\left(1 - \frac{\rho^2}{2L_0^2} + \frac{z_{\mathrm{max}}^2}{2L_0^2}\right). \tag{3.82}$$

The cyclotron phase can be calculated by integrating over the cyclotron frequency,

$$\Phi_c(t) = \Omega_0 t + q \sin(2\Omega_a t), \tag{3.83}$$

in which the magnitude of the modulation is

$$q = -\frac{eB_0}{\gamma m_e} \frac{z_{\text{max}}^2}{4L_0^2 \Omega_a}. \tag{3.84}$$

To find the power spectrum of the electron's radiation, Fourier coefficients in Eq. (3.56) are needed. The coefficients can be calculated using the Jacobi-Anger expansion. Therefore we get

$$\begin{aligned} e^{i\Phi_c(t)+ik_\lambda z_0(t)} &= e^{i(\Omega_0 t + q\sin(2\Omega_a t) + k_\lambda z_{\text{max}} \sin(\Omega_a t))} \\ &= \sum_{m,p=-\infty}^{\infty} J_m(q) J_p(k_\lambda z_{\text{max}}) e^{i(\Omega_0 + (2m+p)\Omega_a)t}, \end{aligned} \tag{3.85}$$

where J_n is the n^{th} Bessel function of the first kind. Thus, the power for each harmonic can be found from Eq. (3.79) by squaring

$$a_n(k_\lambda) = \sum_{m=-\infty}^{\infty} J_m(q) J_{n-2m}(k_\lambda z_{\text{max}}) \tag{3.86}$$

and using the appropriate $P_{0,\lambda}$ as found in section 3.2.4. Let us note that these coefficients, a_n, correspond to the coefficients α_m and β_m defined by Eq. (3.54) and Eq. (3.55). The relative magnitude of the main peak and sideband powers for typical parameters are shown in Fig. 3.7.

It can be shown from Eq. (3.11) that a 4 mT deep trap in a 1 T background magnetic field can trap electrons with pitch-angles as small as 86 degrees. In this case, the magnitude of the modulation of the magnetic field experienced by the electron, q, is smaller than 0.6, while the Doppler effect's modulation, $k_\lambda z_{max}$, can be as large as 10.5. Therefore, $J_m(q)$ can be approximated with δ_{m0}. In this case, the power spectrum can be simplified to

$$\begin{aligned} \tilde{P}_\lambda^{\pm}(\omega) = P_{0,\lambda} &\sum_{n=-\infty}^{\infty} J_n^2(k_\lambda z_{max}) \\ &\times \left[\delta(\omega - (\Omega_0 + n\Omega_a)) + \delta(\omega + \Omega_0 + n\Omega_a)\right]. \end{aligned} \tag{3.87}$$

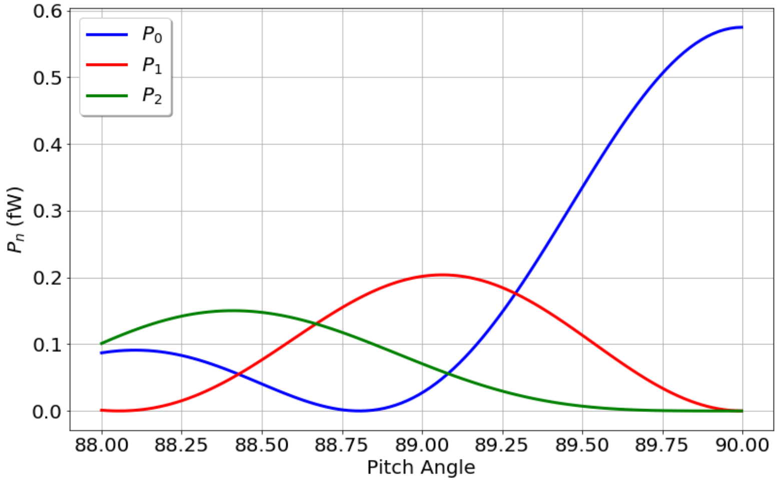

Figure 3.7: The power in the first three peaks of a 17.83 keV electron spectrum at the center of phase II circular waveguide, trapped in an ideal harmonic trap.

This approximation works best for shallow traps in which $\frac{\Delta B}{B} < 0.002$.

Power spectrum in a real trap geometry

In Sec.3.1.2 we discussed electron motion in a real trap geometry. We can now utilize the recipe given in Sec.3.2.6 to numerically calculate the power spectrum for this electron.

Fig. 3.8 shows the power propagating in the first three peaks of a 17.83 keV electron's power spectrum. The electron resides at the center of the phase II circular waveguide. This plot shows how the power in these three peaks changes with the value of the pitch-angle. Note that as the main peak loses power, the first peak gains power. This is an illustration of the fact that the total radiated power is not pitch-angle dependent as it was proved in Eq. (3.67) for any given trap geometry.

Fig. 3.9 shows how the main peak power of a 17.83 keV electron changes as a function of its pitch-angle at different radii. The reduction in the total power is caused by the change in the electron's coupling to the circular waveguide mode as was illustrated in Fig. 3.6. The

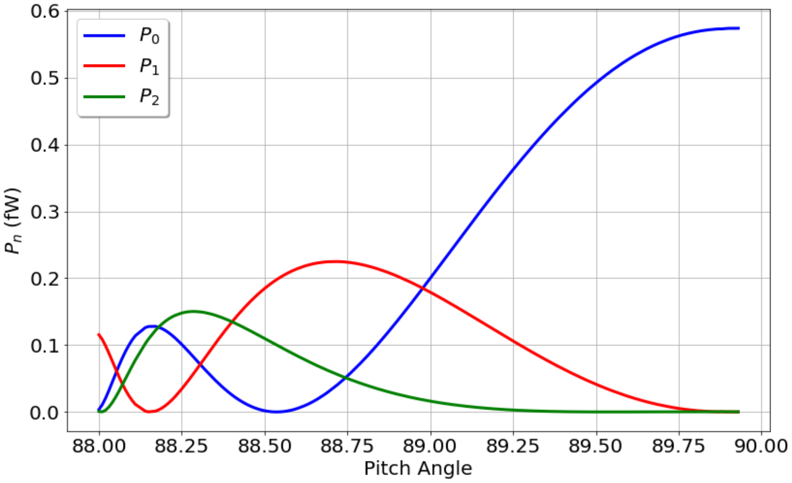

Figure 3.8: The power in the first three peaks of a 17.83 keV electron spectrum at the center of phase II circular waveguide, trapped in a phase II trapping coil running at 0.3 $Amps$ (Fig. 2.13).

functional form of the power also changes due to the different field profiles traversed by the electron at different radii.

In Fig.3.10 we plotted the changes in the main peak's normalized power and the averaged cyclotron frequency for a range of pitch-angles and at different radii. The key feature in this plot is that the normalized power is independent of electron's radius. Furthermore, the total electron's radiated power is independent of its pitch-angle. Hence these two features in the electron's power spectrum, the total radiated power and the main peak's normalized power, can be used to find electron's kinematic features. In the next chapter we will use this feature to improve the energy resolution in Project 8 detector.

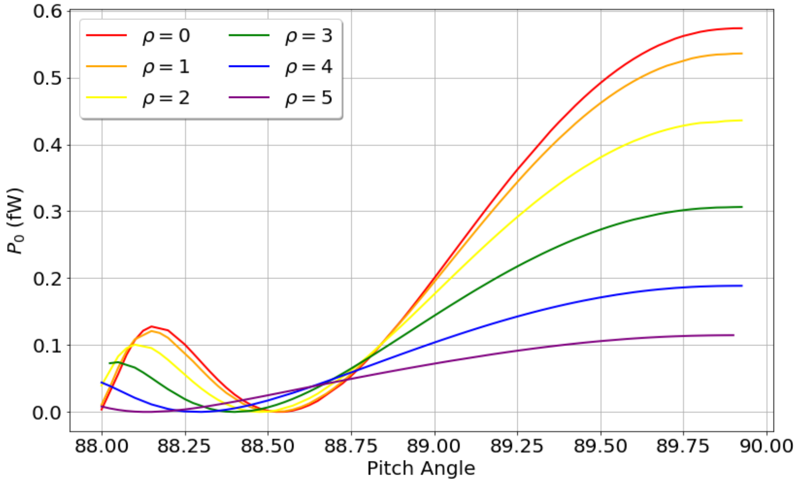

Figure 3.9: The main peak's power of a 17.83 keV electron spectrum as a function of its pitch-angle, at different radii. The electron is assumed to be in the phase II circular waveguide trapped in a phase II trapping coil running at 0.3 *Amps* (Fig. 2.13).

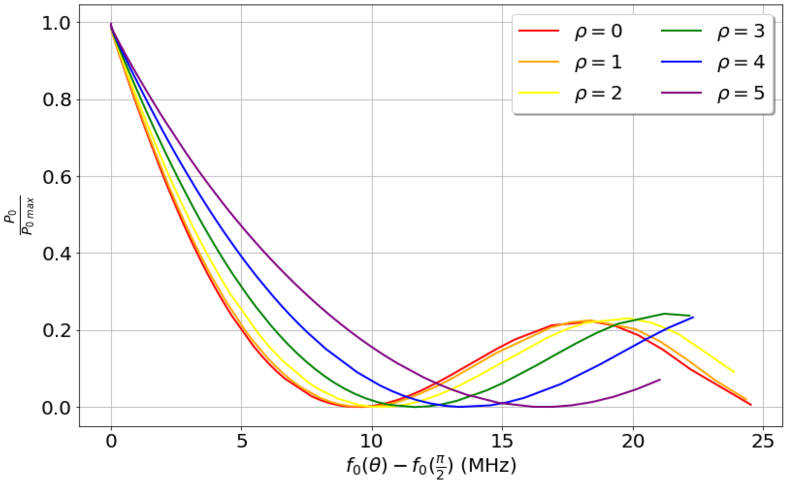

Figure 3.10: The main peak's power of a 17.83 keV electron spectrum as a function of its averaged cyclotron frequency, at different radii. The electron is assumed to be in the phase II circular waveguide trapped in a phase II trapping coil running at 0.3 $Amps$ (Fig. 2.13). All the lines are drawn for pitch-angle values in the range of $(88°, 90°)$.

Chapter 4

CALIBRATION DATA ANALYSIS USING CONVERSION ELECTRONS FROM ^{83M}KR

In the last chapter we constructed a phenomenological model that describes a magnetically trapped electron's radiation inside a waveguide. In this chapter we present the krypton data that is taken with the project 8 CRES demonstrator, explained in Ch. 2. We will discuss the ways that the knowledge built in the last chapter can assist us to better understand this data.

The analysis process in the project 8 collaboration consists of two main parts. In the first step the recorded data is presented in a spectrogram. Any excess in the power caused by the electron radiation is detected at this point. This part is managed by a set of algorithms which are named *Track and Event Reconstruction.*

In the second step the recorded quantities from the first step are used to construct the krypton spectrum. A detailed discussion of these two stages is the main objective of this chapter's discussion.

4.1 Track and Event Reconstruction

As it was mentioned in section 2.3, Project 8 uses two stages of low noise amplifiers to detect the CRES signal which has $\sim 1fW$ of power. A mixer stage down-convert the amplified signal from the K band to the L band of the RF spectrum. Finally, the down converted signal digitized by a ROACH FPGA. The ROACH data acquisition system has a built in Fourier transform operator. This operator is used to trigger on high power bins in the frequency domain and save the full time series of surrounding data.

After digitization, the time series data are divided into time slices. An offline Fourier

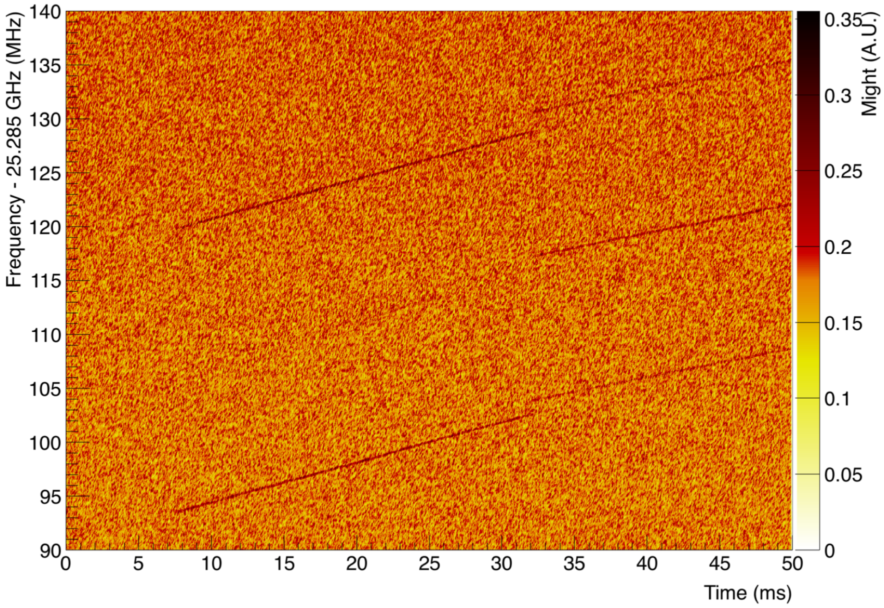

Figure 4.1: An electron spectrogram recorded by the ROACH system. The spectrogram contains information about the time (on the X-axis), frequency (on the Y-axis), and power (color code). Five tracks of excess in power can be detected in this event.

transform converts the data from the time domain into the frequency domain. The combined information of time, frequency, and power can be shown in a spectrogram plot (Fig. 4.1).

The most apparent feature in this spectrogram is the presence of five distinct *Tracks* with excess in power over the noise flour. These Tracks are the manifestation of the peaks in the CRES spectrum discussed in Sec. 3.2, spanned over many time slices. The tilt in the tracks is representing the electron's power loss to radiation. The averaged electron's cyclotron frequency over a complete period of the its axial motion, including the power loss, is

$$\begin{aligned} f &= \frac{1}{2\pi}\frac{e\tilde{B}}{m_e + E_{kin}(t)/c^2} \\ &= \frac{1}{2\pi}\frac{e\tilde{B}}{m_e + (E_0 - P_{tot}t)/c^2} \\ &\simeq \frac{1}{2\pi}\frac{e\tilde{B}}{m_e + E_0/c^2}\ (1 + \frac{P_{tot}t}{E_0 + mc^2}) \\ &= f_0 + S \cdot t. \end{aligned} \tag{4.1}$$

Where the approximation in the third line is valid because the radiated power of an electron in the time scale of a track in Project 8 ($\sim 1\ ms$) is less than $10\ eV$ and is smaller than the mass of the electron ($\sim 0.5\ MeV$). The $\tilde{B}$ represents the averaged value of magnetic field traversed by the electron inside the magnetic field. Eq.(4.1) shows that the start-frequency of the track, f_0, is exactly equal to the averaged value of cyclotron frequency introduced in Eq. (3.25). Furthermore, the *Slope* of the track, S in Eq.(4.1), is related to the total radiated power via,

$$S = \frac{f_0}{m_e c^2 + E_0} P_{tot}. \tag{4.2}$$

The first task in the Project 8's analysis chain is to detect these electron tracks in a spectrogram. Furthermore, the five tracks shown in Fig. 4.1 are from a single electron and needed to be grouped together appropriately. As the electron loses energy in a scattering off the residual gas molecules in the gas cell, its cyclotron frequency jumps in the spectrogram. For example the electron detected in Fig. 4.1 has experienced one scattering. Failure in grouping Tracks which belong to a single electron *Event*, results in misidentifying the electron's initial energy at the instant of decay. An ideal Track and Event reconstruction algorithm should be capable of detecting short tracks with low power without misidentifying noise as an independent fake Track.

The first step in the track reconstruction after creating the spectrogram, is to remove the background shape. This shape is a result of different factors including the thermal noise in the waveguide, transfer function of different components of the receiver chain, and the digital filters applied in the data acquisition system. By normalizing the background one insures a time and frequency independent detection probability for Tracks in the spectrogram.

The standard background shape is shown in Fig. 4.2. Since the background shape varies relatively slowly with frequency, third-order splines are used to fit its average amplitude and variance. The normalized power in each bin is then,

$$P'_i = \frac{P_i - \mu_i}{\sigma_i}, \tag{4.3}$$

where P'_i, P_i, μ_i, and σ_i are respectively *Normalized Power*, un-normalized power, average

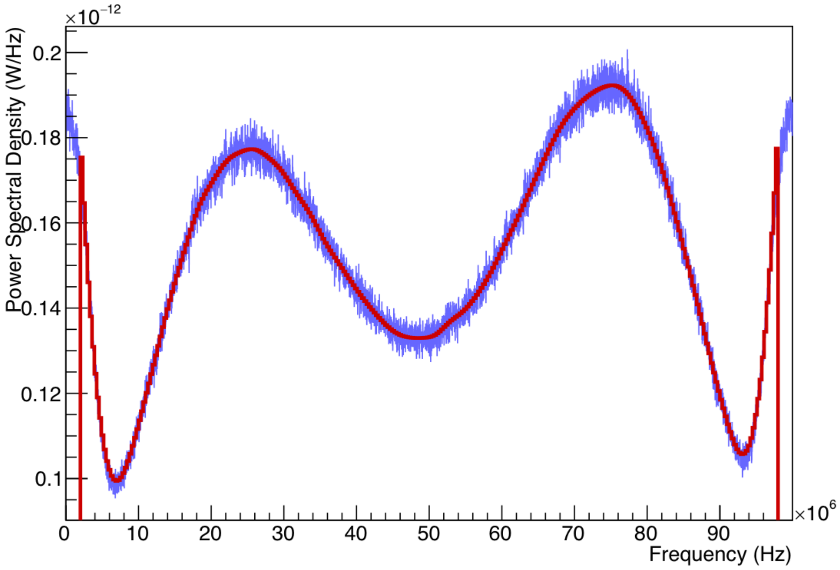

Figure 4.2: The 3rd-order spline fit to an average power spectrum amplitude.

amplitude in the i-th bin, and the standard deviation in that bin.

The next step in the Track reconstruction procedure is to remove the low-power bins in the spectrogram. This results in a *sparse spectrogram* one example of which is shown in Fig. 4.3.

The sparse spectrogram then passed to the *sequential track finder*(STF). The STF algorithm processes the data in each time slice separately. If STF finds a point which passes the power threshold, it initializes a line. STF then chooses an initial slope, which has shown to be insignificant in the success of track clustering. In the next slice the STF appends any point in the sparse spectrogram to the line if the condition,

$$f_i - (f_{end,l} + s_l \cdot (t_i - t_{end,l})) < \Delta f, \tag{4.4}$$

is satisfied, where f_i, t_i, $f_{end,l}$, $t_{end,l}$, s_l, and Δf are respectively, new point's frequency, new point's time, line's last point's frequency, line's last point's time, line's assigned slope, and the fixed frequency acceptance. When a new point is added to the line, the slope is re-evaluated accordingly,

$$s_l = \frac{\sum_{i=1}^{N} \frac{p_i - \mu_i}{\sigma_i} \cdot \frac{f_i - f_{start,l}}{t_i - t_{start,l}}}{\sum_{i=1}^{N} \frac{p_i - \mu_i}{\sigma_i}}. \tag{4.5}$$

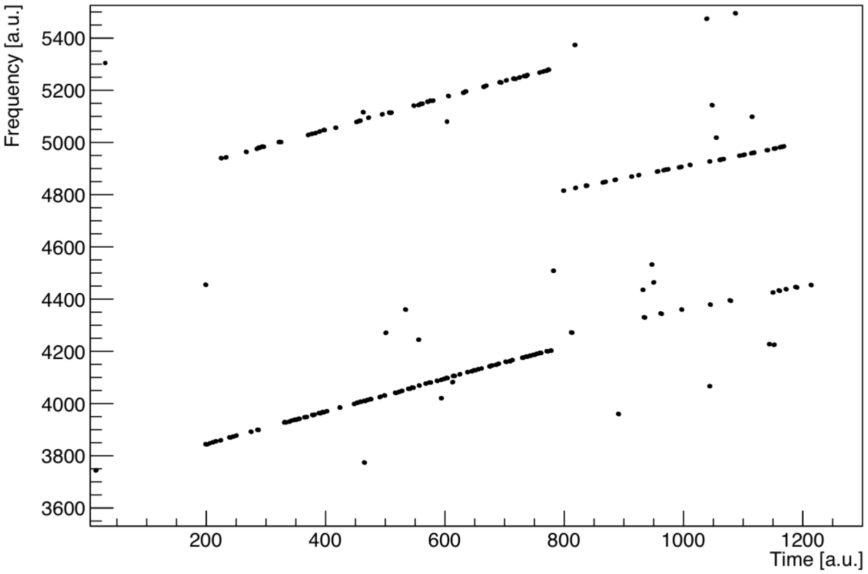

Figure 4.3: The sparse spectrogram which is the result of passing the spectrogram shown in Fig. 4.1 through a high bin power cut.

If a point is found that exceeds the power threshold without satisfying Eq. (4.4), a new line will be started. A line will be inactive if the distance in time between its last point and the current time slice exceeds a fixed time-gap-tolerance. After a line is inactive its start and end points are trimmed until they satisfy a configurable trimming threshold. If the line still contains enough points it will be passed to the next stage.

While the STF is efficient in detecting physical tracks, it occasionally identifies a single track as multiple tracks due to power fluctuations in the track. Therefore a *track segment clustering* (TSC) algorithm is used to recombine these broken tracks. The TSC algorithm recombines two tracks if they satisfy one of the below conditions:

- The endpoint of a track coincides with the start point of another track in time, their frequency difference is small, and their slopes are similar.

- The time distance between the start point of a track and the endpoint of the other track is smaller than a certain limit, the frequency of the extrapolation of the first track at the start time of the second track is close enough to the start-frequency of the second track, and their slopes are similar.

In this case the line will be registered as a track and its properties including power, slope, start-frequency, and etc, will be calculated.

The final stage in track and event reconstruction is to regroup the detected tracks from a single electron into an event. Electrons can generate multiple tracks in two different topologies. The first topology is where there exist parallel tracks in the spectrogram which have similar slopes and start and end time. These tracks which are called *sidebands* appear in the spectrogram whenever two peaks in the electron spectrum have enough power to stand above the noise flour. These event cluster to a single *Multi-peak track* (MPT) based on their start and end time in the spectrogram.

The second topology occurs when the electron scatters off a residual gas molecule. If the end time of the first MPT event is close enough to the start time of the second MPT event, then the two events will be re-clustered into a single event.

4.1.1 Validating the Track and Event Reconstruction Algorithm

The algorithm discussed in the last section cannot detect all the tracks in a spectrogram, mainly due to the presence of the noise in the system. The shorter and less-powered tracks are the ones which have the least probability for detection. In order to quantitatively study the efficiency of the track and event reconstruction algorithm, we have simulated events using our simulation package [20]. One of the main objectives of this study is to investigate the measurement precision of the tracks reconstructed features such as slope and power. Furthermore, the detection efficiency of the reconstruction algorithm can be studied as a function of different track properties.

The fake event generator utilizes the Locust software to generate realistic events with simulated power, start-frequency, and time length. However the value of track slope is an input for the simulation software. The fake event generator is used to simulate events with various values for the track slope. Afterwards, the simulated events are sent to the official

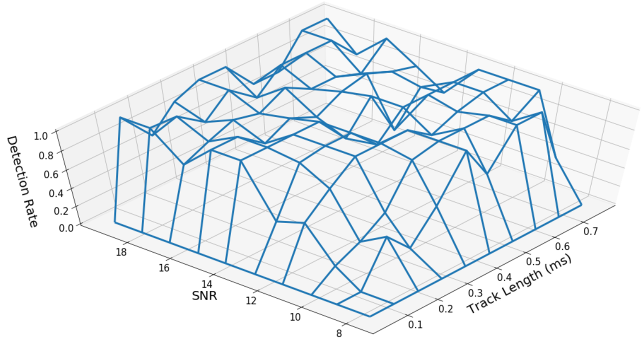

Figure 4.4: The detection rate (defined as the number of events detected over the number of simulated events) for tracks with different values of power and length. The reconstruction algorithm has the best performance for high-powered and longer tracks.

track and event reconstruction software. The comparison between the simulated events and their reconstructed counterparts, assists us to quantitatively validate the track and event reconstruction algorithm.

The success of the track and event reconstruction algorithm depends strongly on the power and time length of the electron tracks in the spectrogram. Fig. 4.4 shows how the detection rate changes with track power and time length for a specific track and event reconstruction configuration. It is apparent that the very low power tracks cannot be detected by the track and event reconstruction algorithm. The shorter tracks are also harder to detect. However, the reconstruction algorithm is functioning effectively for longer and more powerful tracks.

Fig. 4.5 illustrates that the track slope is also a relevant factor in the detection probability. The higher slope tracks have a lower probability of detection by the track reconstruction algorithm.

Next we can examine the precision of track and event reconstruction for the detected events. Since the energy of the electron is reconstructed using the event's start-frequency,

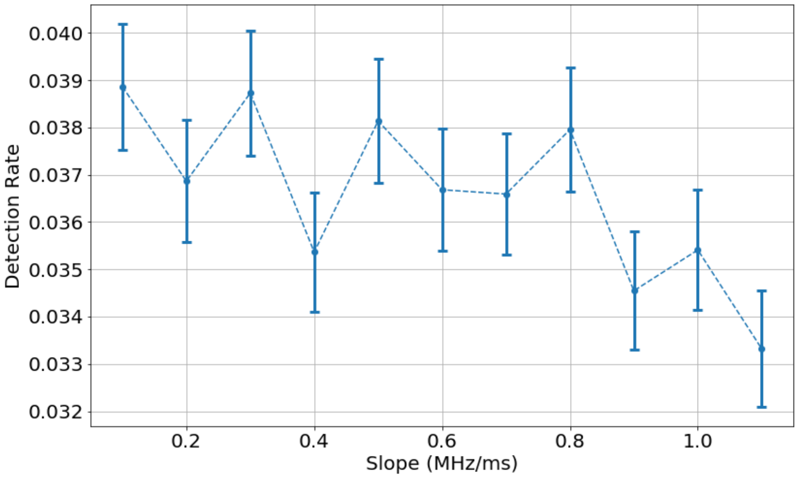

Figure 4.5: The detection rate for tracks with different values of slope.

validating its measurement accuracy has the highest priority. Fig. 4.6 is the histogram for the reconstructed start-frequency error. The track and event reconstruction algorithm often register a higher start-frequency. The Gaussian distribution in Fig. 4.6 is caused by the inefficiency of the algorithm in detecting the initial points in the first track of an electron event. Fig. 4.10 illustrates that the reconstructed frequency error for longer tracks is larger. This is due to the fact that the longer tracks provide the probability for the track reconstruction to miss many bins in the track without missing the entire track.

The track power measurement is the next key aspect of the reconstruction algorithm which should be validated. Fig. 4.7 plots the simulated vs. the reconstructed signal to noise ratio. The red line is the result of a fit to the points with simulated signal to noise ratio greater than 12.5. The reason for applying this cut is to avoid the hard cut that the reconstruction algorithm applies around the signal to noise ratio of 8. One might expect the fit to have a slope around one and a y-intercept around zero. The reason for the smaller slope in the linear fit is that the tracks can go through multiple bins in a single time slot of the spectrogram. However the power is constructed with one bin in each time slot. Therefore the reconstructed power is a fraction of the simulated power. Furthermore, the non-zero y-intercept is the result of the addition of the noise power to the track.

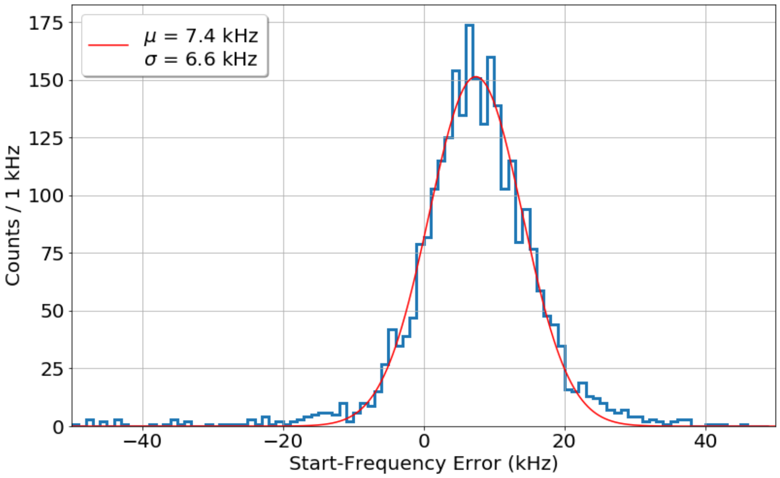

Figure 4.6: The start-frequency measurement error(defined as the difference between the reconstructed and the simulated tracks' start frequencies) histogram.

The relative deviation of reconstructed SNR from the line fit in Fig. 4.7 is defined as the SNR error percentage. Fig. 4.8 histograms this error percentage for the power measurement. The error histogram can be approximately fitted with a Gaussian approximately centered at zero with a $\sim 13\%$ standard deviation. The most relevant factor in power measurement accuracy is the track length. Fig. 4.10 illustrates how the error on the power changes with track length. As expected the power is less accurate for shorter tracks.

The track slope measurement is the next criteria which needs to be validated. The error in the slope measurement is histogrammed in Fig. 4.9. The error can be empirically fitted with a Lorentzian distribution centered at zero with $\gamma \sim 0.04\ \frac{MHz}{ms}$. The track length is once more the most relevant factor in the efficiency of the slope measurement as it is apparent from Fig. 4.10.

4.2 Spectrum Analysis

In the last section, we studied the track and event reconstruction algorithms and discussed how the tracks are constructed and grouped together in a single electron event. The next task in the analysis chain is to relate the measured features of an event to the electron's

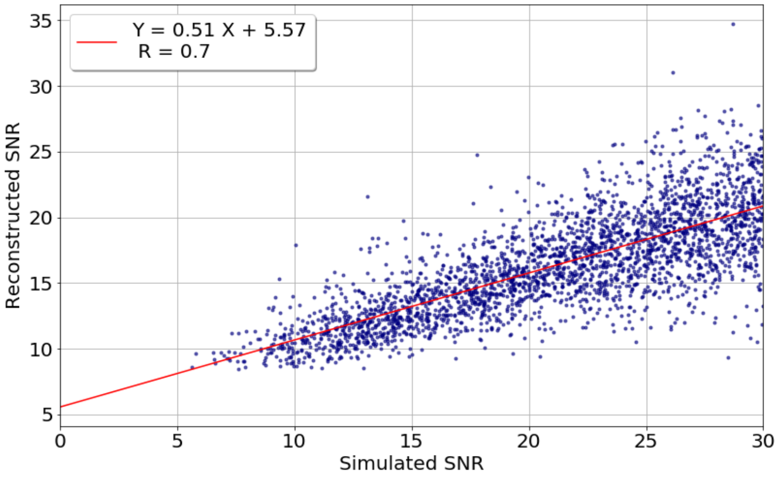

Figure 4.7: Reconstructed SNR vs. simulated SNR. The red line represent the fit to the points with reconstructed SNR above 12.5.

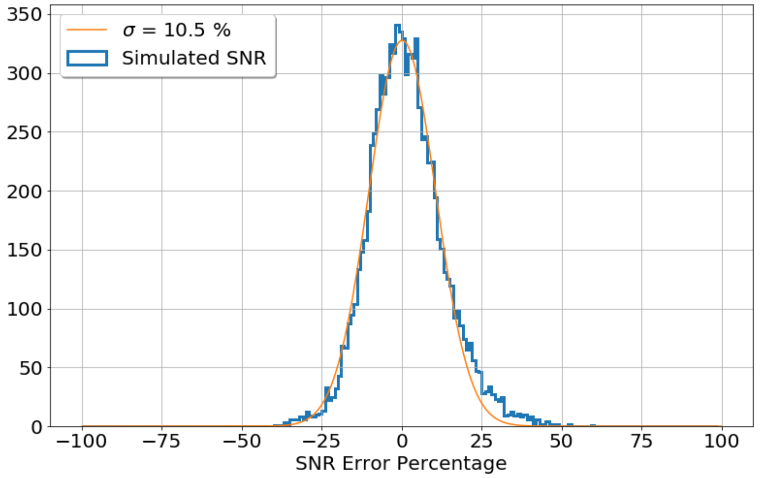

Figure 4.8: Power error percentage (defined as the percentage difference between the reconstructed and the red line in Fig. 4.7) histogram.

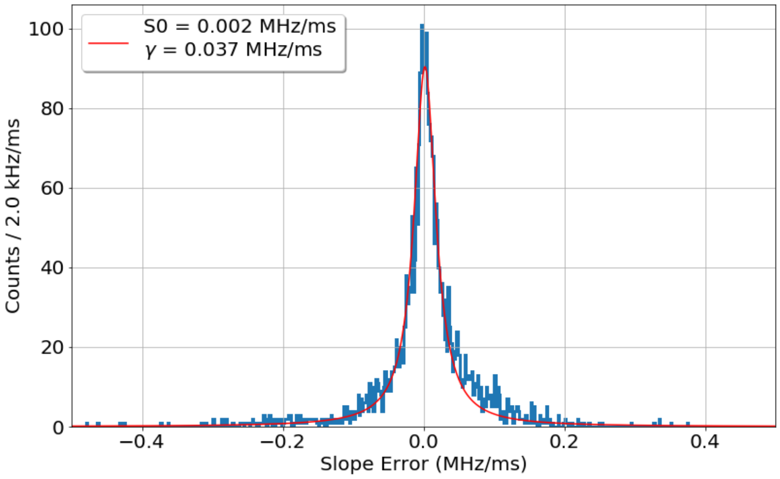

Figure 4.9: Slope error (defined as the difference between the reconstructed and simulated slope) histogram. The slope error follows a Cauchy distribution with $\gamma = 0.037\ \frac{MHz}{ms}$.

kinematics including its energy.

Project 8 demonstrator's main purpose is to measure a precise tritium spectrum from which a tritium end-point can be evaluated. The ideal analysis chain in order to reach this purpose can be characterized by a number of criteria. First, the main objective of the analysis chain should be to facilitate the highest number of electron events available. The event statistics has a significant effect on the precision of the tritium end-point measurement. Second, energy resolution is the other feature which determines the precision of a tritium end-point measurement. Third, we need to ensure that the simple cyclotron equation (Eq. 1.12) is the right relation for relating the energy and frequency of the electron. This feature, which we named linearity, can be tested via changing electron's energy or the strength of the background magnetic field. Lastly, the receiver chain's detection efficiency should be well understood in the frequency range of interest. Failure in recognizing the detection efficiency would result in a distorted tritium spectrum measurement.

In order to investigate the performance of the system and calibrate our analysis procedure, we employ conversion electrons from ^{83m}Kr. As it was mentioned in chapter 2, a source of ^{83}Rb is used to produce ^{83m}Kr continuously. The krypton then decays through two sequential

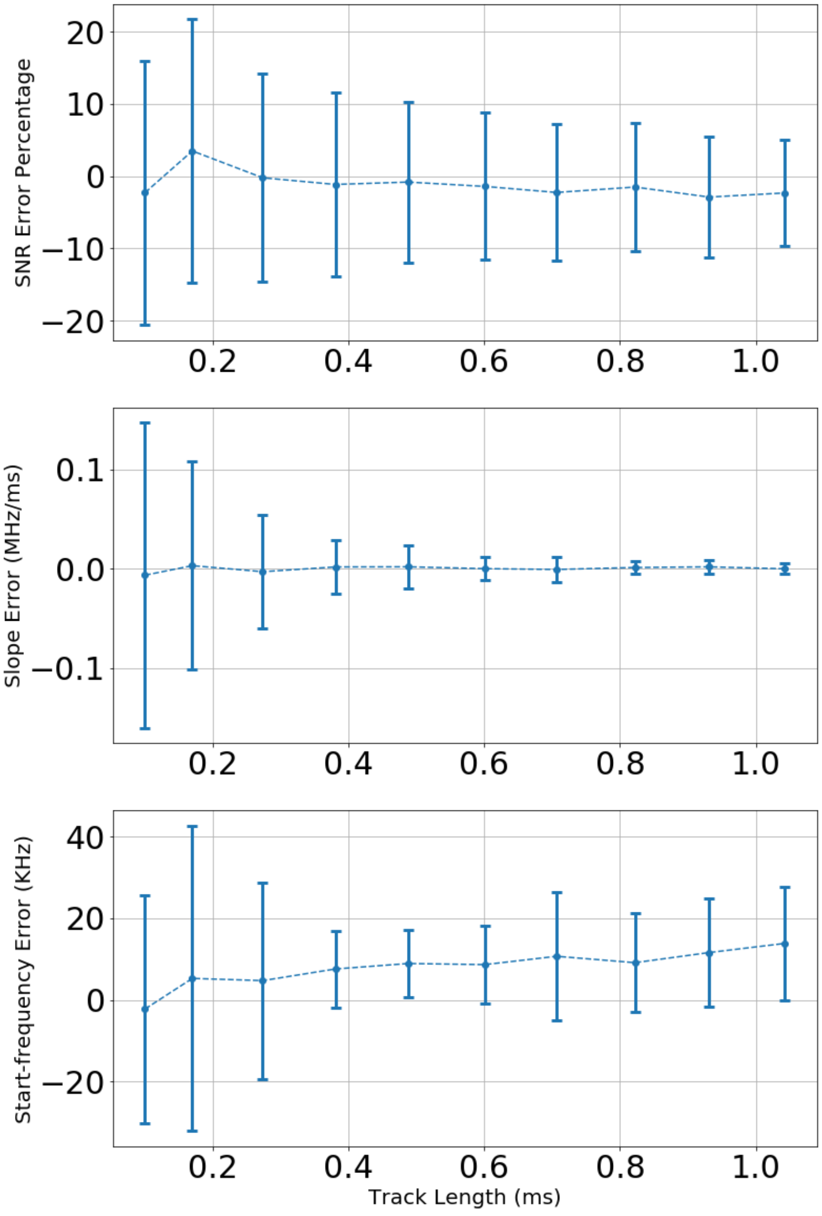

Figure 4.10: Errors in the power, slope, and start-frequency as a function of track length.

transitions of 32 keV and 9.4 keV. The energy of these transition are internally converted to release electrons from the krypton's shell. The energy of these electrons depend on the shell to which they belonged initially. Tbl. 4.1 summarizes the experimental measurements using the Mainz spectrometer.

Line	Intensity per Decay (%)	Binding Energy (eV)	Natural LineWidth (eV)	Recoil Energy (eV)	Conversion Electron Energy (eV)
K	24.8(5)	14327.26(4)	2.71(20)	0.120	17824.2(5)
L_2	24.3(3)	1731.91(6)	1.25(25)	0.207	30419.5(5)
L_3	37.8(5)	1679.21(5)	1.19(24)	0.207	30472.2(5)
M_2	4.02(6)	222.12(17)	1.6(2)	0.218	31929.3(5)
M_3	6.24(9)	214.54(11)	1.1(1)	0.218	31936.9(5)
N_2	0.300(4)	14.67(1)	0.03	0.219	32136.7(5)
N_3	0.457(6)	14.00(1)	0.03	0.219	32137.4(5)

Table 4.1: Conversion electron lines for krypton's 32 keV transition [14].

The most attractive electrons for Project 8 are those in the K line of the krypton spectrum which have 17.83 keV of energy. This line is a compelling option for calibrating the analysis chain due to its proximity to the end-point energy of the tritium spectrum.

In this section we first present electron data recorded in a *standard candle* trapping geometry. We then use the model built in the last chapter to explain different spectral features of this CRES signal. Then we show that the best energy resolution can be achieved in a *shallow trap* geometry. This specific geometry will prove the potentials of the CRES technique in high resolution electron spectroscopy.

We then present our investigation for finding the best trapping configuration. The ideal trapping configuration should have the potential for trapping the largest number of electrons (feasible in deeper traps) while providing a satisfactory energy resolution(feasible in shallower traps). We will discuss how these two criteria are incompatible for different trapping configurations and our strategy in choosing the *Final Trap Configuration*.

We then present a novel technique in which using electron tracks' power and slope assists us to attain a better energy resolution in deeper traps. This technique is based on the knowledge that we acquired in the last chapter by building a phenomenological model to characterize the CRES signal in a waveguide.

Finally, we present the data taken utilizing the field shifting solenoid introduced in Sec. 2.4. This data assists us to study the frequency dependent systematics of our complicated receiver chain, in the frequency range in which we measure the tritium spectrum.

It is also worth mentioning that there is a possibility that the electron events manifest themselves in a non-trivial topology. These topologies happen when the electron radiate most of its energy into the secondary peaks of the spectrum. These peaks show up in the event spectrogram as parallel tracks. These topologies can further complicate the spectrum analysis chain. However these structures are absent in the phase II spectrograms. Therefore we present the discussion on sideband analysis in Appx. D. There we will show how the knowledge we built in the last chapter can assist us to understand these non-trivial spectrograms.

4.2.1 Spectral Features of the CRES Data

After a track has been reconstructed using the algorithms reviewed in Sec. 4.1, a number of physical quantities can be extracted. The track's start-frequency, power, slope, and time length are the ones that carry the most significant physical information. In this section we present the data taken with the phase II apparatus. Then we utilize the model built in the last chapter along with the study of track and event reconstruction algorithms, to describe the features apparent in the data.

The data presented here is from the K line electrons of krypton's spectrum recorded in the trap coil 3 with a 0.3 A current in the harmonic mode configuration (a.k.a. standard candle configuration).

To simulate the electron's CRES signal one needs to have the information about its energy, radial position, and pitch-angle at the bottom of the trap. Given these quantities the electron track's start-frequency, power, and slope can be calculated using the phenomenology model built in the previous chapter. The effect of reconstruction algorithm is then modeled using the result of the study presented in Sec. 4.1. This effect includes adding a track-length dependent Lorentzian error to the track slope and a track-length dependent Gaussian error to the track power.

The track-length is simulated assuming an exponential distribution with a half-life which is directly assigned from the data. The reason for this assumption will be discussed shortly. Next in the final step the track is tagged with either a "detected" or "undetected" label based on its power and track length (Fig. 4.4). It worth mentioning that the last step is far from ideal. The detectability of a track depends on a more complicated set of quantities (such as track slope) which we overlook.

To model the other measured quantities, we start with simulating the energy of the conversion electron with a Lorentzian distribution,

$$P(E) = \frac{1}{\pi}\frac{\gamma/2}{\gamma^2/4 + (E - E_0)^2} \tag{4.6}$$

with $E_0 = 17824\ eV$ and $\gamma = 2.7\ eV$ (Tbl. 4.1). The electron's radial position follows a linear distribution

$$P(\rho) = \frac{2\rho}{a^2}, \tag{4.7}$$

where a is the radius of the waveguide. Finally, the electron pitch-angle as it gets emitted by the krypton atom follows a sinusoidal distribution,

$$P(\theta_0) = \sin\theta_0. \tag{4.8}$$

However to use the equations driven in the last chapter we need to find the value of electron's pitch-angle at the bottom of the trap. Eq. (3.10) can be used to extract this information.

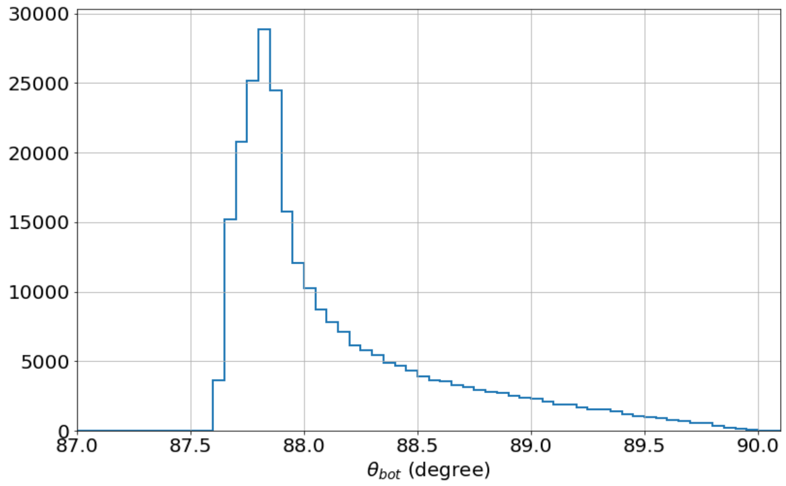

Figure 4.11: The trapped electron's pitch-angle at the bottom of the trap.

The local value of the magnetic field and the minimum value of the field traversed by the electron is needed for this calculation. The axial position of the electron, which follows a uniform distribution, and its radial positions can be used to estimate the local value of the magnetic field based on the calculated values for the phase II trap coil geometry (Fig. 2.13). Furthermore, since the electron's axial motion does not change its radial position[1], neither does its slow grad-B motion, the minimum of the magnetic field is the minimum of the trap field at the given radial position. Fig. 4.11 shows the electron pitch-angle value at the bottom of the trap for the electrons that can be trapped using the phase II standard candle trap geometry. Given this information the track's associated quantities can be calculated.

Track length yields the information about the gas pressure and the electron's cross section with the residual gas inside the gas cell. Fig. 4.12 shows the track length histograms. Two distinct features can be noticed in this plot. At large track length ($t > 0.5\ ms$), the counts follow a pure exponential distribution. This distribution is the result of the electron scattering off the residual gas. The mean free time of electron can be extracted from this region of the histogram. Afterward the mean free path can be extracted and it can be related to the

---

[1] This is true in the cases that we can ignore the radial component of the magnetic field. This holds when the background field is much stronger than the trap field.

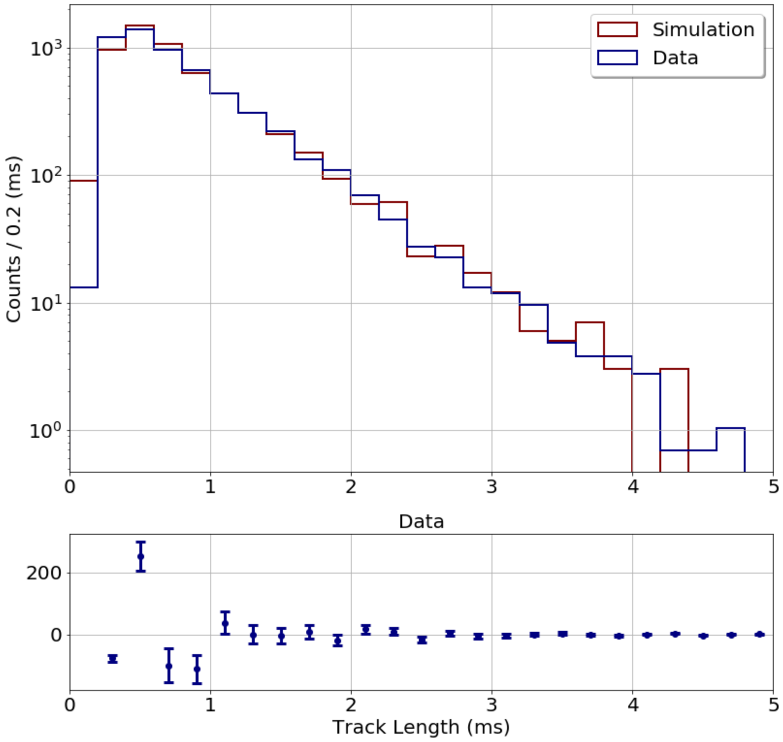

Figure 4.12: Track length histogram of the simulated and measured data taken in standard candle trapping geometry. The track length follows an exponential distribution at larger values. The missing low track lengths are due to inefficiency of track and event reconstruction in detecting the short tracks.

pressure inside the gas cell,

$$\lambda = \frac{1}{n\sigma} = \frac{k_B T}{P\sigma}, \tag{4.9}$$

where σ is the electron-ion cross section. The next feature in the track-length histogram is the inability of the track reconstruction algorithms to detect short tracks. Fig. 4.4 illustrates this inefficiency in reconstructing these short tracks.

The next important feature is the track power in the spectrogram. The model in the last section is used here to calculate the track power based on electron's radial position,

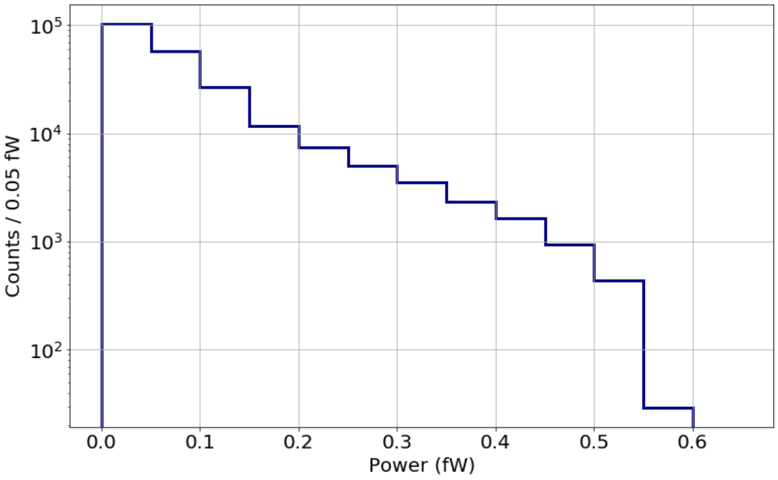

Figure 4.13: Calculated electron's power distribution in a standard candle geometry.

pitch-angle, and energy. Fig. 4.13 shows the electron emitted power[2] distribution. The track power empirically follows an exponential distribution.

In the next step the power distribution of detectable tracks is evaluated. Fig. 4.14 shows the averaged normalized unit power for the electron tracks. As can be seen, the power follows a gamma distribution,

$$P(p) = \frac{\beta^{\alpha}}{\Gamma(\alpha)}(p - p_0)^{\alpha-1}e^{-\beta(p-p_0)}. \tag{4.10}$$

The polynomial term in the gamma distribution models the track and event reconstruction inefficiencies to reconstruct low power tracks. The exponential term fits the probability of the events to have higher power values. The simulated data has fairly modeled the power distribution. The differences are most probably due to the non-ideal detectability model.

The track slope can also be calculated using the electron's radial position and its energy. As it was shown in the last chapter the total radiated power of an electron is approximately

---

[2] The power is the radiation by the electron in one direction. The total radiated power by the electron are twice the values shown in Fig. 4.13

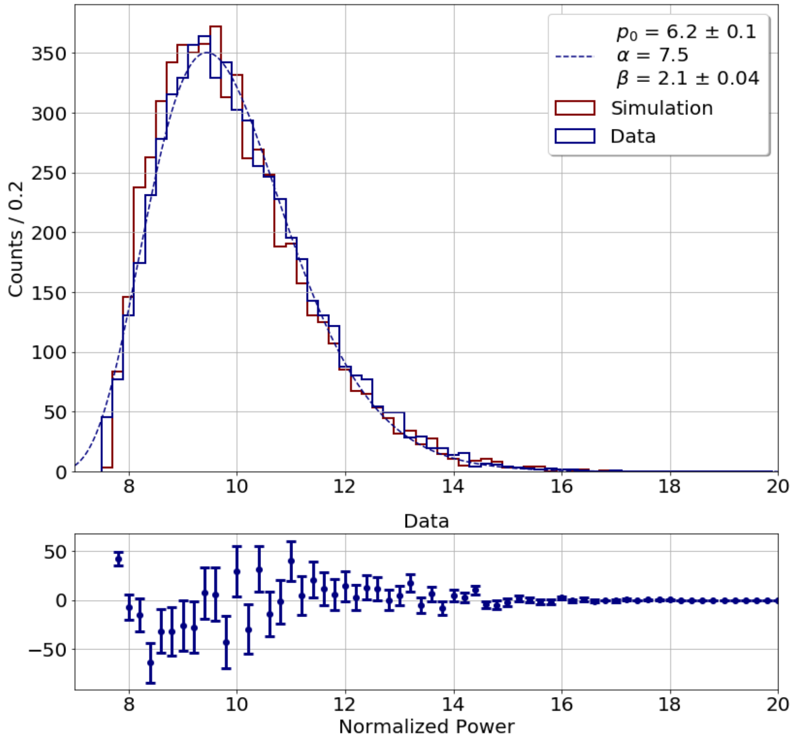

Figure 4.14: Normalized power histogram of the simulated and measured data taken in standard candle trapping geometry. The data follows a gamma distribution given in Eq. (4.10).

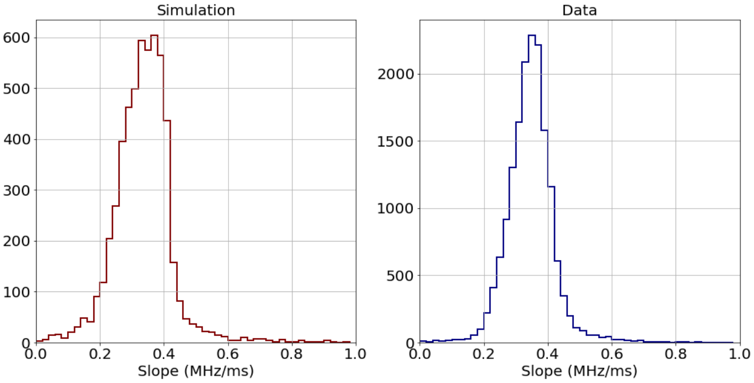

Figure 4.15: First track's slope histogram of the simulated and measured data taken in standard candle trapping geometry. A 0.07 MHz/ms offset is added to simulated data as the non-propagating mode's contribution to slope.

independent of its pitch-angle value. Hence, Eq. (4.2) can be used to find the track slope,

$$S = \frac{f_0}{m_e c^2 + E} \left(2 \times P_{0,TE_{11}} + P_{non}\right), \tag{4.11}$$

where P_{non} is the non-propagating power radiated by the electron. The factor of 2 is added to include radiation in both directions. Fig. 4.15 shows the result of this simulation and the measured data. The discrepancy between the simulation and measurement is due to presence of resonant structures in the slope. We will discuss these effects in more details in the next section. Here we assume a constant value for radiation into the non-propagating mode

$$S_{non} \ \equiv \ \frac{f_0}{m_e c^2 + E} \ P_{non} \ = \ 0.07 \ \frac{MHz}{ms}. \tag{4.12}$$

Finally, the track start-frequency which is the quantity used directly in the energy measurement can be calculated. The track start-frequency is equal to the averaged cyclotron frequency of the electron over a full axial period. The averaged cyclotron frequency can be deduced by using the information of the electron's radial position and its pitch-angle at the bottom of the trap. Fig. 4.16 represent the data and compares it to the simulation. The simulated data is fitted with a Voigt distribution with a fixed Lorentzian width given in Tbl. 4.1. The broadening of the line due to the field variation experienced by the electron can be properly modeled with a Gaussian distribution.

One obvious feature which is absent in the simulation is the tail of the frequency histogram. The tail is the result of the combination of the shake-off and shake-up electrons and the scattering events. The shake-up electrons are the ones which have excited another electron in the krypton atom orbitals. Therefore they have lost some energy and have a higher cyclotron frequency. The shake-off electrons are similar to the shake-up electrons with the only difference that they completely liberated another electron from the krypton shell.

However most events in the tail are caused by electron events for which the first tracks cannot be detected. A glance at Fig. 4.11 proves that most of the electrons have a small pitch-angle ($\sim$ 87 *degree*) in the trap. The radiated power of these electrons is not sufficient to be detectable. However, a single or multiple scatterings can change the electron pitch-angle and increase its radiated power so it can be detected. At that time the electron has lost some of its energy and therefore its cyclotron frequency has increased.

For modeling the line-shape we consider scattering off the krypton and hydrogen molecules inside the gas cell. The line-shape function is

$$L = \sum_{n=0}^{N} \sum_{i=0}^{n} \binom{n}{i} a\rho(1-\rho)^n \sigma^n \gamma_H^i \gamma_{Kr}^{n-i} f_{(i,n-i)}. \tag{4.13}$$

Here a is an amplitude and ρ is the probability of detection for any given track. N is the total number of scattering and i is the number of Hydrogen scatterings. σ is the total cross section and γ_H and γ_{Kr} are the relative contributions of the hydrogen and krypton molecules in the scattering process. Finally, $f_{(i,n-i)}$ is the electron spectrum after i hydrogen and $n-i$ krypton scatterings[3].

---

[3] This model is developed by Yu-Hao Sun (yxs682@case.edu), Nick Buzinsky(buzinsky@mit.edu), and Eris Machado (emachado@uw.edu).

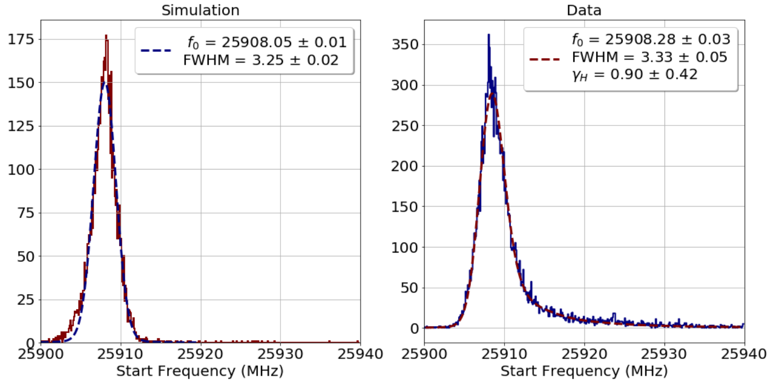

Figure 4.16: Start-frequency histogram of the simulated and measured data taken in the standard candle trapping geometry. The simulation data lacks the frequency tail of the measurement caused by the scattered events in the trap. A Voigt distribution with a fixed Lorentzian width is used to fit the simulated data. The line-shape in Eq. 4.13 is used to fit the measured histogram.

The spectrum before any scattering, $f_{(0,0)}$, is a Lorentzian function with the addition of the shake-off and shake-up spectrum [54]. The electron energy loss in an electron-hydrogen scattering, $f_{(1,0)}$, is modeled using the measurement presented in [8]. The electron spectrum after scattering off the krypton, $f_{(0,1)}$, is from [49]. The higher order scattering functions are evaluated by convolving these two functions. At the final step this line-shape is convolved with a Gaussian function to model the energy resolution of the detector. Fig. 4.16 shows the result of this fit.

4.2.2 High Resolution Spectroscopy with the Shallow Trap Geometry

In the last section we showed how the change in the value of magnetic field in a trap causes a broadening in the electrons' frequency histogram. A more precise energy measurement is hence achievable by employing a shallow trap geometry in which the trapping coil currents are set to a minimum possible value. This geometry then causes small radial and axial changes in the magnetic field of the trap. In the specific geometry used in this section, trapping coil 3's current is set to 12 mA and trapping coil 4 has a 17.85 mA current (Fig.

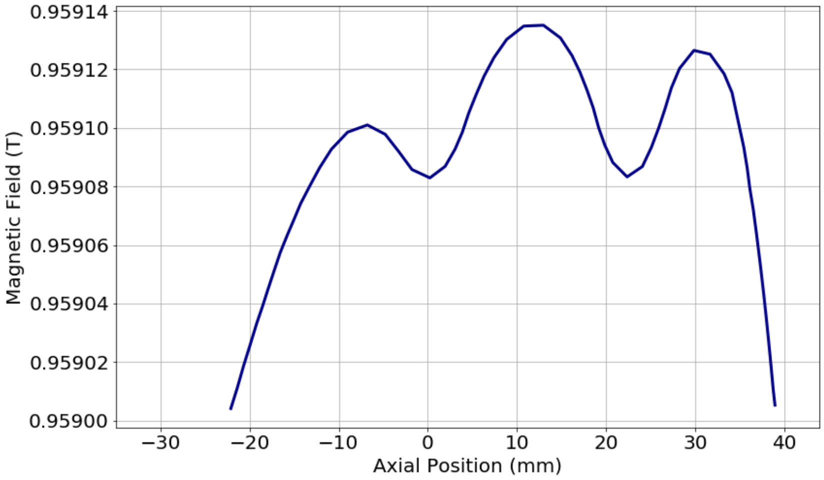

Figure 4.17: The shallow trap geometry used in this section. Trap coils 3 and 4 are used with their currents at 12 mA and 17.85 mA.

4.17[4]).

Fig. 4.18, 4.19, 4.20, and 4.21 show the frequency histograms of conversion electrons respectively from K, L, M, and N lines of ^{83m}Kr recorded in the shallow trap. These plots are recorded simultaneously using three distinct channels of the ROACH data acquisition system. The fits to K, L, and M lines are performed using a Voigt function with a Gaussian and Lorentzian fixed width σ and γ. For fitting the N_{2+3} line a double Gaussian fit with fixed separation and relative intensities is used. The fit is performed solely on the main peak and the tail events are ignored in the fit.

The central frequencies found in the above fits can be used to check the linearity of the system over 600 MHz of frequency band. This measurement can also be used to infer the energy of the krypton's 32 keV gamma ray.

The measured frequencies follow the known cyclotron frequency relation,

$$f_i = \frac{eB}{2\pi} \frac{1}{m_e + \left(\frac{E_\gamma - U_i - E_i(rec)}{c^2}\right)}, \tag{4.14}$$

where E_γ, U_i, and E_{r_i} are respectively the krypton's 32 keV gamma energy, the binding

---

[4] The plot is by Hamish Robertson (rghr@uw.edu).

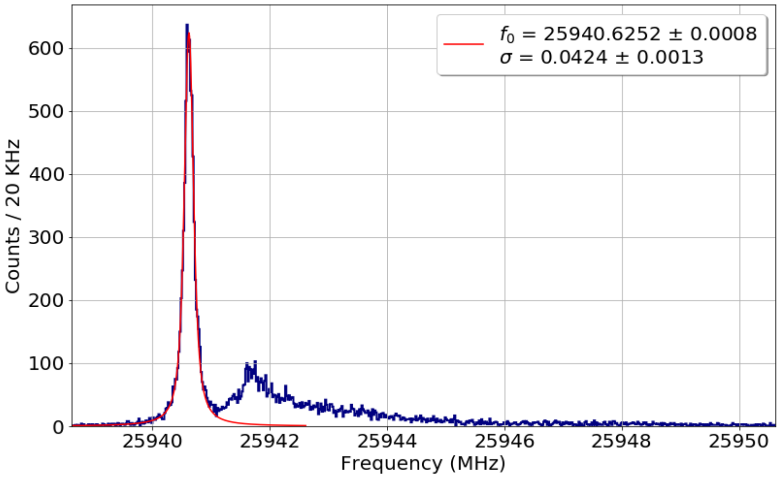

Figure 4.18: The frequency histogram of electrons from the K line of Krypton spectrum recorded in the shallow trap geometry. The peak is fitted using a Voigt distribution with a fixed Lorentzian width. The value for the central frequency and the Gaussian width of the Voigt function are given in the legend box.

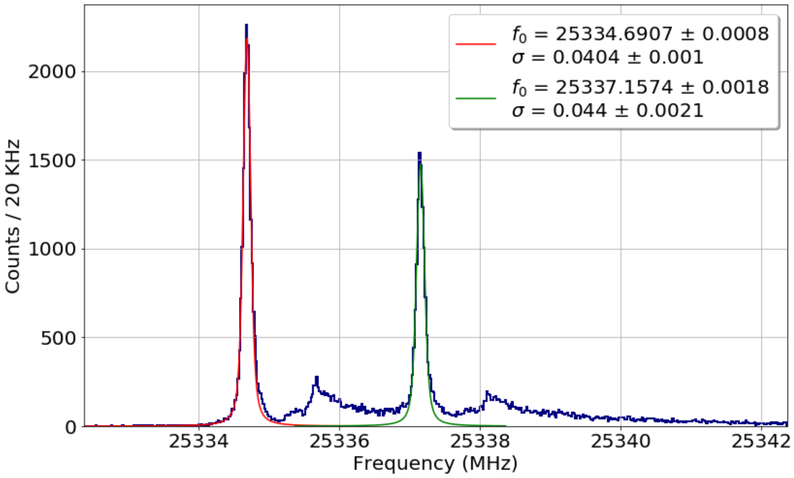

Figure 4.19: The frequency histogram of electrons from the L2 and L3 lines of Krypton spectrum recorded in the shallow trap geometry. The peaks are fitted using Voigt distributions with fixed Lorentzian widths. The value for the central frequencies and the Gaussian widths of the Voigt functions are given in the legend box.

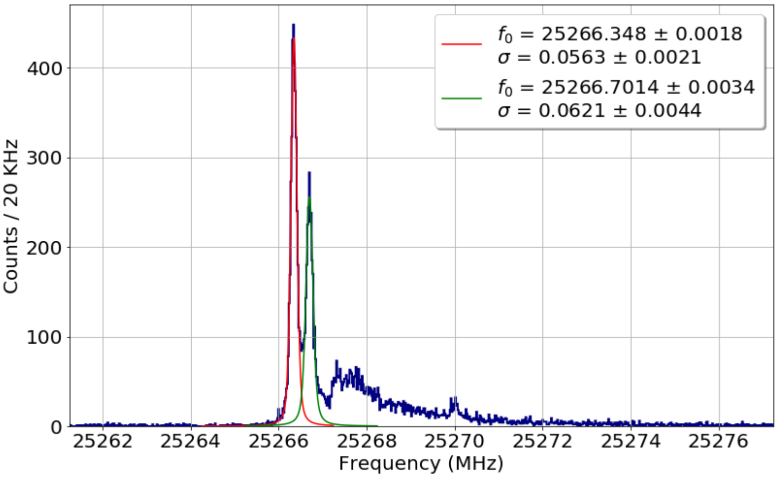

Figure 4.20: The frequency histogram of electrons from the M2 and M3 lines of Krypton spectrum recorded in the shallow trap geometry. The peaks are fitted using Voigt distributions with fixed Lorentzian widths. The value for the central frequencies and the Gaussian widths of the Voigt functions are given in the legend box.

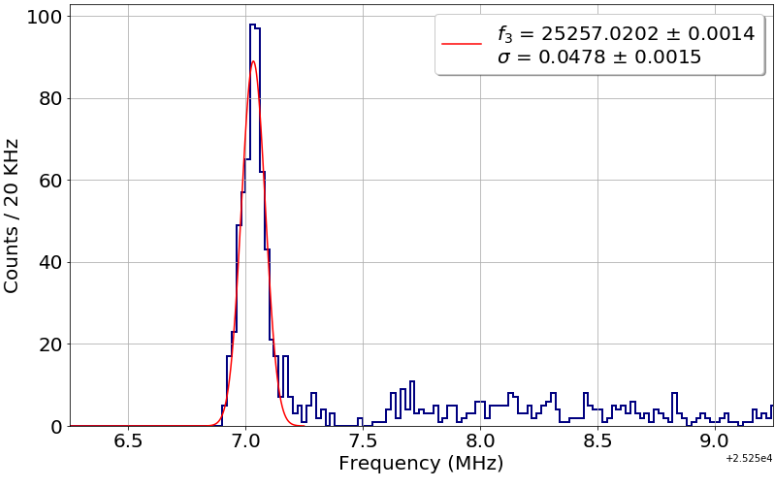

Figure 4.21: The frequency histogram of electrons from the N_{2+3} lines of Krypton spectrum recorded in the shallow trap geometry. The peak is fitted using a Gaussian distribution due to negligible natural linewidth. The value for the central frequency and the Gaussian width are given in the legend box.

energy of the i^{th} line, and the recoil energy for the i^{th} line. The values for the binding energy of the lines and their corresponding recoil energy are from Tbl. 4.1.

Using the recipe presented in Appx. E one can build a chi-square to include the errors in the binding energy,

$$\chi^2 = \sum \frac{\left(f_i - \frac{e}{2\pi m}\frac{B}{\left(1+\frac{1}{mc^2}(E_\gamma - U_i - E_i(rec))\right)^2}\right)^2}{\sigma_{f_i}^2 + \sigma_{U_i}^2 \left(\frac{e}{2\pi m}\right)^2 \frac{B^2/m^2c^4}{\left(1+\frac{1}{mc^2}(E_\gamma - U_i - E_i(rec))\right)^4}}. \tag{4.15}$$

The magnetic field and the 32 keV gamma energy are the two free parameters that can be found by minimizing the chi-square. Fig. 4.22 shows the result of this minimization with the values of magnetic field and the 32 keV gamma energy reported in the legend box.

The best estimate of the 32 keV gamma energy is from [14],

$$E_\gamma = 32151.7 \pm 0.5 \text{ eV} \qquad \text{(D.Venos et. al.)}. \tag{4.16}$$

This value is in agreement with our estimation,

$$E_\gamma = 32153.6 \pm 2.4 \text{ eV} \qquad \text{(this work)}. \tag{4.17}$$

4.2.3 Trap Configuration

The gas cell design for the second phase of Project 8 experiment is facilitated with five trapping coils (Fig. 2.11). These trapping coils can generate both the “Harmonic” and “Bathtub” trapping geometries. Finding the optimal geometry requires some investigation into the spectral features of the electrons in each configuration. Electron count rate and energy resolution are the most important aspect of an ideal trapping geometry.

A brief study of different bathtub geometries fails to meet any of the desired criteria. Therefore this geometry is not studied in more comprehensive investigations. Trap coil 5 also fails to trap any electron at any currents lower than $500mA$. The reason can be understood by reviewing the background magnetic field shown Fig. 2.2. Trap coil 5 resides in upper regions of the magnet bore where there is a steep fall in the value of background

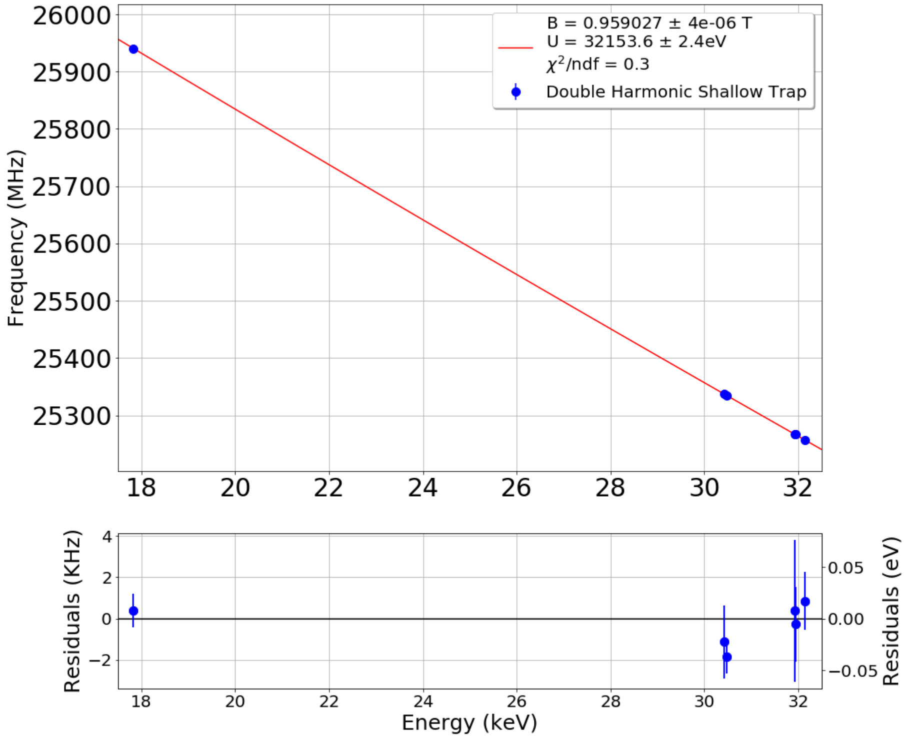

Figure 4.22: The measured frequencies vs. the known energy values of the krypton spectrum's main lines. The red line is a fit using the cyclotron frequency relation with floating magnetic field and gamma energy values.

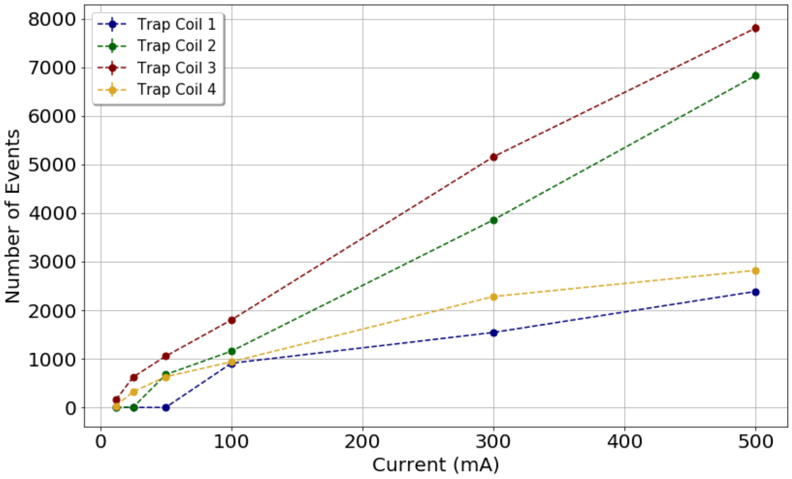

Figure 4.23: Electron count rate in trapping coils 1-4 each powered with different trapping currents. An hour of data is recorded for each point.

field. Therefore generating a valley in the magnetic field is not possible with the conventional current values used in trapping coils.

Thus, the trap config search is narrowed to using the first four trapping coils. We used currents of less than 500 mA to avoid overheating the gas cell and trapping coils. Six hours of data is recorded for each trap in six different trap depth of 12.5 mA, 25 mA, 50 mA, 100 mA, 300 mA, and 500 mA. The count rate for different trap coils at different depths is shown in Fig. 4.23. The count rate increases with trap depth for all of the trapping coils. This is due to the deeper trapping coils capability for confining larger ranges of electron pitch-angles (see Eq. (3.11)). The count rates for different trapping coils also depend on their position inside the background field.

A satisfactory energy resolution is the next crucial feature of the desired trapping configuration. Fig. 4.24 illustrates how the spectrum's width increases for all of the trapping coils with the value of the trapping coil's current. Since the magnetic field inside a deeper magnetic trap varies more broadly, electrons with different kinematics observe a more extensive range of the field values. Therefore the electron's start-frequency spectrum has a larger

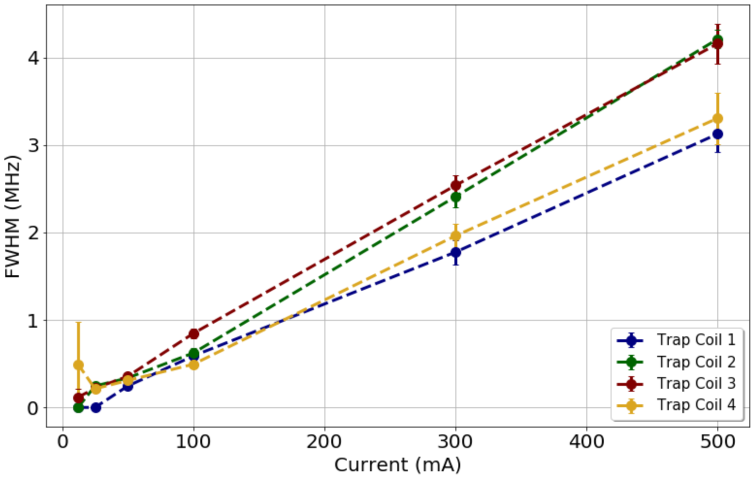

Figure 4.24: Spectrum's energy resolution for trap coils 1-4 each powered with different trapping currents. An hour of data was recorded for each point.

width [5].

A comparison between Fig. 4.23 and Fig. 4.24 suggests that the choice of trapping configuration is a trade-off between count rate and energy resolution. One means to increase the count rate without further compromising the energy resolution is to utilize all the trapping coils together. This can be achieved by carefully tuning the trapping currents so that the electrons in different magnetic traps observe similar field profiles. Since the start-frequency is linearly dependent on the value of the magnetic field which is linearly proportional to the trapping current, the start-frequency is expected to change linearly with the value of the trapping coil's current. Fig. 4.25 exhibits this linear relation between the spectrum's mean frequency and the value of trapping coil's current. The linear fits can be used to align the start-frequency spectra for electrons in different trapping coils. Note that the negative slope is due to anti-alignment of harmonic trap fields with the background magnetic field. To select the currents one needs to find the cross effect of coil currents on the magnetic field of adjacent traps. The specific geometry of the each coil is used to calculate the coil's magnetic field at the position of the other three coils. After including this cross effect the trapping

---

[5] This will be discussed in more detail in the next section.

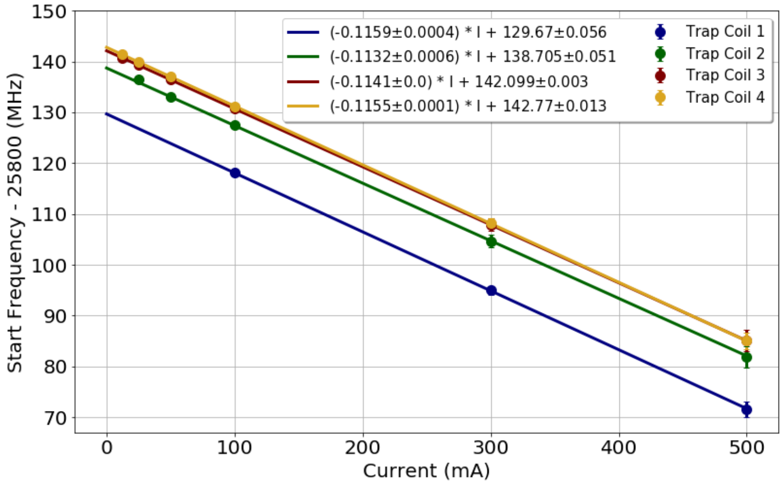

Figure 4.25: The mean values of electron's start-frequency spectrum for trap coils 1-4 powered with different trapping currents. The linear relation is evident for points with enough statistics.

coil's currents are selected to be,

$$\begin{aligned} I_1 &= 173.7644\ mA \\ I_2 &= 248.7516\ mA \\ I_3 &= 272.4751\ mA \\ I_4 &= 286.4395\ mA. \end{aligned} \tag{4.18}$$

Fig. 4.26[6] represent this trap configuration known as *Final Trap Configuration* (a.k.a. Q-300).

In the next section we propose a method in which we can use track's power and slope to increase the energy resolution without reducing the count rate.

4.2.4 Trapping Systematics

Fig. 3.3 shows how mono-energetic electrons with different pitch-angles at different radii in the trap give rise to tracks with different start frequencies. The track start-frequency is

---

[6] The plot is by Hamish Robertson (rghr@uw.edu).

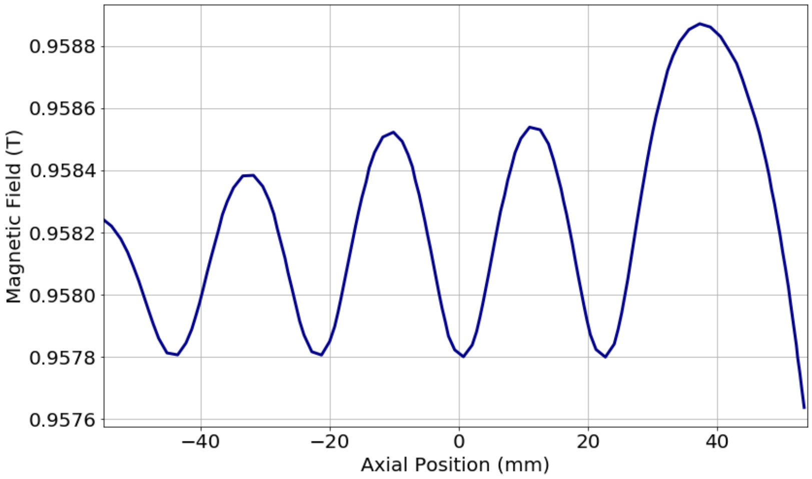

Figure 4.26: The final trap configuration. In this geometry four trapping coils are used. Their current is fine tuned to match the minimum value of the field in each trap. The shape of the background field is also included in this plot.

the averaged value of electron's cyclotron frequency over a full axial motion's period. Since electrons with lower values of pitch-angle traverse to higher field regions of the trap, their tracks have higher start-frequencies. Furthermore, electrons at larger radii inside the trap experience a lower field (see Fig. 2.13) which produces tracks with lower start-frequencies. Thus, deducing the electron energy from the track start-frequency utilizing a single magnetic field value causes a systematic effect which reduces the energy resolution in a CRES experiment. Fig. 4.18 and the right panel in Fig. 4.16 show the energy resolution of the Phase II apparatus for the shallow trap and a deep trap ($I_{trap} = 300\ mA$) . Fig. 3.3 illustrates that ignoring the effect of trapping in deducing the electron's energy leads to a systematic effect which can widen the detector's response function by tens of mega-hertz.

In order to correct for the trapping systematic effect, we need to have the knowledge of the electron's pitch-angle and radial position. This can be achieved utilizing the track power and slope.

Eq. 4.2 relates the track slope to the electron's total radiated power. We proved in Sec.

3.2 [7] that the electron's total radiated power is independent of its pitch-angle. Hence the total radiated power is equal to the mode coupling of the electron to TE_{11} mode of the waveguide defined in Eq. (3.69) and plotted in Fig. 3.6. Hence the slope is a direct measure of electron's radial position.

The track power has also radial position dependency due to the electron coupling's dependence on the radial position. The track power also depends on the value of electron's pitch-angle (Fig. 3.9). In order to construct a radial independent function, the track power can be divided by its value of slope. Hence the coupling function cancels and a radial independent quantity is constructed which only depends on the electron's pitch-angle.

Fig. 4.27 shows the values of slope and main track's power for the krypton's L line conversion electrons in a 300 mA deep trap. An obvious triangular structure can be seen in this plot. The low power edge is the manifestation of the minimum power cut below which the tracks cannot be distinguished from the noise. The points on the high slope edge of the plot belong to the electrons at the center of the trap that have the highest electron coupling to waveguide mode. The third edge consists of electron tracks for a given slope value that have the most powerful tracks. These are the electrons that have a 90 degree pitch-angle. Notice that this line has a non-zero x-intercept, S_0. This non-zero value signals the existence of electron power coupling into the non-propagating modes in the waveguide. Vertical lines in the plot relate electrons at similar radial position in the trap and the positive slope lines passing the S_0 point connect the electrons with the same pitch-angle value.

To address the trapping systematic effect one can shift the measured track's start-frequency based on its value of slope and power. In the first step, we shift the measured start-frequency using the slope as if the electron was at the center of the trap. Fig. 4.28 shows the slope vs. start-frequency for L line conversion electrons. An obvious edge can be seen at lower frequencies. This edge consists of electrons with 90 degree pitch-angle for which the start-frequency has the lowest value. The low slope points are from electrons

---

[7] Eq. (3.67)

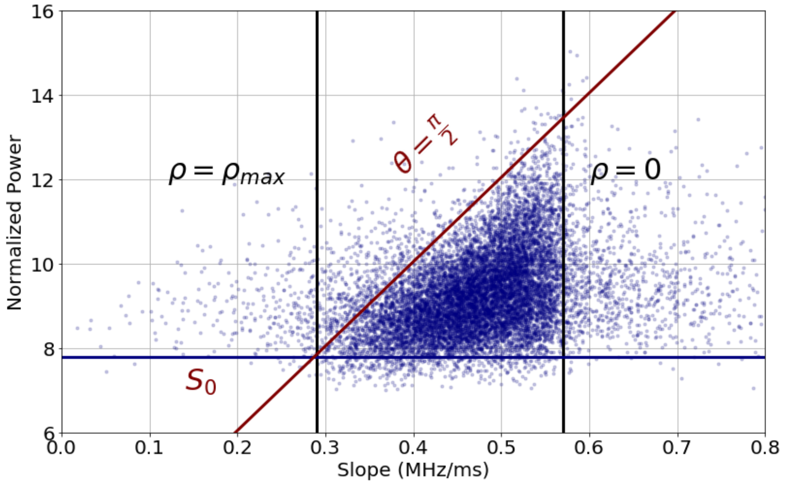

Figure 4.27: Track power vs. track slope for electrons from the L line of krypton spectrum recorded in the standard candle trap geometry. Each point represents a single event. The vertical lines connect events with similar radial position (ρ). The lines passing the S_0 (Eq. (4.12)) value on the slope axis connect events with similar pitch-angle values.

with smaller electron couplings. These are the electrons closer to the wall of the waveguide. In a harmonic trap the magnetic field has the lowest value next to the trapping coils and the wall of the waveguide. Thus these electrons generate tracks with lower start frequencies. By moving to the higher values of slope in the plot one is observing electrons closer to the center of the trap. The electron coupling increases for these electrons and therefore the generated tracks have higher slopes. Moreover, the magnetic field increases by moving toward the center of the trap which causes an increase in the track's start-frequency. The magnetic field change with the radius has a parabolic shape. Therefore the start-frequency which is linearly dependent on the magnetic field also changes parabolically with respect to the radius. Since the electron coupling to the waveguide mode plotted in Fig. 3.6 can also be well-approximated with a parabola, the edge in the Fig. 4.28 has a linear form.

In the first step to correct the measured start-frequency, a line is used to find the edge in Fig. 4.28. This line was then used to shift the measured start-frequency based on the value of the track's slope. Fig. 4.29 shows the slope vs. rho-corrected frequency for the same data

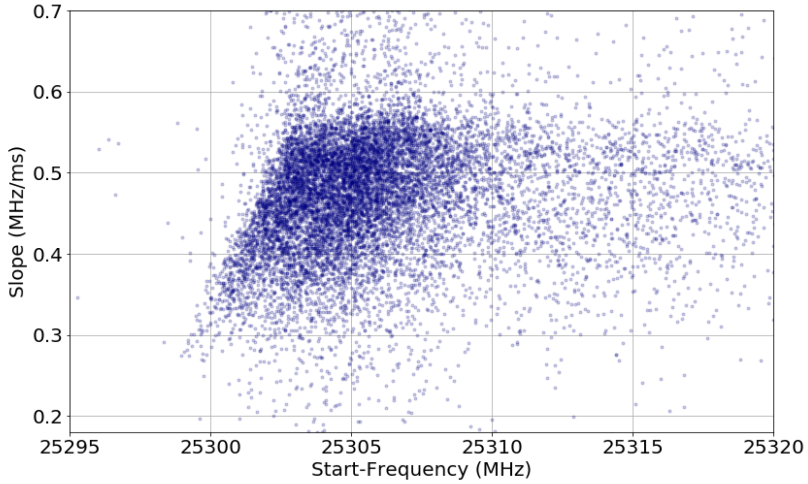

Figure 4.28: Track slope vs. track start-frequency for electrons from the L line of krypton spectrum recorded in the standard candle trap geometry. The radial structure can be recognized in this plot. The events at larger radii experience a lower magnetic field and hence a smaller start-frequency. These events also radiate less due to weaker electron's coupling to the fundamental waveguide mode. Thus these events also have a lower slope value.

previously shown in Fig. 4.28. The rho-corrected start-frequency is the frequency that the electron track would have had if it had positioned at the center of the trap.

For finding the pitch-angle corrected frequencies we construct the quantity,

$$P_{norm}(\theta) = \frac{P_0(\rho, \theta)}{S(\rho) - S_0}, \tag{4.19}$$

where S_0 is the non-propagating mode's contribution to slope (Fig. 4.27). Fig. 4.30 plots the P_{norm} value vs. rho-corrected start-frequency. The doublet structure [8] is what we expected in Fig. 4.30. Electrons with higher pitch-angle have higher values of P_{norm} and lower values of start-frequency. A parabola was used to fit the points in Fig. 4.30. The pitch-angle-corrected start-frequency is then constructed by shifting the rho-corrected start-frequency along the parabola. Fig. 4.31 shows the same data after applying the pitch-angle correction. The pitch-angle-corrected start-frequency is the frequency that the electron track would have

---

[8] A result of the doublet energy of ^{83m}Kr's L line.

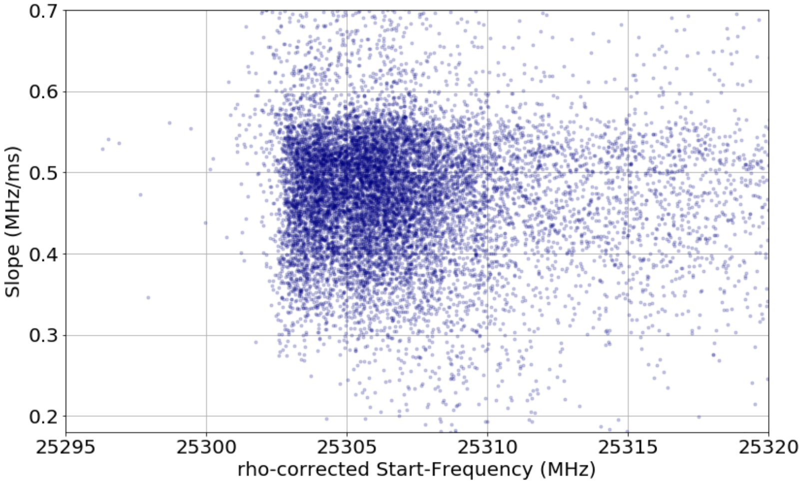

Figure 4.29: Track slope vs. track rho-corrected start-frequency for electrons from the L line of krypton spectrum recorded in the standard candle trap geometry. The rho-corrected start-frequency is the result of a shift applied to the recorded data in Fig. 4.28 to incorporate the radial variation in the magnetic field. The rho-corrected frequency is the frequency that these electrons would have radiated with if they had been placed at the center of the trap.

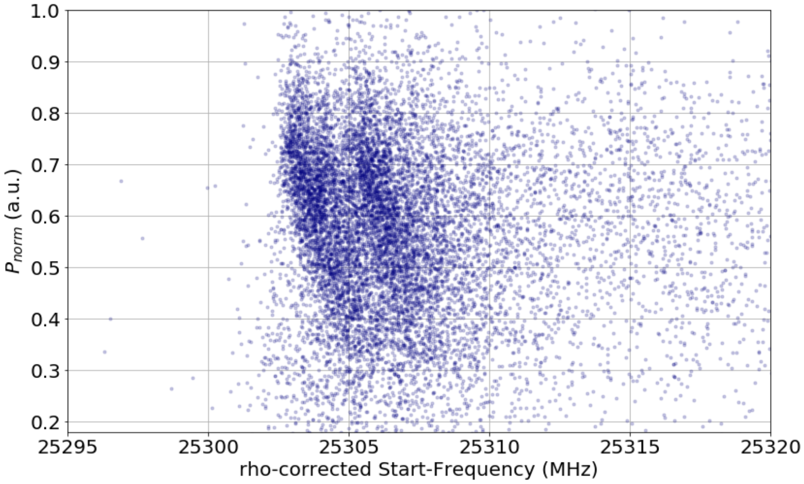

Figure 4.30: Track P_{norm} (Eq. (4.19)) vs. track rho-corrected start-frequency for electrons from the L line of krypton spectrum recorded in the standard candle trap geometry. The pitch-angle induced structure is visible in the plot. Electrons with lower value of pitch-angle experience a larger averaged magnetic field and hence have a higher start-frequency. These electrons also have a lower P_{norm} value.

had if it had been placed at the center of the trap with a 90 degree pitch-angle.

Fig. 4.32 and 4.33 show the histogram for the raw and corrected start-frequencies. The doublet structure which cannot be seen in the raw data emerges when we apply the correction.

Fig. 4.34 shows the result of applying the same correction to the K line of krypton's spectrum. Comparing the energy resolution of corrected start-frequency in Fig. 4.34 with the raw data plotted in Fig. 4.16 proves that the power-slope correction improves the line shape FWHM from 54 eV to 34 eV. However, the fine energy resolution of the shallow trap cannot be reached by using this correction scheme due to the inaccuracy in the measurements of the track power and slope [9].

---

[9] Fig. 4.9 and 4.8

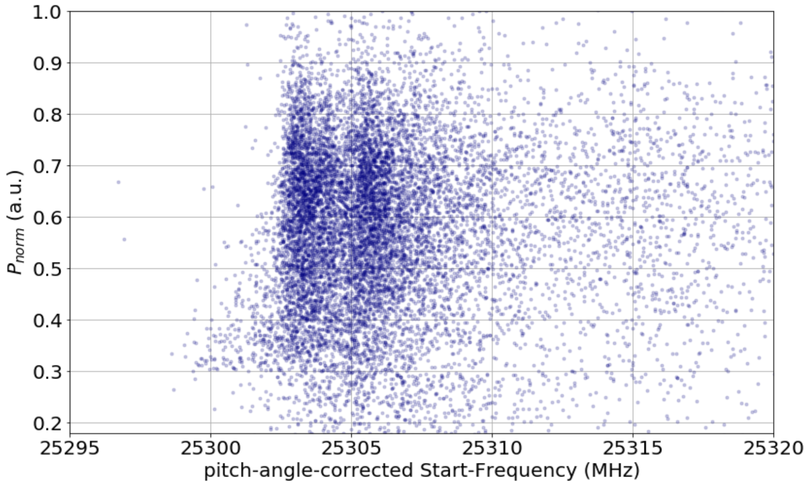

Figure 4.31: Track P_{norm} (Eq. (4.19)) vs. track pitch-angle-corrected start-frequency for electrons from the L line of krypton spectrum recorded in the standard candle trap geometry. The pitch-angle correction is the result of a shift applied to the recorded data in Fig. 4.30 to incorporate the pitch-angle variation in the value of averaged magnetic field experienced by the electron. The pitch-angle-corrected frequency is the frequency that these electrons would have radiated with if they had been emitted at the center of the trap with a 90 degree pitch-angle.

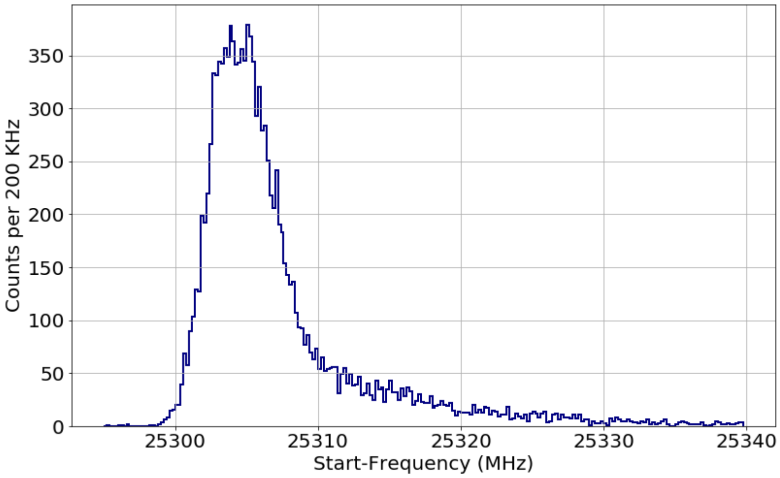

Figure 4.32: Frequency histogram of electrons from the L line of krypton spectrum recorded in the standard candle trap geometry. The doublet structure is invisible due to the radial and pitch-angle dependent broadening of the lines.

4.2.5 Field Shifting Solenoid Data Analysis

In section 2.4 we introduced the field shifting solenoid. It was mentioned that this component was added to the system as a means to study the frequency dependent systematic effects in the Phase II receiver. This goal is achieved by altering the cyclotron frequency of the conversion electrons from the K band of ^{83m}Kr. The change in the frequency is induced through a change in the background magnetic field using the solenoid. In this section we present the analysis performed using the field shifting solenoid data. This analysis helps us in finding the efficiency curve which is a crucial part of the next chapter's tritium analysis. The efficiency curve is the curve which shows how efficiently the electrons are being detected at any given frequency. It encapsulates the frequency dependent systematics in Phase II receiver.

The field shifting solenoid data is recorded with five different trap configurations. The

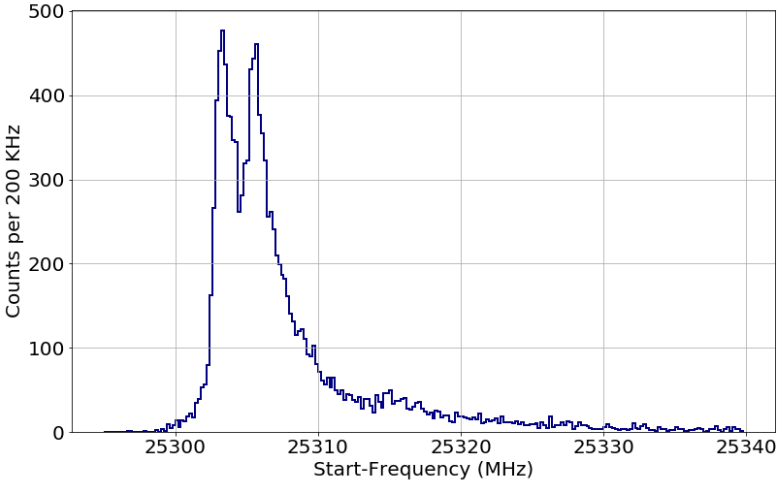

Figure 4.33: Pitch-angle-corrected frequency histogram of electrons from the L line of krypton spectrum recorded in the standard candle trap geometry. The doublet structure, with 54 eV separation, emerges after correcting the recorded frequencies for the radial and pitch-angle dependent variations of the magnetic field in the trap.

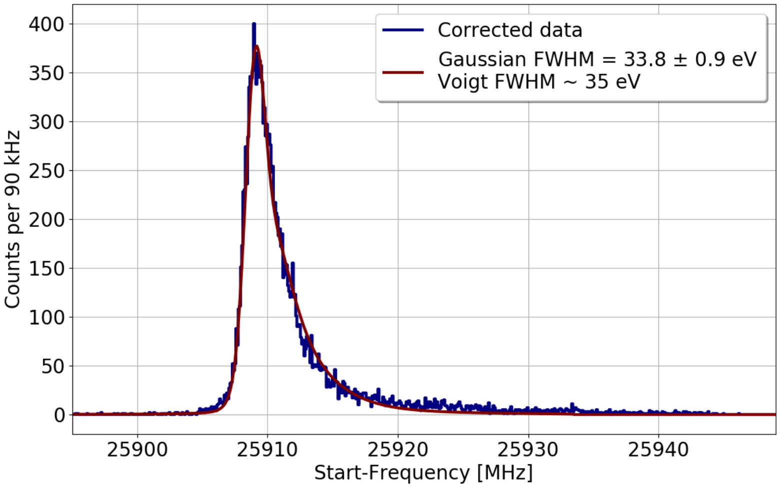

Figure 4.34: Pitch-angle-corrected frequency histogram of electrons from the K line of krypton spectrum recorded in the standard candle trap geometry. Comparing this plot with the right plot in Fig. 4.16 proves a $\sim 30\ eV$ improvement in the energy resolution.

main set uses the *Final Trap Configuration* (4.18) (a.k.a. Q-300). This trap configuration is the main configuration with which the tritium data will be studied. This data is recorded with the field shifting solenoid's current changing from $\sim -1\ A$ to $\sim\ 1A$ in 23 mA steps.

Fig. 4.35 represents the change of the krypton's K line spectrum, recorded using the Q-300 trap configuration, with field shifting solenoid's current. The frequency shown in this plot is the result of a fit to the krypton spectrum at each field shifting solenoid's current value. The frequencies are linearly dependent on the value of the current. This relationship is expected since the electron's cyclotron frequency changes linearly with the value of the magnetic filed, which has a linear relationship with the field shifting solenoid's current.

The other four trap configurations are the individual traps used in the *Final Trap Configuration* (4.18). The data recorded with these individual traps will assist us to study the efficiency curve.

Track power and slope are the two major factors shaping the efficiency curve. To that

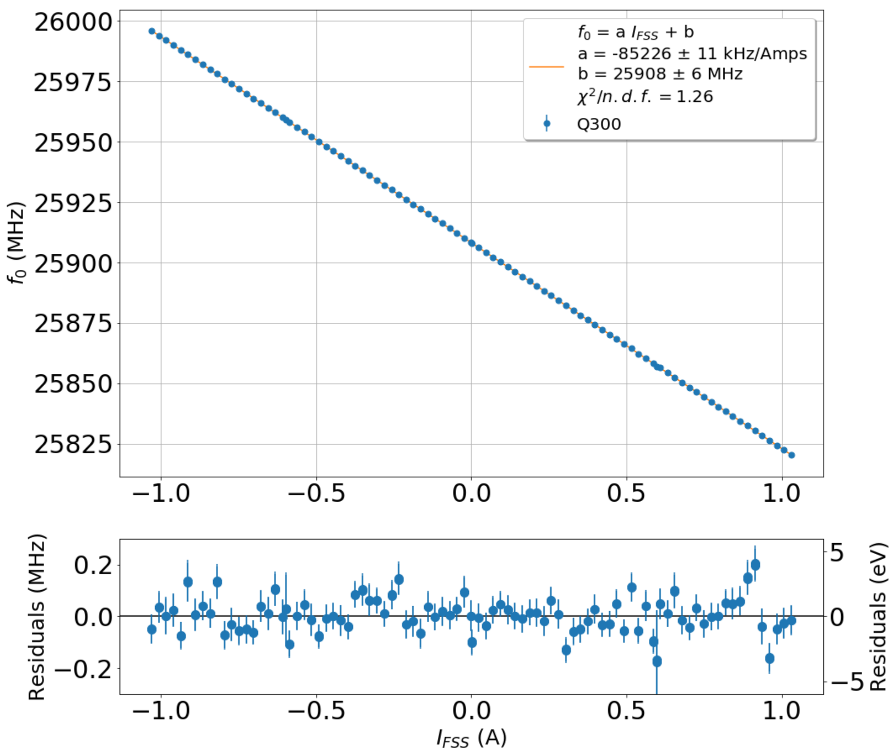

Figure 4.35: The central frequency of the krypton's K line spectrum plotted vs. the field shifting solenoid's current. The frequencies are following a linear relationship with the current values.

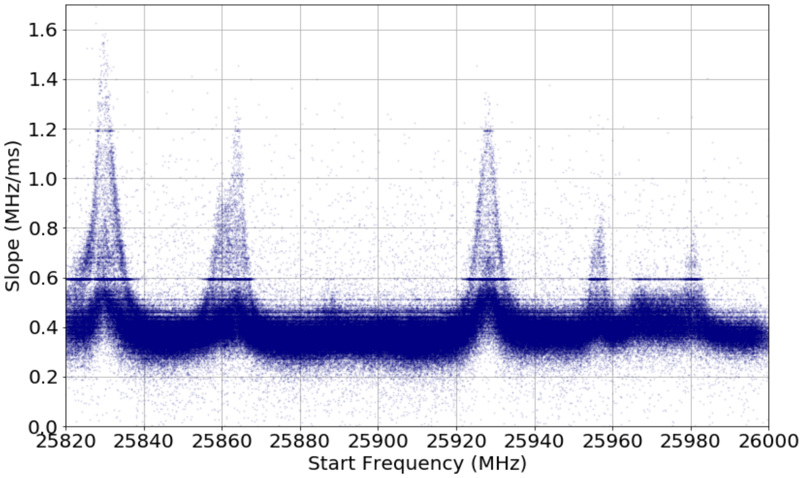

Figure 4.36: The Slope vs. start-frequency for the field shifting solenoid's data taken in the Final Trap Configuration (Eq. 4.18). Each point represents a single electron event.

end we need to investigate the track power and slope structure of the data taken with the aid of the field shifting solenoid over the frequency range of interest.

Fig. 4.36 shows the track's slope vs. start-frequency for the Q-300 field shifting solenoid's data. Each point represents a single electron event. The most apparent structure in the slope plot is a number of sharp peaks at different frequencies. The presence of these structures can be explained with the knowledge we built in the previous chapters.

It was mentioned in section 2.2 that electrons in the circular waveguide couple to the TE_{11} and TM_{01} modes of the circular waveguide. However it is the TE_{11} mode that can propagate to the amplifier stage and determine the track power. Fig. 4.37 shows the track power vs. start-frequency in the same configuration as in Fig. 4.36. It is obvious that the sharp structures in the slope plot are absent in the power plot. Hence the changes in the slope cannot be associated with the TE_{11} mode.

The TM_{01} mode on the other hand, cannot propagate in the WR-42 waveguide . Therefore it reflects back and forms resonant structures in the gas cell. These resonant structures alter the electron coupling's to TM_{01} mode and therefore change the track's slope. A more cautious inspection of the large peaks in Fig. 4.36 reveals a multi-branch structure in the

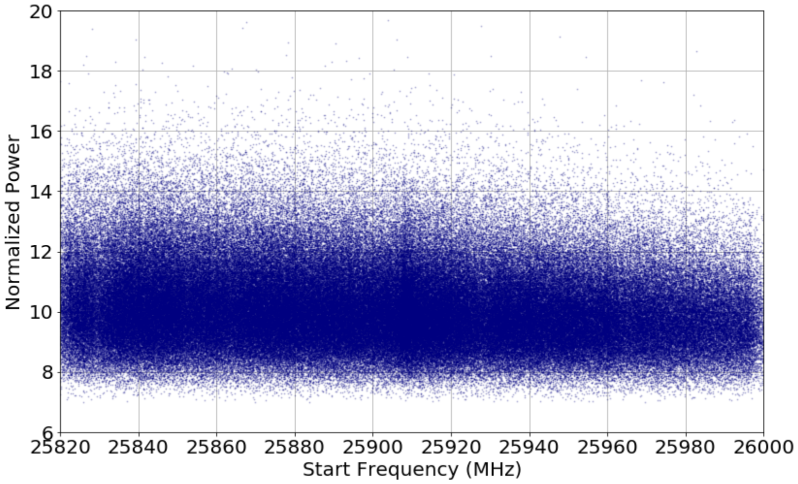

Figure 4.37: The normalized power vs. start-frequency for the field shifting solenoid's data taken in the Final Trap Configuration. Each point represents a single electron event.

slope. Comparing the plot in Fig. 4.36 with the single trap plot in Fig. 4.38 proves that the branches are formed by electrons in different traps. This effect can be explained by considering the axial dependency of electron's coupling to the resonant structure of TM_{01} mode in different traps.

Although the power does not exhibit the sharp structures that are present in the slope distribution in Fig. 4.36, a gradual change in the high value envelope of the track power distribution is observable in Fig. 4.37 [10]. To quantify this change, the frequency range is divided into 2 MHz wide bins. Next, track power at each frequency bin are fitted with the gamma function as it was explained before.

Fig. 4.39 shows how the average value of the fitted gamma function changes with frequency. In order to explain this pattern one needs to investigate the track power change of each of the four traps individually.

Fig. 4.40 illustrates how the averaged track power varies with frequency for the four single trap data. To model the power variation in the single traps we need to consider the places at

---

[10] The lower limit on the power is rooted in the track reconstruction algorithms. Therefore a frequency dependent change is not expected with regard to this lower cut.

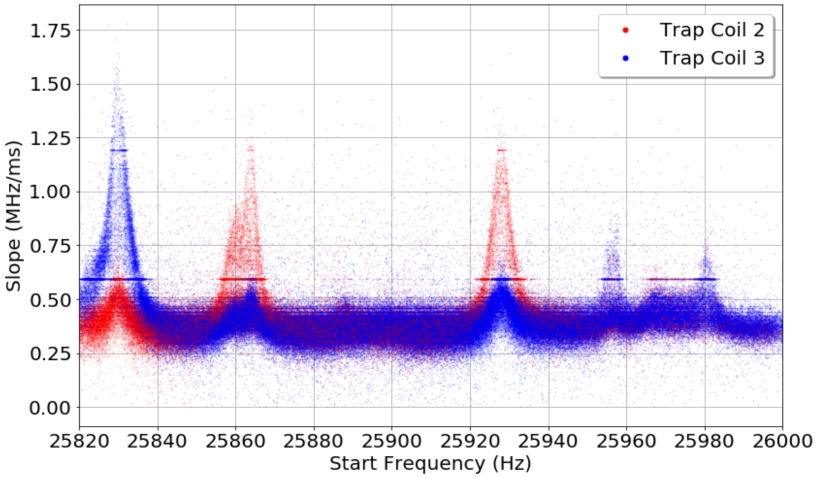

Figure 4.38: The Slope vs. start-frequency for the field shifting solenoid's data taken in the single coil traps 2 and 3. Each point represents a single electron event.

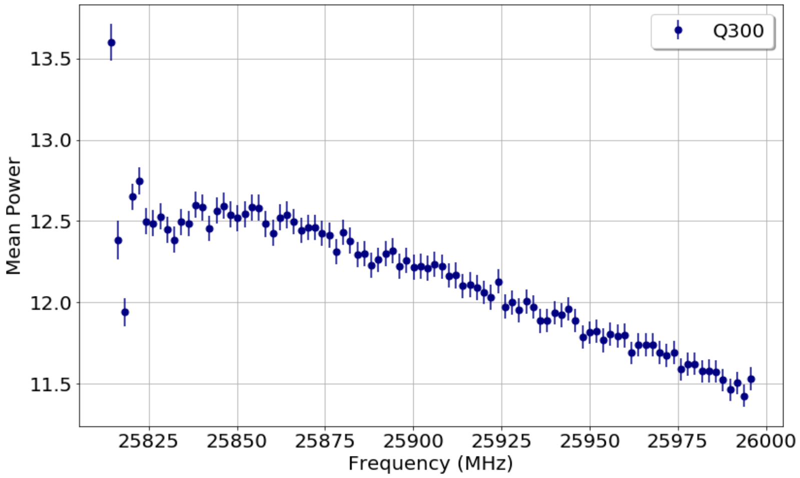

Figure 4.39: The averaged power from the fitted gamma distribution to the tracks' normalized power as a function of the frequency. The data is taken in the final trap configuration.

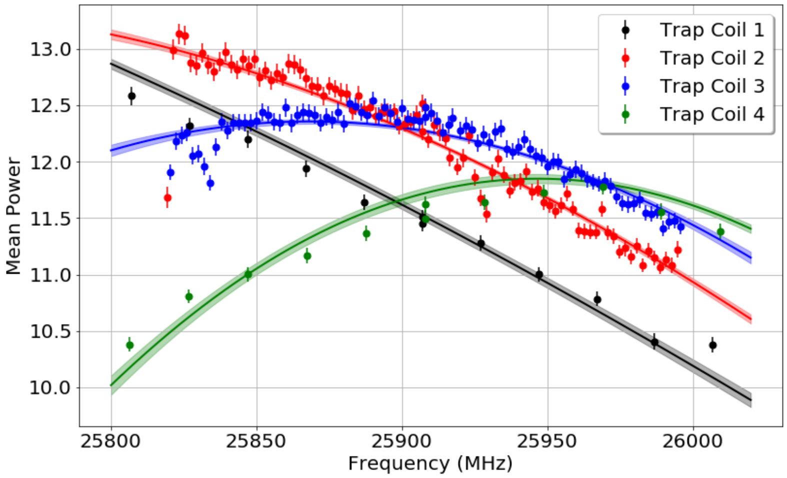

Figure 4.40: The averaged power from the fitted gamma distribution to the tracks' normalized power as a function of the frequency. The data taken in trap coils 1-4 are shown. The fit is performed with the use of the function in (4.20) which models the interference pattern caused by reflection off the lower window and the terminator.

which the R.F. power can reflect back and make an interference pattern. The lower window and the terminator are the only two places below the gas cell which can cause an interference pattern traveling upward toward the amplifier stage. In the last chapter we worked out the effect of a perfect reflector on the power spectrum. The effect of two physical reflectors on the power spectrum can be modeled by multiplying the power with the reflection factor,

$$Q_r(f) = a_1 + a_2 \cos 2kl + a_3 \cos 2k\ (l - l_0), \tag{4.20}$$

in which k, l, and l_0 are respectively the wave-number, the axial distance between the center of the trap and the terminator, and the distance between the terminator and the lower window. The fits presented in Fig. 4.40 are performed using this function to simultaneously explain the power behavior of all the four traps.

The next step in this analysis is to relate the power to the number of electron counts in each trap. Fig. 4.13 shows that the radiated cyclotron power from the trapped electrons follows an exponential distribution,

$$P_P(p) = \beta e^{-\beta p}. \tag{4.21}$$

The power distribution in the interference pattern caused by the reflections can be calculated using the above distribution. The track powers are multiplied by the factor in Eq. (4.20) and hence,

$$P_{Q_r \cdot P}(p) = \frac{\beta}{Q_r} e^{-\frac{\beta}{Q_r} p}. \tag{4.22}$$

The number of detectable tracks can be deduced by modeling the track and event reconstruction as a simple cut in the power. In this simplistic model the tracks are detectable if their power is above a given threshold, P_0. Therefore the number of counts are,

$$\begin{aligned} N &= N_0 \int_{P_0}^{\infty} P_{Q_r \cdot P}(p)\ \mathrm{d}p \\ &= N_0 \int_{P_0}^{\infty} \frac{\beta}{Q_r} e^{-\frac{\beta}{Q_r} p}(p)\ \mathrm{d}p \\ &= N_0 e^{-\frac{\beta}{Q_r} P_0}, \end{aligned} \tag{4.23}$$

in which N_0 is the total number of trapped electrons. Next we need to estimate the averaged track power for any given reflection factor, Q_r. The same assumption in the derivation of the number of counts in Eq. (4.23) can be used here to find the averaged power,

$$\begin{aligned} \overline{P} &= \frac{N_0}{N} \int_{P_0}^{\infty} p\ P_{Q_r \cdot P}(p)\ \mathrm{d}p \\ &= \frac{N_0}{N} \int_{P_0}^{\infty} p\ \frac{\beta}{Q_r} e^{-\frac{\beta}{Q_r} p}(p)\ \mathrm{d}p \\ &= P_0 + \frac{Q_r}{\beta}. \end{aligned} \tag{4.24}$$

The two derived relations in Eq. (4.23) and (4.24) can be used to relate the number of counts to the averaged power by substituting the $\frac{Q_r}{\beta}$ factor. The result is a function relating the number of counts to the averaged power,

$$N(\overline{P}) = N_0\ e^{\frac{1}{1-\frac{\overline{P}}{P_0}}}. \tag{4.25}$$

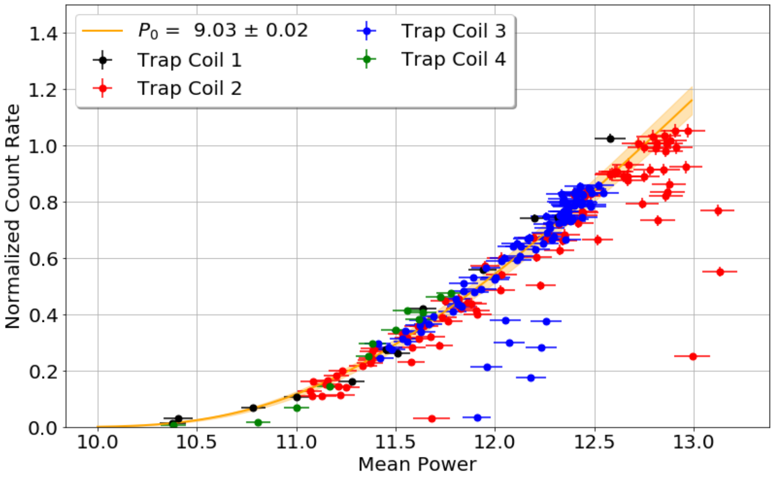

Figure 4.41: Normalized count rate as a function of averaged track power. The fit is performed with the use of the function in Eq. (4.25).

Fig. 4.41 shows the normalized count rate vs. the averaged power plotted in Fig. 4.40. The fit is performed using the function in Eq. (4.25) using the technique introduced in Appx. E to include the errors in the mean power. The points with lower count rate than expected belong to the frequencies at which a large TM_{01} resonant structure is present. In these frequencies a higher value of the slope reduces the number of detectable tracks. The dependency of the track and event reconstruction efficiency on the track's slope is represented in Fig. 4.5.

The two functions introduced in Eq. (4.25) and Eq. (4.20) provide enough information to predict the count rate in the field shifting solenoid's single trap data sets. Fig. 4.42 shows the prediction made using these two functions. The deficit in the count rate at $\sim$ 25830 MHz and $\sim$ 25930 MHz are modeled with a Lorentzian function. This function is used because of the Lorentzian shape of a resonant mode. The count rate deficit in the second trap coil at $\sim$ $25860 - 25870$ MHz has an irregular shape and hence a linear interpolation is used to model it. The fall of the count rate at low frequencies is also expected. This can be explained by recalling that there are no krypton spectrum recorded at lower frequencies (higher field shifting solenoid currents 4.35). Hence the number of krypton lines with different field shifting solenoid currents contributing to the count rate at lower frequencies is lower.

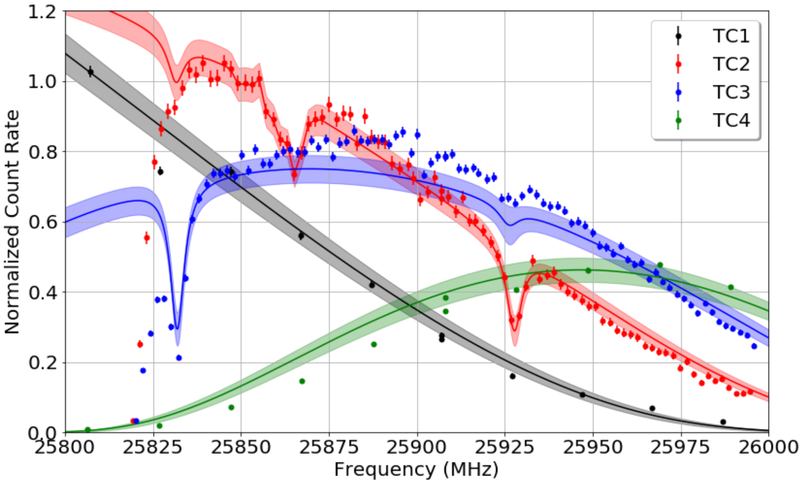

Figure 4.42: Normalized count rate as a function of frequency. The prediction is made with the use of the functions in Eq. (4.25) and Eq. (4.20). The deficit in the count rate is caused by the high slope of the tracks in the frequencies where a strong TM_{01} resonant mode is present.

At this point we have established a framework that can predict the power and efficiency curve for the Q-300 trap configuration. For predicting the averaged power we use a weighted sum of the averaged power in each trap using Eq. (4.25) and Eq. (4.20),

$$\overline{P} = \frac{\sum_{i=1}^{4} \overline{P_i}\, e^{\frac{1}{1-\frac{\overline{P_i}}{P_0}}}\, S_i(f)}{\sum_{i=1}^{4} e^{\frac{1}{1-\frac{\overline{P_i}}{P_0}}}\, S_i(f)}, \tag{4.26}$$

where $\overline{P_i}$ is the averaged power in the i^{th} trap and $S_i(f)$ is the count deficit in the i^{th} trap caused by the high slope tracks. Fig. 4.43 illustrates the averaged track power in Q-300 trap with the prediction made using the Eq. (4.26). The parameters in this equation are deduced from the fits to single trap data sets.

The efficiency curve can also be predicted using the same framework. Similar to the averaged power relation in Eq. (4.26), the expected count rate is,

$$N = N_0 \sum_{i=1}^{4} e^{\frac{1}{1-\frac{\overline{P_i}}{P_0}}}\, S_i(f). \tag{4.27}$$

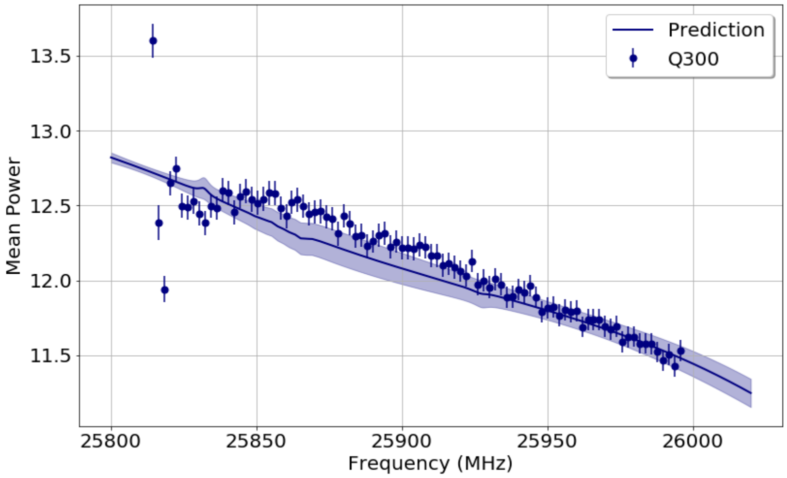

Figure 4.43: Averaged track power as a function of frequencies in Q-300 trap geometry. The prediction is made with the use of Eq. (4.26).

Fig. 4.44 shows the prediction and measured count rate in the Q-300 trap geometry. It is obvious that the number of counts is less than expected.

The difference between the prediction and measured count rate is by no means surprising. The count rate in the Q-300 trap geometry should be less than the combined count rate of the three individual traps. The reason is the cross-effect of trap coils on each other. This cross-effect is changes the shape of the individual traps at larger radii and axial positions farther from the center of the trap. Therefore the effect is enhanced for the bins with higher averaged power. The reason is that the higher averaged power bins can detect electrons at larger radii with smaller pitch-angles. These electrons are the ones which are affected the most with the cross-effect between traps. We use a simple line to model this effect and fix the deficit in the count rate. The corrected prediction is shown in Fig. 4.45.

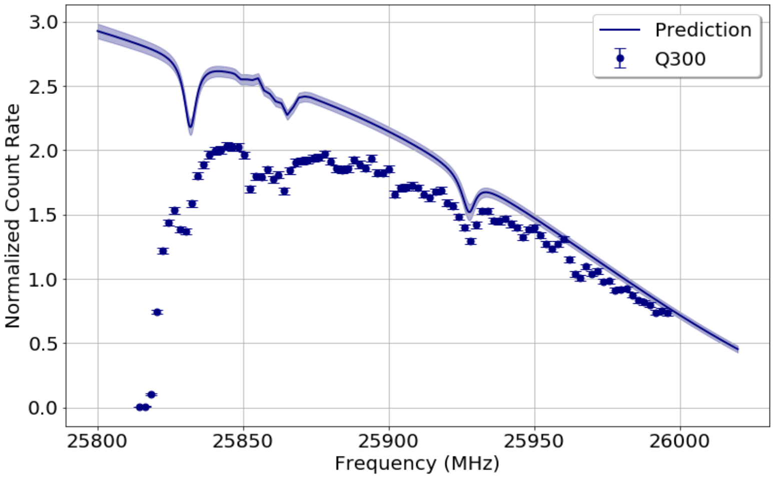

Figure 4.44: Normalized count rate as a function of frequency in Q-300 trap geometry. The prediction is made with the use of Eq. (4.27).

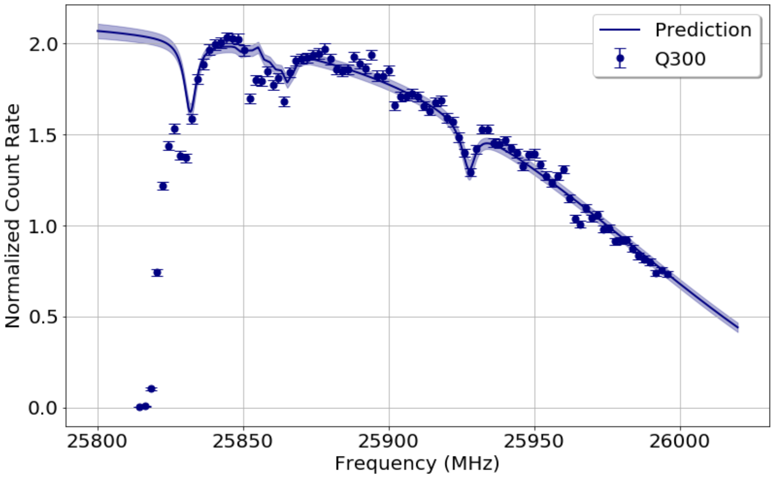

Figure 4.45: Normalized count rate as a function of frequency in Q-300 trap geometry. The prediction is made with the use of Eq. (4.27). The prediction also includes a linear change in the count rate to model the cross-effect of the trap coils in the Q-300 trap geometry.

Chapter 5

TRITIUM SPECTRUM MEASUREMENT AND ANALYSIS

The main objective of the second phase of Project 8 experiment is to measure a tritium spectrum and to infer an endpoint value and a neutrino mass limit. This chapter is dedicated to the analysis of the tritium data recorded with the project 8 demonstrator's apparatus.

Here we present the data analysis of the tritium spectrum. The importance of the calibration data analyzed in the last chapter will become evident here. The knowledge about the CRES power spectrum discussed in chapter 3 will also be crucial in analysing the tritium data.

5.1 Tritium Spectrum

Tritium is a super-allowed beta-decay isotope with an endpoint value of $Q = 18575.72 \pm 0.07\ eV$ [47]. The relatively low value of the endpoint produces a larger fraction of electron events with energies close to the endpoint. The super-allowed nature of the nuclear transition also leads to an energy-independent nuclear matrix element. For tritium the value for this matrix element is $|M_{nuc}^2| = 5.55$ [53].

These advantageous features make the tritium a favorable isotope for the direct study of the neutrino mass. Furthermore, the gaseous state of the tritium in temperatures above 25 K makes it a viable choice for CRES type spectroscopy.

The full spectrum of the tritium can be written as

$$R_\beta(E) = \frac{G_F^2 \cos^2\theta_c}{2\pi^3} \left|M_{nuc}^2\right| F(E, Z=2) p_e \epsilon (E + m_e) \sum_i |U_{ei}|^2 \sqrt{\epsilon^2 - m_{\nu_i}^2}\ \Theta(\epsilon - m_{\nu_i}) \quad (5.1)$$

in which G_F, Θ_c, p_e, and E are the Fermi constant, the Cabibbo angle, electron's momentum, and the electron's kinetic energy. $\epsilon = E_0 - E$ is the electron anti-neutrino's energy where

E_0 is the effective endpoint value of the tritium spectrum whose value is 1.72 eV lower than the Q-value due to the recoil of the T_2 molecule [47]. The Fermi function in Eq. (5.1),

$$\begin{aligned} F(E,Z) &\approx \frac{x}{1-e^{-x}}, \\ x &= \frac{2\pi Z\alpha}{v/c} \end{aligned} \tag{5.2}$$

where α is the fine structure constant, models the Coulomb interaction of the emitted electron with the daughter nucleus.

The sum in Eq. (5.1) is over the three mass states of the electron anti-neutrino with U_{ei} being the elements of Pontecorvo–Maki–Nakagawa–Sakata matrix. In cases where the experiment's energy resolution is wider than the mass differences, the spectrum can be rewritten with an effective value of neutrino mass state where,

$$m_\beta^2 = \sum_i |U_{ei}|^2 m_{\nu_i}^2. \tag{5.3}$$

The final spectrum used in the analysis of the tritium data is

$$R_\beta(E) = AF(E, Z=2) p_e \epsilon (E + m_e) \sqrt{\epsilon^2 - m_\beta^2}\ \Theta(\epsilon - m_{\nu_i}), \tag{5.4}$$

where A is an amplitude used as a free parameter in the fit.

5.2 Tritium Data

The ultimate tritium data taking campaign started on December 12th 2019 and finished on March 18th 2020. Three channels of the ROACH data acquisition system were used simultaneously to record electron events in the frequency range of 25820-26010 MHz corresponding to the energy range of 15.7-19.6 keV (Fig. 5.1[1]). This energy range was chosen to include a 1 keV region beyond the endpoint to illustrate the capability of the CRES type experiment in recording low background spectra.

Fig. 5.2 shows the gas pressure evolution during this time. It is apparent that the tritium storage getter has maintained a stable gas pressure. Fig. 2.30 shows the gas composition

---

[1] The analysis for this plot has been done by Christine Claessens (claessen@uni-mainz.de).

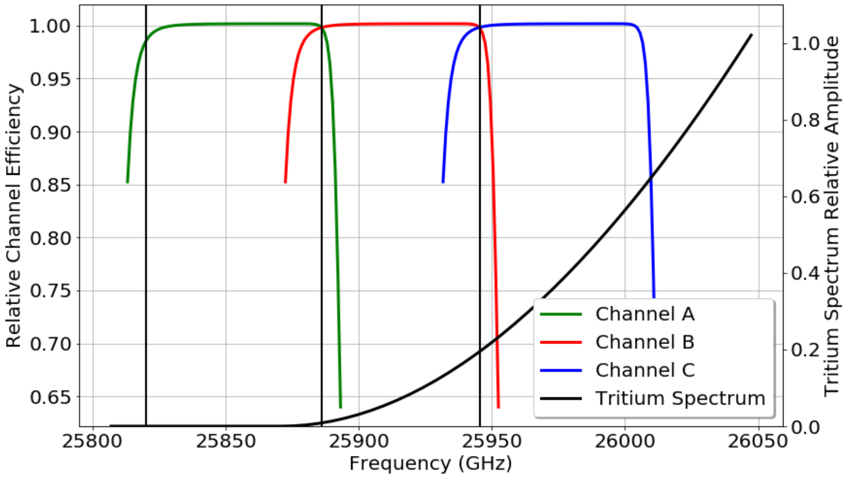

Figure 5.1: The alignment of the three data acquisition channels in the frequency domain. The channel curves represent the efficiency of the channel in detecting electron events. The curve is not measured at the frequency edges where the efficiency is lower. The tritium spectrum shows the relative position of the channels.

recorded in the SRS Residual Gas Analyzer installed near the gas cell during the tritium data taking (see Fig. 2.21).

During this data taking campaign a total of 5533 electron events were recorded. Fig. 5.3 shows the frequency histogram of the events recorded in each of the three Roach system channels. To construct the final spectrum we performed a number of frequency cuts for each channel. This was done to exclude double counting of the events that were registered with two channels. The frequency cuts are marked in Fig. 5.1 with solid lines. Events in channel A below 25945.6 MHz, in channel C above 25886.2 MHz, and in channel B below 25886.2 MHz and above 25945.6 MHz were cut. These cuts were also performed to ensure that the channel efficiency does not play a role in the efficiency curve calculations. A total number of 4478 unique electron counts survive these frequency cuts. Fig. 5.4 shows the energy histogram of the final data set.

Fig. 5.5 illustrates the first track slope and start-frequency of the recorded events. The presence of the resonant structures in the slope is apparent. A comparison with Fig. 4.36

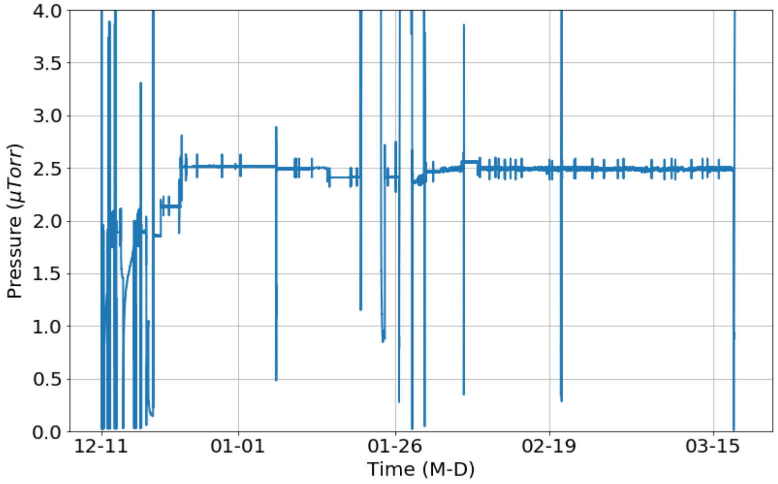

Figure 5.2: Gas pressure during the tritium run. The pressure is recorded with IG2 (Fig. 2.21).

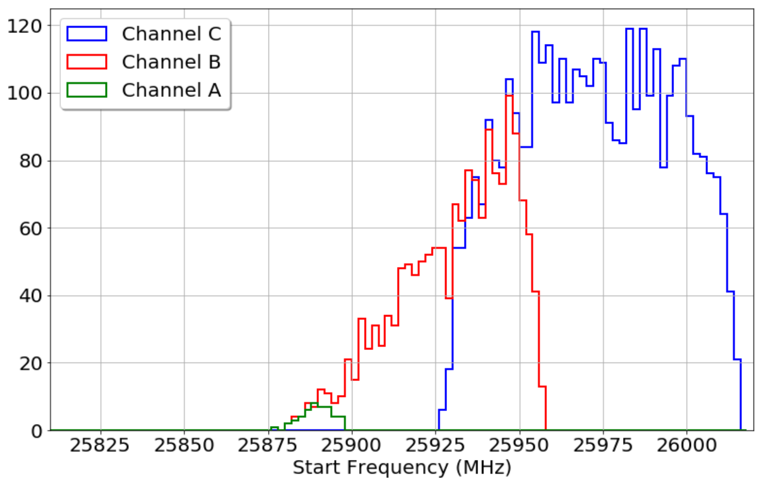

Figure 5.3: start-frequency histogram for the electrons recorded in the three channels of the Roach data acquisition system.

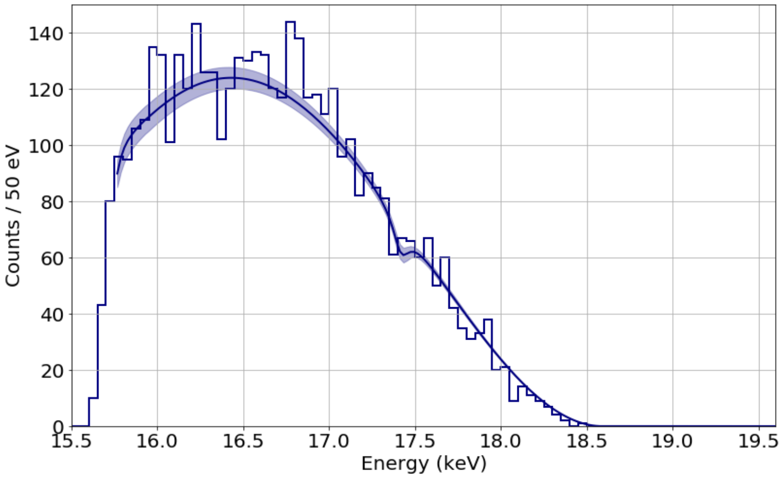

Figure 5.4: Energy histogram of the electrons after applying the appropriate frequency cuts to the events in the three channels of the data acquisition system. The efficiency curve multiplied by the beta-decay spectrum is shown with the corresponding uncertainties. The efficiency curve below 15.7 keV is not known due to the unknown channel efficiency.

proves that the resonant structure in the tritium data is identical to the ones discovered with the frequency systematics study performed with the field shifting solenoid.

Fig. 5.6 presents the first track power and start-frequency of the tritium events. It was shown in the last chapter that the track power plays a major role in shaping the efficiency curve. One important effect that needs to be accounted for is that the electron's coupling to the waveguide mode is different for the krypton and the tritium data. In the case of the systematic study performed with the field shifting solenoid the energy of the conversion electron does not change. The frequency change is caused through a change in the background field induced by the field shifting solenoid. However, the beta electrons from the tritium have different energies in a constant magnetic field. Thus the cyclotron frequency of the beta particles vary due to their energy variations. The electron coupling to the waveguide for these two cases can be calculated using Eq. (3.69). Fig. 5.7 presents the result of this calculation. As expected, tritium events with energies above the krypton's conversion electrons couple more strongly to the waveguide mode while the lower energy electrons have

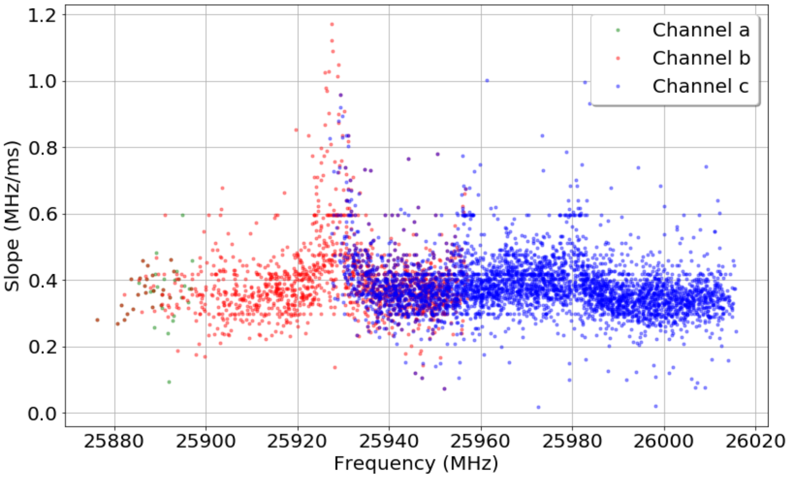

Figure 5.5: Slope vs. start-frequency for electrons recorded in the three channels of the Roach data acquisition system.

a weaker coupling. We will use this calculation in the next section to modify the efficiency curve calculation of the last section for the tritium spectrum.

5.3 Efficiency Curve

In the last chapter we showed how the power changes due to reflection from the terminator and the lower window and the resonant structures in the slope shaped the efficiency curve. In the last section we mentioned that the slope structures are similar in tritium and krypton data. However to modify the efficiency curve for the tritium data the electron coupling difference needs to be incorporated.

Eq. 4.24 shows how the reflection factor modifies the power in the systematic study performed with the help of the field shifting solenoid. The reflection is a spectral feature which is present independent of the gas type or the energy of the electron. To find the tritium power we added a factor Q_{tr} which is the ratio of the tritium coupling to the waveguide mode

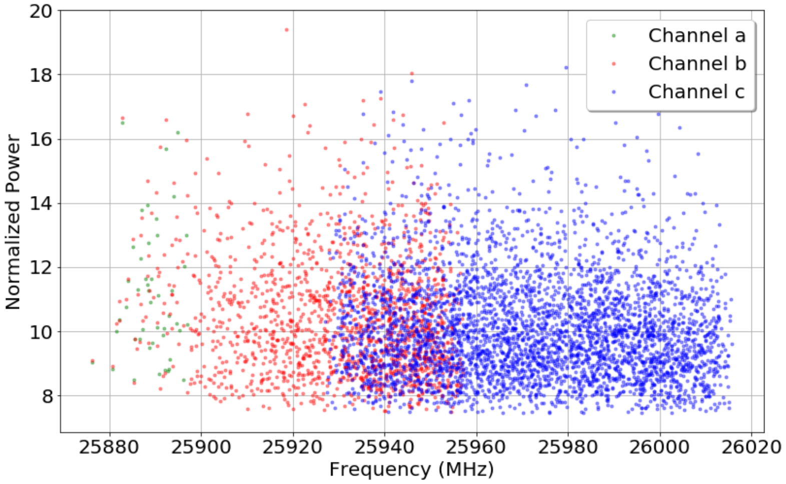

Figure 5.6: Normalized power vs. start-frequency for electrons recorded in the three channels of the Roach data acquisition system.

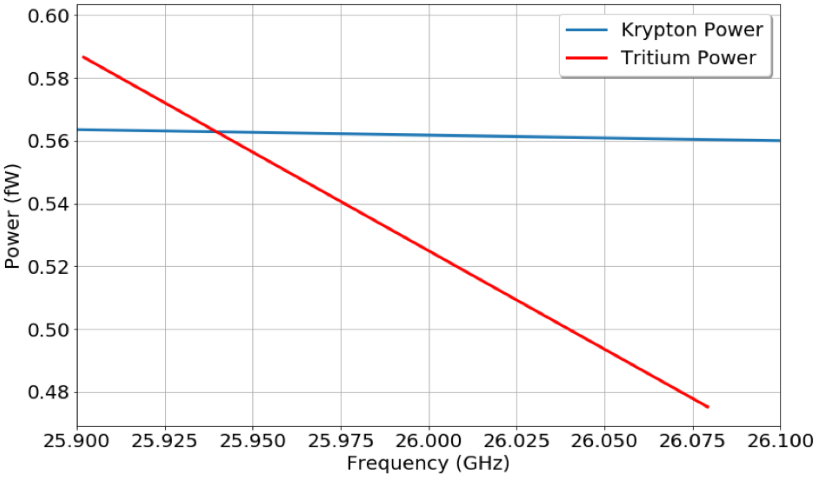

Figure 5.7: Comparison of the radiated power of krypton's conversion electrons in a varying background field with the radiated power of beta electrons at different energies.

to that of a krypton at a given frequency [2]. Hence for the tritium power we get,

$$\bar{P}_{tr} = P_0 + \frac{Q_{tr}Q_r}{\beta}. \tag{5.5}$$

Comparing this equation to Eq.(4.24) helps us to find the modification we need for the tritium data efficiency curve calculation, where

$$\bar{P}_{tr} = P_0 + Q_{tr} \cdot (\bar{P}_{kr} - P_0). \tag{5.6}$$

Modifying the efficiency curve calculation presented in the previous chapter with this equation produces the efficiency curve for the tritium data. Fig. 5.4 presents the tritium data with the tritium spectrum multiplied by the efficiency curve. We do not include the very high frequency events above 26012 MHz in our analysis due to the unknown efficiency of the ROACH system channels at higher frequencies.

5.4 Line-Shape

In section 4.2.1 we studied the spectral features of the CRES signal using the krypton conversion electrons. We used a complex line-shape model, presented in Eq. (4.13), to fit the frequency spectrum. For modeling the line-shape for the beta electrons from the tritium spectrum we start with the same model. The most significant difference is the gas composition inside the gas cell. The background during the tritium data taking mainly consists of tritium and helium gases with an insignificant amount of krypton pressure. However the exact gas composition is not known for the tritium run and hence a number of different scenarios are used to find the appropriate line-shape. The gas composition uncertainty is then translated into the parameters of the line-shape.

The model in Eq. 4.13 needs to be convolved first with a Gaussian to model the finite energy resolution of the receiver, and then with the tritium spectrum in Eq. (5.4) for evaluating the expected spectrum. For energy resolutions wider than 30 eV, the result of the convolution with $f_{(n,0)}$ functions can be approximated with Gaussian functions. The mean

---

[2] Q_{tr} is the result of dividing the red curve in Fig. 5.7 by the blue curve.

and the standard deviation of these Gaussian functions are estimated by using empirical fits to simulated data using the exact model presented in Eq. (4.13),

$$\begin{aligned} \sigma_n &= P_{0n} + P_{1n} \cdot FWHM \\ \mu_n &= P_{2n} + P_{3n} \cdot \ln(FWHM - 30), \end{aligned} \tag{5.7}$$

where the FWHM is the energy resolution of the system in eVs. The four coefficients are evaluated by fitting to fake events generated by our simulation package [20]. The result is the simplified line-shape where [3]

$$L = \sum_{n=0}^{N} N_0 P^n G_n(-\mu_n, \sigma_n). \tag{5.8}$$

Comparing this simplified line-shape with Eq. (4.13) can relate the quantities of this model to the physically motivated coefficients. Thus $N_0 = a\rho$ is the amplitude multiplied by the probability of track detection. Moreover, $P = (1-\rho)\sigma\gamma_H$ is the probability that the first track is not detected and the electron has scattered once after that. This coefficient is named *Survival Probability.* Fig. 5.8 shows the line-shape with the inclusion of 20 scattering with a 36 eV wide energy resolution.

To find the two parameters of the line-shape model, the survival probability and the energy resolution, a fit is performed to a krypton data set taken after the conclusion of the tritium data campaign. This calibration data set is recorded with the exact same final trap configuration. To propagate the uncertainty on the gas composition five slightly different compositions are used to fit the data. These compositions are based on the residual gas analyser data taken during the krypton run. The difference between the concluded parameters is assigned to the uncertainty for the parameters of the fit.

The energy resolution uncertainty also has a contribution from the krypton systematic study performed with the field shifting solenoid. The energy resolution distribution in the field shifting solenoid data is added to incorporate any change in the frequency region of

---

[3] This model is developed by Xueying Huyan (xueying.huyan@pnnl.gov).

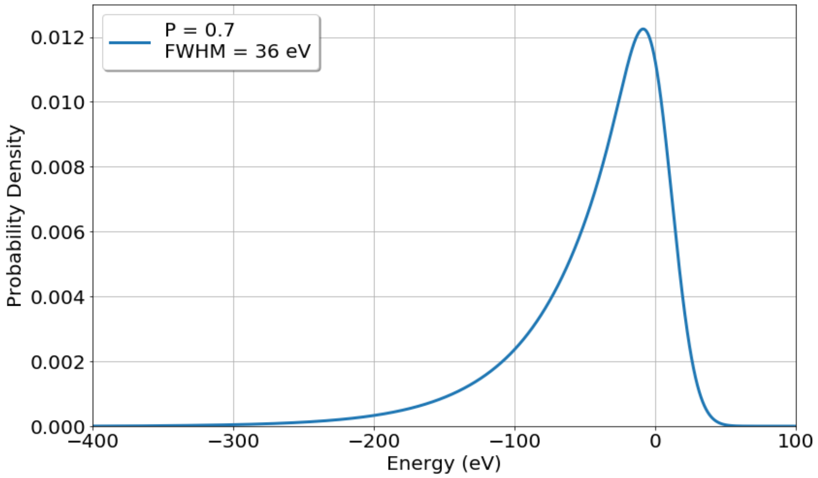

Figure 5.8: Simplified Line-shape function according to Eq. (5.8) with the given parameters. The line-shape is normalized and hence the y-axis represents the probability density.

interest. The magnetic field is another parameter which is derived from the fit to this data set. The result of this study is presented in Tbl. 5.1 [4].

Parameter	Value	Uncertainty
Survival Probability	0.67	0.11
Energy Resolution	36.5 eV	5.2 eV
Magnetic Field	0.9578095 T	8.5e-6 T

Table 5.1: Line-shape parameters extracted from the krypton systematic data.

5.5 *Constructing the Log-Likelihood*

To infer the tritium endpoint value and the neutrino mass, we perform a binned analysis. The Poisson regression method is the technique used for building the log-likelihood due to

---

[4] This table is the result of an extensive study by Elise Novitski (en37@uw.edu), Talia Weiss (tweiss@mit.edu), and Yu-Hao Sun (yxs682@case.edu).

the Poisson nature of the radioactive decays.

The log-likelihood is,

$$\begin{aligned} -2\ln L(\mathbf{n};\boldsymbol{\theta}) &= -2\ln\left(\prod_{i=1}^{n}\frac{L(n_i;\mu_i)}{L(n_i;n_i)}\right) = -2\ln\left(\prod_{i=1}^{n}\frac{\mu_i^{n_i}e^{-\mu_i}}{n_i!}\frac{n_i!}{n_i^{n_i}e^{-n_i}}\right) \\ &= 2\sum_{i=1}^{n}\left[\mu_i(\boldsymbol{\theta}) - n_i + n_i\ln\left(\frac{n_i}{\mu_i(\boldsymbol{\theta})}\right)\right] \end{aligned} \tag{5.9}$$

where $\boldsymbol{\theta}$ is the set of m parameters, n_i are the number of counts in the ith bin, and μ_i is the expected number of counts in the ith bin. The $L(n_i; n_i)$ is a constant factor added to the log-likelihood which does not change the minimum of the function. The addition of this extra factor makes the log-likelihood function to asymptotically obey the χ^2 distribution with $n - m$ degrees of freedom [37].

To find the expected number of counts in each bin, first the convolution of the tritium spectrum with the simplified line-shape introduced in the last section is calculated. We then apply the tritium efficiency curve to the spectrum. The expected number of counts in each bin is the average of the resulting curve over a bin size. Fig. 5.9 shows the tritium count rate at every step of this calculation.

For fitting the spectrum shown in Fig. 5.4 two separate assumptions are used. First, the neutrino mass is set to zero to measure the endpoint value. The value of the survival probability and the energy resolution are fixed to the numbers given in Tbl. 5.1. A constant background rate is also added to the spectrum. The *iminuit* package is used to minimize the log-likelihood function. The free parameters in this fit are the amplitude (A), the effective beta-decay endpoint energy (E_0), and the background rate (b). The result of minimizing the log-likelihood is,

$$\begin{aligned} E_0 &= 18574.1 \pm 17.2\ eV \\ b\ &< 1.72\times 10^{-10}\ (eV.s)^{-1}\ (90\%\ C.L.). \end{aligned} \tag{5.10}$$

The goodness of the fit can be expressed by stating the $-2\ lnL = 51.8$ for 75 degrees of freedom.

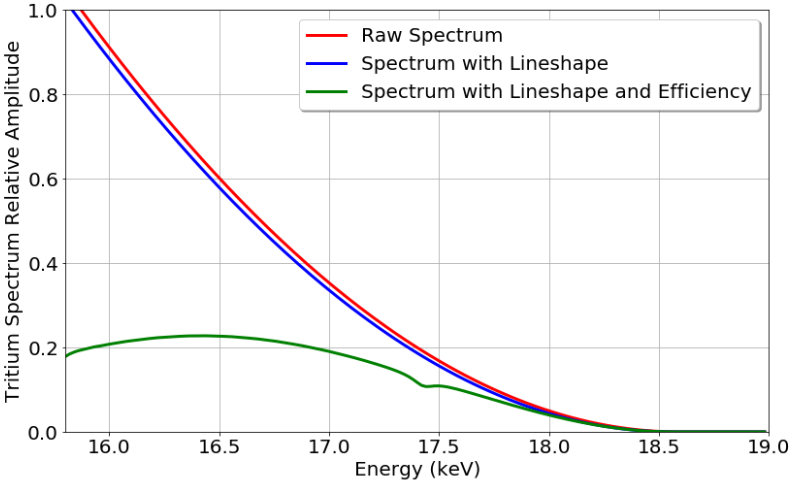

Figure 5.9: The tritium raw spectrum, the spectrum with the inclusion of the simplified line-shape (Fig. 5.8), and the spectrum with the inclusion of both the line-shape and the efficiency curve. Note that the absolute amplitude of the curve with the efficiency is exaggerated for comparison.

In the second scenario a non-zero neutrino mass is added to the model. The values for the survival probability and the energy resolution are fixed again. The resulting parameters from the log-likelihood minimization in this case are,

$$\begin{aligned} E_0 &= 18580.2 \pm 23.2 \; eV \\ m_\beta^2 &= 4020^{+17000}_{-82000} \; eV^2 \; (90\% \; C.L.) \\ b \; &< 1.76 \times 10^{-10} \; (eV.s)^{-1} \; (90\% \; C.L.). \end{aligned} \tag{5.11}$$

The minimum of the log-likelihood function for the fit is $-2 \; lnL = 51.6$ for 74 degrees of freedom.

5.6 Systematic Effects

The main systematic effects in this analysis are the uncertainty in the survival probability coefficient of the simplified line-shape model in Eq. (5.8), the energy resolution uncertainty, the background field uncertainty, and the uncertainty in the efficiency curve. In order to study these systematic effects a number of fake experiments with large statistics are run. The

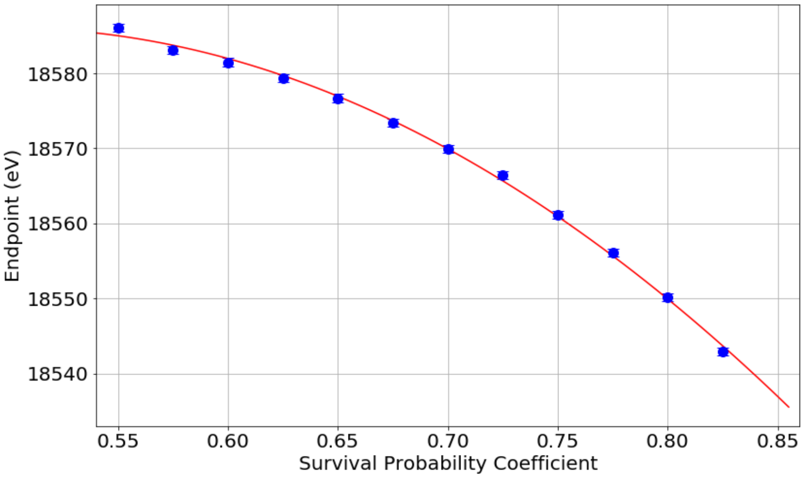

Figure 5.10: Result of the fake experiment runs for the study of the survival probability effect on the endpoint measurement. Each point represents a single fake experiment with the given survival probability. The endpoint is extracted with the fixed value of the survival probability given in Tbl. 5.1. A linear fit is used to fit the points.

value of the parameters under study is altered during each experiment. The log-likelihood is then constructed and minimized with the fixed values in Tbl. 5.1 to study the effect of the miss-assignment of the parameter on the endpoint and the neutrino mass measurements.

Fig. 5.10 shows the result of this study for the survival probability in the simplified lineshape. Each point in this plot represents a single fake experiment run with the given survival probability. The value of the magnetic field and the energy resolution parameters are fixed with the numbers provided in Tbl. 5.1. As can be seen, the uncertainty in the survival probability leads to a miss-calculation of tritium endpoint energy. To find the systematic uncertainty effect of survival probability the endpoint energy change corresponding to the uncertainty of the survival probability presented in Tbl. 5.1 is calculated. The result is shown in Tbl. 5.2.

The same technique is used to find the systematic effects of the magnetic field and the energy resolution in Fig. 5.11 and 5.12. Tbl. 5.2 gives the result of these studies. To calculate the contribution of the efficiency curve uncertainty to the systematics, similar plots

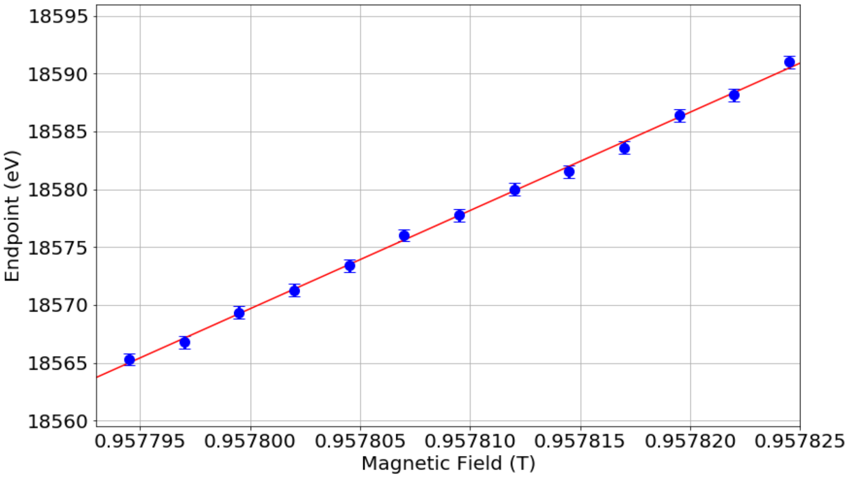

Figure 5.11: Result of the fake experiment runs for the study of the magnetic field effect on the endpoint measurement. Each point represents a single fake experiment with the given magnetic field. The endpoint is extracted with the fixed value of the magnetic field given in Tbl. 5.1. A second degree polynomial is used to fit the points.

are generated to find the changes in the endpoint energy with respect to the parameters in the efficiency curve. These parameters are a_1, a_2, b, and $l_1 - l_4$ from Eq. (4.20) and P_0 from Eq. (4.25). The covariance matrix from the fits shown in Fig. 4.40 is used to find the value reported in Tbl. 5.2. At the end, the different systematic values are added in quadrature to find the final systematic effect.

The final value of tritium endpoint extracted with the inclusion of the systematic and statistical uncertainty is,

$$\boxed{\boldsymbol{E_0 = 18574.1 \pm (17.2)_{stat.} + \left({}^{+12.5}_{-21.1}\right)_{sys.}\ eV.}} \tag{5.12}$$

Tbl. 5.3 shows the result of a similar study for the model with the neutrino mass. These systematic uncertainties can be added to the statistical uncertainty to conclude a mass-squared value. However this simplistic method ignores the fact that the mass-squared

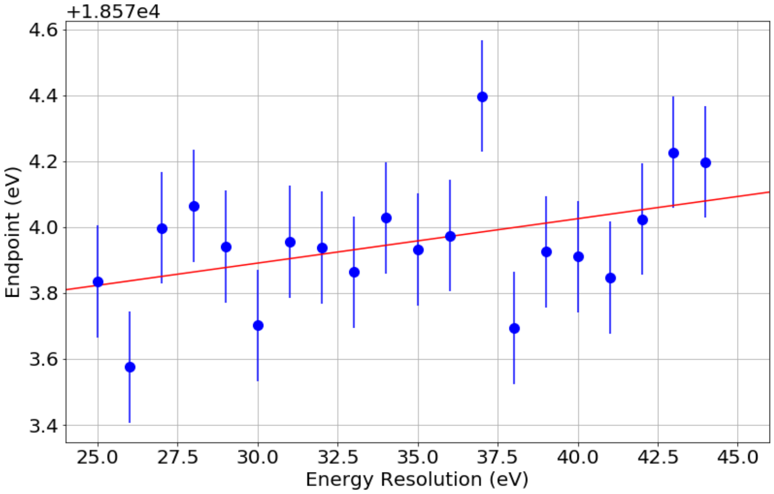

Figure 5.12: Result of the fake experiment runs for the study of the energy resolution effect on the endpoint measurement. Each point represents a single fake experiment with the given energy resolution. The endpoint is extracted with the fixed value of the energy resolution given in Tbl. 5.1. A line is used to fit the points.

Effect	$\sigma(E_0)$ eV
Survival Probability	$^{+10.2}_{-19.8}$
Magnetic Field	7.2
Energy Resolution	0.1
Efficiency Curve	0.9
Total	$\boldsymbol{^{+12.5}_{-21.1}}$

Table 5.2: Systematic effects on the tritium endpoint energy measurement.

cannot have negative values. This prior knowledge can be used to find the mass-squared confidence interval. To do this the method introduced in [39] has been used.

Fig. 5.13 shows the plot resulted from applying this technique. The real value of the mass-squared is represented in the y-axis while the estimated value is drawn on the x-axis. The maroon region is representing the 90% confidence interval with only the statistical uncertainty included. The systematic uncertainty is then calculated to add the navy band. The confidence interval is the vertical distance in the band at the value of the neutrino mass-squared found from log-likelihood minimization in Eq. (5.11). The final result is an upper bound for the electron neutrino mass,

$$\boxed{\boldsymbol{m_\beta \ < 146\ eV\ \ (90\%\ C.L.).}} \tag{5.13}$$

Effect	$\sigma(m_\beta^2)\, eV^2$ (90% $C.L.$)
Survival Probability	$^{+2700}_{-5700}$
Magnetic Field	1500
Energy Resolution	600
Efficiency Curve	700
Total	$\mathbf{^{+3200}_{-6000}}$

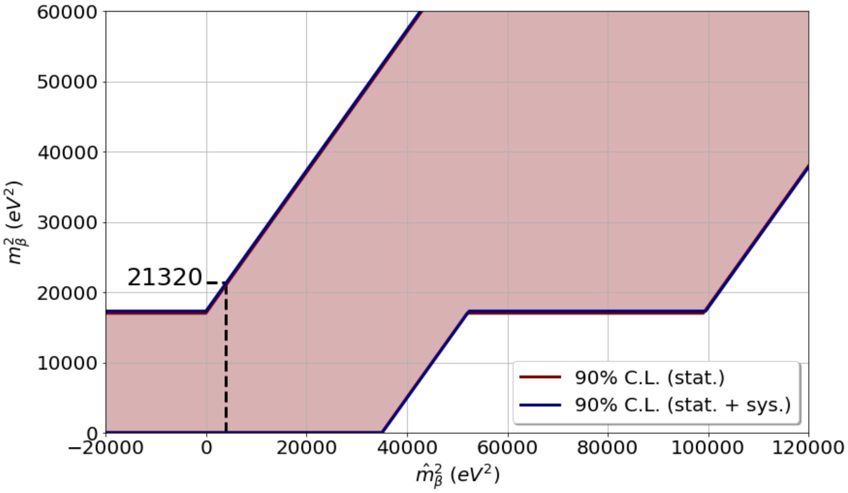

Figure 5.13: Confidence interval for the neutrino mass-squared values. The y-axis is the real value and the x-axis shows the estimated parameter. For any given estimation of the mass-squared the 90% confidence interval can be found using the vertical line with the given estimation x-value. The vertical dashed line represents the value[**?**] from the log-likelihood minimization in Eq. 5.11.

Chapter 6

CONCLUDING REMARKS

A decade after the proposal of the CRES technique, project 8 collaboration has measured the first tritium spectrum. The success of the second phase of the experiment paved the road for project 8 collaboration to construct the next generation of the neutrino mass measurement experiments.

The major challenge in the next phase of the experiment is the detection of the cyclotron radiation with an antenna array. This new detecting scheme requires major efforts starting from the design and construction of the new gas cell. Developing an updated phenomenological model for the free-space cyclotron radiation is also required. These upgrades will necessitate a revised data analysis chain.

The success of the project 8 in the second phase of the experiment has its effect on other areas of nuclear physics. This new technique can be used by other collaborations for measuring electron energies. Testing the noble element atomic energy levels and photoelectric cross sections and the measurement of helium-6 spectrum are two examples of proposed projects which can use CRES [31].

We finish this work by suggesting a number of changes that can assist other experiments in their design and construction. Some of these proposed upgrades can also be used in the next phase of the project 8 experiment.

6.1 Possible Improvements

6.1.1 Improving the Signal to Noise Ratio

As it was explained in Chapter 2, a terminator was used to absorb half of the radiated cyclotron power of the electron. This was done to minimize the effect of reflection in the

CRES spectrum. An alternative technique can be used to detect the full radiated power without the challenges of the interference.

One possible solution is to employ two sets of antennas to detect the radiated power of electrons emitting in both directions in the waveguide. Two RF circulators are needed to stop the amplifier noise from re-emission to the gas cell.

One other advantage of using two sets of antennas is the better detection of the Doppler effect. Detecting the radiation in both directions with proper time resolution can measure the blue-shifted and red-shifted frequencies. This can be used to find the axial frequency of the electron which is an extra piece of information that can provide better energy resolution by determining the electron pitch-angle.

6.1.2 Improving the Gas System Design

Throughout the operation of the phase II gas system we encountered a number of challenges. One of these challenges was the ever growing background pressure from helium-3. Helium-3 is the daughter nucleus remnant of the tritium beta decay.

There existed two main sources of helium-3. First, the tritium molecules deposited on the walls of the gas system as the storage getter was loaded with 2 Ci of tritium, were releasing a considerable amount of helium-3. Second, the tritium molecules in the storage getter also release a substantial amount of helium-3 after they beta decay.

To minimize this background pressure a number of improvements can be made in the next phases gas systems.

- Make the source closer to the storage getter to minimize the exposed surface to the high pressures of tritium during the loading process.

- Separate the storage getter from the operation getter. This can help to minimize the background pressure of helium-3 released from the getter during the operation. The operation getter can be reloaded with tritium in the storage getter.

- Add a high resolution residual gas analyzer close to the gas cell. This can help to better understand the gas composition inside the gas-cell.

6.1.3 Miscellaneous

It was mentioned in Chapter 4 that the use of shallow traps can help us achieving great energy resolution. A flat background field is a requirement for reaching sub-eV energy resolutions. These resolutions are achievable with the use of super shallow traps that minimize the trap field variations. The super shallow traps can operate only in the presence of a flat background.

The last suggestion is related to the resonant structures shown in Fig. 4.36. These structures can be avoided by using a smaller radius of the circular waveguide. The smaller radius results in a higher cut-off frequency for the TM_{01} mode in the circular waveguide. Hence the radiated power of the electrons does not couple to this mode and hence the resonant structure vanishes.

BIBLIOGRAPHY

[1] St 171 and st 172 - sintered porous getter. *Product data sheet.*, 2007.

[2] M. Agostini, A. M. Bakalyarov, M. Balata, I. Barabanov, L. Baudis, C. Bauer, E. Bellotti, S. Belogurov, A. Bettini, L. Bezrukov, J. Biernat, T. Bode, D. Borowicz, V. Brudanin, R. Brugnera, A. Caldwell, C. Cattadori, A. Chernogorov, T. Comellato, V. D'Andrea, E. V. Demidova, N. Di Marco, A. Domula, E. Doroshkevich, V. Egorov, R. Falkenstein, A. Gangapshev, A. Garfagnini, P. Grabmayr, V. Gurentsov, K. Gusev, J. Hakenmüller, A. Hegai, M. Heisel, S. Hemmer, R. Hiller, W. Hofmann, M. Hult, L. V. Inzhechik, J. Janicskó Csáthy, J. Jochum, M. Junker, V. Kazalov, Y. Kermaidic, T. Kihm, I. V. Kirpichnikov, A. Kirsch, A. Kish, A. Klimenko, R. Kneißl, K. T. Knöpfle, O. Kochetov, V. N. Kornoukhov, V. V. Kuzminov, M. Laubenstein, A. Lazzaro, M. Lindner, I. Lippi, A. Lubashevskiy, B. Lubsandorzhiev, G. Lutter, C. Macolino, B. Majorovits, W. Maneschg, M. Miloradovic, R. Mingazheva, M. Misiaszek, P. Moseev, I. Nemchenok, K. Panas, L. Pandola, K. Pelczar, L. Pertoldi, A. Pullia, C. Ransom, S. Riboldi, N. Rumyantseva, C. Sada, F. Salamida, C. Schmitt, B. Schneider, S. Schönert, A-K. Schütz, O. Schulz, B. Schwingenheuer, O. Selivanenko, E. Shevchik, M. Shirchenko, H. Simgen, A. Smolnikov, L. Stanco, L. Vanhoefer, A. A. Vasenko, A. Veresnikova, K. von Sturm, V. Wagner, A. Wegmann, T. Wester, C. Wiesinger, M. Wojcik, E. Yanovich, I. Zhitnikov, S. V. Zhukov, D. Zinatulina, A. Zschocke, A. J. Zsigmond, K. Zuber, and G. Zuzel. Improved limit on neutrinoless double-β decay of ^{76}Ge from gerda phase ii. *Phys. Rev. Lett.*, 120:132503, Mar 2018.

[3] B. Aharmim, S. N. Ahmed, A. E. Anthony, N. Barros, E. W. Beier, A. Bellerive, B. Beltran, M. Bergevin, S. D. Biller, K. Boudjemline, M. G. Boulay, B. Cai, Y. D. Chan, D. Chauhan, M. Chen, B. T. Cleveland, G. A. Cox, X. Dai, H. Deng, J. A. Detwiler, M. DiMarco, P. J. Doe, G. Doucas, P.-L. Drouin, F. A. Duncan, M. Dunford, E. D. Earle, S. R. Elliott, H. C. Evans, G. T. Ewan, J. Farine, H. Fergani, F. Fleurot, R. J. Ford, J. A. Formaggio, N. Gagnon, J. TM. Goon, K. Graham, E. Guillian, S. Habib, R. L. Hahn, A. L. Hallin, E. D. Hallman, P. J. Harvey, R. Hazama, W. J. Heintzelman, J. Heise, R. L. Helmer, A. Hime, C. Howard, M. Huang, P. Jagam, B. Jamieson, N. A. Jelley, M. Jerkins, K. J. Keeter, J. R. Klein, L. L. Kormos, M. Kos, C. Kraus, C. B. Krauss, A Kruger, T. Kutter, C. C. M. Kyba, R. Lange, J. Law, I. T. Lawson, K. T. Lesko, J. R. Leslie, J. C. Loach, R. MacLellan, S. Majerus, H. B. Mak, J. Maneira, R. Martin, N. McCauley, A. B. McDonald, S. R. McGee, M. L. Miller, B. Monreal, J. Monroe, B. G. Nickel, A. J. Noble, H. M. O'Keeffe, N. S. Oblath, R. W. Ollerhead, G. D. Orebi Gann, S. M. Oser, R. A. Ott, S. J. M. Peeters, A. W. P. Poon, G. Prior,

S. D. Reitzner, K. Rielage, B. C. Robertson, R. G. H. Robertson, R. C. Rosten, M. H. Schwendener, J. A. Secrest, S. R. Seibert, O. Simard, J. J. Simpson, P. Skensved, T. J. Sonley, L. C. Stonehill, G. Tešić, N. Tolich, T. Tsui, R. Van Berg, B. A. VanDevender, C. J. Virtue, H. Wan Chan Tseung, D. L. Wark, P. J. S. Watson, J. Wendland, N. West, J. F. Wilkerson, J. R. Wilson, J. M. Wouters, A. Wright, M. Yeh, F. Zhang, and K. Zuber. Combined analysis of all three phases of solar neutrino data from the sudbury neutrino observatory. *Phys. Rev. C*, 88:025501, Aug 2013.

[4] M. Aker, K. Altenmüller, M. Arenz, M. Babutzka, J. Barrett, S. Bauer, M. Beck, A. Beglarian, J. Behrens, T. Bergmann, U. Besserer, K. Blaum, F. Block, S. Bobien, K. Bokeloh, J. Bonn, B. Bornschein, L. Bornschein, H. Bouquet, T. Brunst, T. S. Caldwell, L. La Cascio, S. Chilingaryan, W. Choi, T. J. Corona, K. Debowski, M. Deffert, M. Descher, P. J. Doe, O. Dragoun, G. Drexlin, J. A. Dunmore, S. Dyba, F. Edzards, L. Eisenblätter, K. Eitel, E. Ellinger, R. Engel, S. Enomoto, M. Erhard, D. Eversheim, M. Fedkevych, A. Felden, S. Fischer, B. Flatt, J. A. Formaggio, F. M. Fränkle, G. B. Franklin, H. Frankrone, F. Friedel, D. Fuchs, A. Fulst, D. Furse, K. Gauda, H. Gemmeke, W. Gil, F. Glück, S. Görhardt, S. Groh, S. Grohmann, R. Grössle, R. Gumbsheimer, M. Ha Minh, M. Hackenjos, V. Hannen, F. Harms, J. Hartmann, N. Haußmann, F. Heizmann, K. Helbing, S. Hickford, D. Hilk, B. Hillen, D. Hillesheimer, D. Hinz, T. Höhn, B. Holzapfel, S. Holzmann, T. Houdy, M. A. Howe, A. Huber, T. M. James, A. Jansen, A. Kaboth, C. Karl, O. Kazachenko, J. Kellerer, N. Kernert, L. Kippenbrock, M. Kleesiek, M. Klein, C. Köhler, L. Köllenberger, A. Kopmann, M. Korzeczek, A. Kosmider, A. Kovalík, B. Krasch, M. Kraus, H. Krause, L. Kuckert, B. Kuffner, N. Kunka, T. Lasserre, T. L. Le, O. Lebeda, M. Leber, B. Lehnert, J. Letnev, F. Leven, S. Lichter, V. M. Lobashev, A. Lokhov, M. Machatschek, E. Malcherek, K. Müller, M. Mark, A. Marsteller, E. L. Martin, C. Melzer, A. Menshikov, S. Mertens, L. I. Minter, S. Mirz, B. Monreal, P. I. Morales Guzmán, K. Müller, U. Naumann, W. Ndeke, H. Neumann, S. Niemes, M. Noe, N. S. Oblath, H.-W. Ortjohann, A. Osipowicz, B. Ostrick, E. Otten, D. S. Parno, D. G. Phillips, P. Plischke, A. Pollithy, A. W. P. Poon, J. Pouryamout, M. Prall, F. Priester, M. Röllig, C. Röttele, P. C.-O. Ranitzsch, O. Rest, R. Rinderspacher, R. G. H. Robertson, C. Rodenbeck, P. Rohr, Ch. Roll, S. Rupp, M. Ryšavý, R. Sack, A. Saenz, P. Schäfer, L. Schimpf, K. Schlösser, M. Schlösser, L. Schlüter, H. Schön, K. Schönung, M. Schrank, B. Schulz, J. Schwarz, H. Seitz-Moskaliuk, W. Seller, V. Sibille, D. Siegmann, A. Skasyrskaya, M. Slezák, A. Špalek, F. Spanier, M. Steidl, N. Steinbrink, M. Sturm, M. Suesser, M. Sun, D. Tcherniakhovski, H. H. Telle, T. Thümmler, L. A. Thorne, N. Titov, I. Tkachev, N. Trost, K. Urban, D. Vénos, K. Valerius, B. A. VanDevender, R. Vianden, A. P. Vizcaya Hernández, B. L. Wall, S. Wüstling, M. Weber, C. Weinheimer, C. Weiss, S. Welte, J. Wendel, K. J. Wierman, J. F. Wilkerson, J. Wolf, W. Xu, Y.-R. Yen, M. Zacher, S. Zadorozhny, M. Zbořil, and G. Zeller. Improved upper limit on the neutrino mass from a direct kinematic method by katrin. *Phys. Rev. Lett.*, 123:221802, Nov 2019.

[5] C. Alduino, F. Alessandria, K. Alfonso, E. Andreotti, C. Arnaboldi, F. T. Avignone, O. Azzolini, M. Balata, I. Bandac, T. I. Banks, G. Bari, M. Barucci, J. W. Beeman, F. Bellini, G. Benato, A. Bersani, D. Biare, M. Biassoni, F. Bragazzi, A. Branca, C. Brofferio, A. Bryant, A. Buccheri, C. Bucci, C. Bulfon, A. Camacho, A. Caminata, L. Canonica, X. G. Cao, S. Capelli, M. Capodiferro, L. Cappelli, L. Cardani, M. Cariello, P. Carniti, M. Carrettoni, N. Casali, L. Cassina, R. Cereseto, G. Ceruti, A. Chiarini, D. Chiesa, N. Chott, M. Clemenza, D. Conventi, S. Copello, C. Cosmelli, O. Cremonesi, C. Crescentini, R. J. Creswick, J. S. Cushman, A. D'Addabbo, D. D'Aguanno, I. Dafinei, V. Datskov, C. J. Davis, F. Del Corso, S. Dell'Oro, M. M. Deninno, S. Di Domizio, M. L. Di Vacri, L. Di Paolo, A. Drobizhev, L. Ejzak, R. Faccini, D. Q. Fang, M. Faverzani, E. Ferri, F. Ferroni, E. Fiorini, M. A. Franceschi, S. J. Freedman, B. K. Fujikawa, R. Gaigher, A. Giachero, L. Gironi, A. Giuliani, L. Gladstone, J. Goett, P. Gorla, C. Gotti, C. Guandalini, M. Guerzoni, T. D. Gutierrez, E. E. Haller, K. Han, E. V. Hansen, K. M. Heeger, R. Hennings-Yeomans, K. P. Hickerson, H. Z. Huang, M. Iannone, L. Ioannucci, R. Kadel, G. Keppel, L. Kogler, Yu. G. Kolomensky, A. Leder, C. Ligi, K. E. Lim, X. Liu, Y. G. Ma, C. Maiano, M. Maino, L. Marini, M. Martinez, C. Martinez Amaya, R. H. Maruyama, Y. Mei, N. Moggi, S. Morganti, P. J. Mosteiro, S. S. Nagorny, T. Napolitano, M. Nastasi, S. Nisi, C. Nones, E. B. Norman, V. Novati, A. Nucciotti, I. Nutini, T. O'Donnell, M. Olcese, E. Olivieri, F. Orio, D. Orlandi, J. L. Ouellet, C. E. Pagliarone, M. Pallavicini, V. Palmieri, L. Pattavina, M. Pavan, M. Pedretti, R. Pedrotta, A. Pelosi, G. Pessina, V. Pettinacci, G. Piperno, C. Pira, S. Pirro, S. Pozzi, E. Previtali, F. Reindl, F. Rimondi, L. Risegari, C. Rosenfeld, C. Rossi, C. Rusconi, M. Sakai, E. Sala, C. Salvioni, S. Sangiorgio, D. Santone, D. Schaeffer, B. Schmidt, J. Schmidt, N. D. Scielzo, V. Singh, M. Sisti, A. R. Smith, F. Stivanello, L. Taffarello, L. Tatananni, M. Tenconi, F. Terranova, M. Tessaro, C. Tomei, G. Ventura, M. Vignati, S. L. Wagaarachchi, J. Wallig, B. S. Wang, H. W. Wang, B. Welliver, J. Wilson, K. Wilson, L. A. Winslow, T. Wise, L. Zanotti, C. Zarra, G. Q. Zhang, B. X. Zhu, S. Zimmermann, and S. Zucchelli. First results from cuore: A search for lepton number violation via $0\nu\beta\beta$ decay of ^{130}Te. *Phys. Rev. Lett.*, 120:132501, Mar 2018.

[6] S. I. Alvis, I. J. Arnquist, F. T. Avignone, A. S. Barabash, C. J. Barton, F. E. Bertrand, V. Brudanin, M. Busch, M. Buuck, T. S. Caldwell, Y-D. Chan, C. D. Christofferson, P.-H. Chu, C. Cuesta, J. A. Detwiler, C. Dunagan, Yu. Efremenko, H. Ejiri, S. R. Elliott, T. Gilliss, G. K. Giovanetti, M. P. Green, J. Gruszko, I. S. Guinn, V. E. Guiseppe, C. R. Haufe, L. Hehn, R. Henning, E. W. Hoppe, M. A. Howe, S. I. Konovalov, R. T. Kouzes, A. M. Lopez, R. D. Martin, R. Massarczyk, S. J. Meijer, S. Mertens, J. Myslik, C. O'Shaughnessy, G. Othman, W. Pettus, A. W. P. Poon, D. C. Radford, J. Rager, A. L. Reine, K. Rielage, R. G. H. Robertson, N. W. Ruof, B. Shanks, M. Shirchenko, A. M. Suriano, D. Tedeschi, R. L. Varner, S. Vasilyev, K. Vorren, B. R. White, J. F. Wilkerson, C. Wiseman, W. Xu, E. Yakushev, C.-H. Yu, V. Yumatov, I. Zhitnikov, and B. X. Zhu. First limit on the direct detection of lightly ionizing particles for electric

charge as low as $e/1000$ with the majorana demonstrator. *Phys. Rev. Lett.*, 120:211804, May 2018.

[7] V. N. Aseev, A. I. Belesev, A. I. Berlev, E. V. Geraskin, A. A. Golubev, N. A. Likhovid, V. M. Lobashev, A. A. Nozik, V. S. Pantuev, V. I. Parfenov, A. K. Skasyrskaya, F. V. Tkachov, and S. V. Zadorozhny. Upper limit on the electron antineutrino mass from the troitsk experiment. *Phys. Rev. D*, 84:112003, Dec 2011.

[8] V.N. Aseev et al. Energy loss of 18 kev electrons in gaseous t and quench condensed d films. *Eur. Phys. J. D*, 10:39–52, March 2000.

[9] D. M. Asner, R. F. Bradley, L. de Viveiros, P. J. Doe, J. L. Fernandes, M. Fertl, E. C. Finn, J. A. Formaggio, D. Furse, A. M. Jones, J. N. Kofron, B. H. LaRoque, M. Leber, E. L. McBride, M. L. Miller, P. Mohanmurthy, B. Monreal, N. S. Oblath, R. G. H. Robertson, L. J Rosenberg, G. Rybka, D. Rysewyk, M. G. Sternberg, J. R. Tedeschi, T. Thümmler, B. A. VanDevender, and N. L. Woods. Single-electron detection and spectroscopy via relativistic cyclotron radiation. *Phys. Rev. Lett.*, 114:162501, Apr 2015.

[10] Karl-Erik Bergkvist. A high-luminosity, high-resolution study of the end-point behaviour of the tritium beta-spectrum (i). basic experimental procedure and analysis with regard to neutrino mass and neutrino degeneracy. *Nuclear Physics B*, 39:317 – 370, 1972.

[11] Karl-Erik Bergkvist. A high-luminosity, high-resolution study of the end-point behaviour of the tritium beta-spectrum (ii). the end-point energy of the spectrum. comparison of the experimental axial-vector matrix element with predictions based on pcac. *Nuclear Physics B*, 39:371 – 406, 1972.

[12] J Chadwick. Intensitätsverteilung im magnetischen Spectrum der β-Strahlen von radium B + C. *Verhandl. Dtsc. Phys. Ges.*, 16:383, 1914.

[13] Bruce T. Cleveland, Timothy Daily, Jr. Raymond Davis, James R. Distel, Kenneth Lande, C. K. Lee, Paul S. Wildenhain, and Jack Ullman. Measurement of the solar electron neutrino flux with the homestake chlorine detector. *The Astrophysical Journal*, 496(1):505–526, mar 1998.

[14] Vénos D., Sentkerestiová J., Dragoun O., Slezák M., Ryšavý M., and Špalek A. Properties of 83mkr conversion electrons and their use in the KATRIN experiment. *Journal of Instrumentation*, 13(02):T02012–T02012, feb 2018.

[15] G. Danby, J-M. Gaillard, K. Goulianos, L. M. Lederman, N. Mistry, M. Schwartz, and J. Steinberger. Observation of high-energy neutrino reactions and the existence of two kinds of neutrinos. *Phys. Rev. Lett.*, 9:36–44, Jul 1962.

[16] Robinson E.L. *Data Analysis for Scientists and Engineers.* Princeton University Press, 2016.

[17] C. D. Ellis and W. A. Wooster. The Average Energy of Disintegration of Radium E. *Proceedings of the Royal Society of London Series A*, 117(776):109–123, December 1927.

[18] A Ashtari Esfahani, S Böser, N Buzinsky, R Cervantes, C Claessens, L de Viveiros, M Fertl, J A Formaggio, L Gladstone, M Guigue, K M Heeger, J Johnston, A M Jones, K Kazkaz, B H LaRoque, A Lindman, E Machado, B Monreal, E C Morrison, J A Nikkel, E Novitski, N S Oblath, W Pettus, R G H Robertson, G Rybka, L Saldaña, V Sibille, M Schram, P L Slocum, Y-H Sun, T Thümmler, B A VanDevender, T E Weiss, T Wendler, and E Zayas. Cyclotron radiation emission spectroscopy signal classification with machine learning in project 8. *New Journal of Physics*, 22(3):033004, mar 2020.

[19] A. Ashtari Esfahani et al. Electron radiated power in cyclotron radiation emission spectroscopy experiments. *Phys. Rev. C*, 99:055501, May 2019.

[20] A. Ashtari Esfahani et al. Locust: C++ software for simulation of RF detection. *New Journal of Physics*, 21(11):113051, nov 2019.

[21] Ali Ashtari Esfahani, David M Asner, Sebastian Böser, Raphael Cervantes, Christine Claessens, Luiz de Viveiros, Peter J Doe, Shepard Doeleman, Justin L Fernandes, Martin Fertl, Erin C Finn, Joseph A Formaggio, Daniel Furse, Mathieu Guigue, Karsten M Heeger, A Mark Jones, Kareem Kazkaz, Jared A Kofron, Callum Lamb, Benjamin H LaRoque, Eric Machado, Elizabeth L McBride, Michael L Miller, Benjamin Monreal, Prajwal Mohanmurthy, James A Nikkel, Noah S Oblath, Walter C Pettus, R G Hamish Robertson, Leslie J Rosenberg, Gray Rybka, Devyn Rysewyk, Luis Saldaña, Penny L Slocum, Matthew G Sternberg, Jonathan R Tedeschi, Thomas Thümmler, Brent A VanDevender, Laura E Vertatschitsch, Megan Wachtendonk, Jonathan Weintroub, Natasha L Woods, André Young, and Evan M Zayas. Determining the neutrino mass with cyclotron radiation emission spectroscopy—project 8. *Journal of Physics G: Nuclear and Particle Physics*, 44(5):054004, mar 2017.

[22] Low Noise Factory. Lnf-lnc2240wa s/n 010: 22-40 ghz cryogenic low noiseamplifier. *Product data sheet.*, 2014.

[23] R. Fitzpatrick. *Introduction to Plasma Physics.* CRC Press, 2014.

[24] Y. Fukuda, T. Hayakawa, E. Ichihara, K. Inoue, K. Ishihara, H. Ishino, Y. Itow, T. Kajita, J. Kameda, S. Kasuga, K. Kobayashi, Y. Kobayashi, Y. Koshio, M. Miura, M. Nakahata, S. Nakayama, A. Okada, K. Okumura, N. Sakurai, M. Shiozawa, Y. Suzuki, Y. Takeuchi, Y. Totsuka, S. Yamada, M. Earl, A. Habig, E. Kearns, M. D. Messier, K. Scholberg, J. L. Stone, L. R. Sulak, C. W. Walter, M. Goldhaber, T. Barszczxak, D. Casper, W. Gajewski, P. G. Halverson, J. Hsu, W. R. Kropp, L. R. Price, F. Reines, M. Smy, H. W. Sobel, M. R. Vagins, K. S. Ganezer, W. E. Keig, R. W. Ellsworth, S. Tasaka, J. W. Flanagan, A. Kibayashi, J. G. Learned, S. Matsuno, V. J. Stenger, D. Takemori, T. Ishii, J. Kanzaki, T. Kobayashi, S. Mine, K. Nakamura, K. Nishikawa, Y. Oyama, A. Sakai, M. Sakuda, O. Sasaki, S. Echigo, M. Kohama, A. T. Suzuki, T. J. Haines, E. Blaufuss, B. K. Kim, R. Sanford, R. Svoboda, M. L. Chen, Z. Conner, J. A. Goodman, G. W. Sullivan, J. Hill, C. K. Jung, K. Martens, C. Mauger, C. McGrew, E. Sharkey, B. Viren, C. Yanagisawa, W. Doki, K. Miyano, H. Okazawa, C. Saji, M. Takahata, Y. Nagashima, M. Takita, T. Yamaguchi, M. Yoshida, S. B. Kim, M. Etoh, K. Fujita, A. Hasegawa, T. Hasegawa, S. Hatakeyama, T. Iwamoto, M. Koga, T. Maruyama, H. Ogawa, J. Shirai, A. Suzuki, F. Tsushima, M. Koshiba, M. Nemoto, K. Nishijima, T. Futagami, Y. Hayato, Y. Kanaya, K. Kaneyuki, Y. Watanabe, D. Kielczewska, R. A. Doyle, J. S. George, A. L. Stachyra, L. L. Wai, R. J. Wilkes, and K. K. Young. Evidence for oscillation of atmospheric neutrinos. *Phys. Rev. Lett.*, 81:1562–1567, Aug 1998.

[25] A. Gando, Y. Gando, T. Hachiya, A. Hayashi, S. Hayashida, H. Ikeda, K. Inoue, K. Ishidoshiro, Y. Karino, M. Koga, S. Matsuda, T. Mitsui, K. Nakamura, S. Obara, T. Oura, H. Ozaki, I. Shimizu, Y. Shirahata, J. Shirai, A. Suzuki, T. Takai, K. Tamae, Y. Teraoka, K. Ueshima, H. Watanabe, A. Kozlov, Y. Takemoto, S. Yoshida, K. Fushimi, T. I. Banks, B. E. Berger, B. K. Fujikawa, T. O'Donnell, L. A. Winslow, Y. Efremenko, H. J. Karwowski, D. M. Markoff, W. Tornow, J. A. Detwiler, S. Enomoto, and M. P. Decowski. Search for majorana neutrinos near the inverted mass hierarchy region with kamland-zen. *Phys. Rev. Lett.*, 117:082503, Aug 2016.

[26] L. Gastaldo et al. The electron capture in 163ho experiment – echo. *The European Physical Journal Special Topics*, 226:1623–1694, June 2017.

[27] A. Giachero, B.K. Alpert, D.T. Becker, D.A. Bennett, M. Biasotti, C. Brofferio, V. Ceriale, G. Ceruti, D. Corsini, P.K. Day, M. De Gerone, R. Dressler, M. Faverzani, E. Ferri, J.W. Fowler, E. Fumagalli, G. Gallucci, J.D. Gard, F. Gatti, J.P. Hays-Wehle, S. Heinitz, G.C. Hilton, U. Köster, M. Lusignoli, J.A.B. Mates, S. Nisi, A. Nucciotti, A. Orlando, L. Parodi, G. Pessina, G. Pizzigoni, A. Puiu, S. Ragazzi, C.D. Reintsema, M. Ribeiro Gomes, D.R. Schmidt, D. Schumann, F. Siccardi, M. Sisti, D.S. Swetz, F. Terranova, J.N. Ullom, and L.R. Vale. Measuring the electron neutrino mass with improved sensitivity: the HOLMES experiment. *Journal of Instrumentation*, 12(02):C02046–C02046, feb 2017.

[28] R. A. Holmwood and R. Glang. Resistivity and temperature coefficient of pure molybdenum. *Journal of Chemical & Engineering Data*, 10(2):162–163, 1965.

[29] John David Jackson. *Classical electrodynamics*. Wiley, New York, NY, 3rd ed. edition, 1999.

[30] Mohan V. Jacob, Janina E. Mazierska, Dimitri O. Ledenyov, and Jerzy Krupka. Microwave characterisation of CaF2 at cryogenic temperatures using a dielectric resonator technique. *Journal of the European Ceramic Society*, 23, 2003.

[31] Kareem Kazkaz and Nathan Woollett. Concept for testing noble element atomic energy levels and photoelectric cross sections using cyclotron radiation emission spectroscopy. 2019.

[32] K. Kodama, N. Ushida, C. Andreopoulos, N. Saoulidou, G. Tzanakos, P. Yager, B. Baller, D. Boehnlein, W. Freeman, B. Lundberg, J. Morfin, R. Rameika, J.C. Yun, J.S. Song, C.S. Yoon, S.H. Chung, P. Berghaus, M. Kubantsev, N.W. Reay, R. Sidwell, N. Stanton, S. Yoshida, S. Aoki, T. Hara, J.T. Rhee, D. Ciampa, C. Erickson, M. Graham, K. Heller, R. Rusack, R. Schwienhorst, J. Sielaff, J. Trammell, J. Wilcox, K. Hoshino, H. Jiko, M. Miyanishi, M. Komatsu, M. Nakamura, T. Nakano, K. Niwa, N. Nonaka, K. Okada, O. Sato, T. Akdogan, V. Paolone, C. Rosenfeld, A. Kulik, T. Kafka, W. Oliver, T. Patzak, and J. Schneps. Observation of tau neutrino interactions. *Physics Letters B*, 504(3):218 – 224, 2001.

[33] Jared Kofron. *A novel method for electron energy measurement: Cyclotron Radiation Emission Spectroscopy*. University of Washington, 2015.

[34] Ch Kraus, B. Bornschein, L. Bornschein, Flatt Bonn, J., Kovalik B., Ostrick A., Otten B., Schall E. W., Th J. P., Thümmler, and Ch Weinheimer. Final results from phase ii of the mainz neutrino mass searchin tritium βdecay. *The European Physical Journal C - Particles and Fields*, 40:447–468, April 2005.

[35] Woodcraft A. L. and Gray A. A low temperature thermal conductivity database. *CP1185,Low Temperature Detectors LTD 13, Proceedings of the 13th International Workshop*, 2009.

[36] W. Orthmann L. Meitner. Über eine absolute Bestimmung der Energie der primären beta-Strahlen von Radium E. *Zeitschrift für Physik*, 60(776):143–155, march 1930.

[37] Luca Lista. Practical statistics for particle physicists, 2016.

[38] Luca Lista. Ubc database, 2016.

[39] A. V. Lokhov and F. V. Tkachov. Confidence intervals with a priori parameter bounds. *Phys. Part. Nuclei.*, 46:347–365, May 2015.

[40] Thomas J. Loredo and Donald Q. Lamb. Bayesian analysis of neutrinos observed from supernova sn 1987a. *Phys. Rev. D*, 65:063002, Feb 2002.

[41] Arthur Loureiro, Andrei Cuceu, Filipe B. Abdalla, Bruno Moraes, Lorne Whiteway, Michael McLeod, Sreekumar T. Balan, Ofer Lahav, Aurélien Benoit-Lévy, Marc Manera, Richard P. Rollins, and Henrique S. Xavier. Upper bound of neutrino masses from combined cosmological observations and particle physics experiments. *Phys. Rev. Lett.*, 123:081301, Aug 2019.

[42] V Lyubimov, E Novikov, V Nozik, E Tret'yakov, V Kozik, and N Myasoedov. Estimation of the neutrino rest mass from measurements of the tritium. beta. spectrum. *Sov. Phys. - JETP (Engl. Transl.); (United States)*, 54, 10 1981.

[43] Tanabashi M., Grp P.D., Hagiwara K., Hikasa K., Nakamura K., Sumino Y., Takahashi F., Tanaka J., Agashe K., Aielli G., Amsler C., Antonelli M., Asner D.M., Baer H., Banerjee S., Barnett R.M., Basaglia T., Bauer C., and Beatty J. Review of particle physics: Particle data group. *Physical Review D*, 98, 08 2018.

[44] Benjamin Monreal and Joseph A. Formaggio. Relativistic cyclotron radiation detection of tritium decay electrons as a new technique for measuring the neutrino mass. *Phys. Rev. D*, 80:051301, Sep 2009.

[45] Wandkowsky N. *Study of background and transmission properties of the KATRIN spectrometers.* KIT, Karlsruhe, 2013.

[46] Theodore G. Northrop. *The Adiabatic Motion of Particles.* Interscience Publishers, 1963.

[47] E W Otten and C Weinheimer. Neutrino mass limit from tritium β decay. *Reports on Progress in Physics*, 71(8):086201, jul 2008.

[48] A. Picard et al. Precision measurement of the conversion electron spectrum of83mkr with a solenoid retarding spectrometer. *Zeitschrift für Physik A Hadrons and Nuclei*, 342(1):71–78, Mar 1992.

[49] L C Pitchford. GEC plasma data exchange project. *Journal of Physics D: Applied Physics*, 46(33):330301, aug 2013.

[50] D.M. Pozar. *Microwave Engineering.* Wiley, 2004.

[51] F. Reines and C. L. Cowan. Detection of the free neutrino. *Phys. Rev.*, 92:830–831, Nov 1953.

[52] F. Reines and C. L. Cowan. The neutrino. *Nature*, 178:446–449, Sep 1956.

[53] Robertson R.G.H. and Knapp D.A. Direct measurements of neutrino mass. *Annual Review of Nuclear and Particle Science*, 38(1):185–215, 1988.

[54] Robertson R.G.H. and Venkatapathy V. Shakeup and shakeoff satellite structure in the electron spectrum of ^{83m}kr. 2020.

[55] Kirby R.K., Touloukian Y.S., Taylor E.R., and Lee T.Y.R. *Thermophysical properties of matter - the TPRC data series. Volume 13. Thermal expansion - nonmetallic solids. (Reannouncement). Data book.* 1 1977.

[56] R. G. H. Robertson, T. J. Bowles, G. J. Stephenson, D. L. Wark, J. F. Wilkerson, and D. A. Knapp. Limit on ν

Appendix A

ELECTRON'S MOTION IN A NON-UNIFORM MAGNETIC FIELD

In this appendix we present the solution to electron's motion in a non-uniform magnetic field. Here we assume that the range of changes in the magnetic field, L, is much larger than the cyclotron radius of the electron, $\rho_c = \frac{\gamma m v_0}{e B_0}$. To keep track of the term's magnitude, we first perform a transformation

$$\begin{aligned} \tilde{\mathbf{B}} &= \mathbf{B}(\mathbf{r})/B_0, \\ \tilde{t} &= v_0 t/L, \\ \tilde{\mathbf{r}} &= \mathbf{r}/L, \end{aligned} \tag{A.1}$$

where v_0 is the initial velocity of electron and B_0 is the value of the magnetic field strength averaged over a cyclotron period. With this transformation, the Lorentz force in Eq. 3.1 can be written as

$$\frac{d^2\tilde{\mathbf{r}}}{d\tilde{t}^2} = \frac{L}{\rho_c}\frac{d\tilde{\mathbf{r}}}{d\tilde{t}} \times \tilde{\mathbf{B}}(\tilde{\mathbf{r}}). \tag{A.2}$$

Following Eq. 3.3 the normalized gyration radius and velocity can be written as

$$\begin{aligned} \tilde{\mathbf{r}} &= \tilde{\mathbf{R}}(t) + \tilde{\boldsymbol{\rho}}(\tilde{\mathbf{R}}, \tilde{\mathbf{U}}, t, \phi), \\ \tilde{\mathbf{v}} &= \tilde{\mathbf{U}}(t) + \tilde{\mathbf{u}}(\tilde{\mathbf{R}}, \tilde{\mathbf{U}}, t, \phi). \end{aligned} \tag{A.3}$$

The periodicity condition (Eq. A.4) is also valid for the normalized gyration radius and velocity,

$$\langle \tilde{\mathbf{u}} \rangle = \langle \tilde{\boldsymbol{\rho}} \rangle = 0. \tag{A.4}$$

We can now expand normalized functions in Eq. (A.3) in terms of $\epsilon \equiv \rho_c/L$,

$$\begin{aligned}
\tilde{\boldsymbol{R}} &= \tilde{\boldsymbol{R}_{\mathbf{0}}}(t) + \tilde{\boldsymbol{R}_{\mathbf{1}}}(t) + \mathcal{O}(\epsilon^2) \\
\tilde{\boldsymbol{\rho}} &= \tilde{\boldsymbol{\rho}_{\mathbf{0}}}(\tilde{\mathbf{R}}, \tilde{\mathbf{U}}, t, \phi) + \tilde{\boldsymbol{\rho}_{\mathbf{1}}}(\tilde{\mathbf{R}}, \tilde{\mathbf{U}}, t, \phi) + \mathcal{O}(\epsilon^2) \\
\tilde{\boldsymbol{U}} &= \tilde{\boldsymbol{U}_{\mathbf{0}}}(t) + \tilde{\boldsymbol{U}_{\mathbf{1}}}(t) + \mathcal{O}(\epsilon^2) \\
\tilde{\boldsymbol{u}} &= \tilde{\boldsymbol{u}_{\mathbf{0}}}(\tilde{\mathbf{R}}, \tilde{\mathbf{U}}, t, \phi) + \tilde{\boldsymbol{u}_{\mathbf{1}}}(\tilde{\mathbf{R}}, \tilde{\mathbf{U}}, t, \phi) + \mathcal{O}(\epsilon^2).
\end{aligned} \tag{A.5}$$

From the definition of $\tilde{\mathbf{v}}$ and the periodicity condition we get

$$\frac{d\tilde{\boldsymbol{R}_{\boldsymbol{n}}}}{d\tilde{t}} = \tilde{\boldsymbol{U}_{\boldsymbol{n}}}, \tag{A.6}$$

and therefore,

$$\frac{d\tilde{\boldsymbol{\rho}_{\boldsymbol{n}}}}{d\tilde{t}} = \tilde{\boldsymbol{u}_{\boldsymbol{n}}}. \tag{A.7}$$

To rewrite similar expansion for the angular frequency of cyclotron motion, we note that $\omega_c \sim 2\pi/\tilde{T} \sim 2\pi L/\rho_c \sim 1/\epsilon$. Hence

$$\frac{d\phi}{d\tilde{t}} = \frac{1}{\epsilon}\omega_{-1}(\tilde{\mathbf{R}}, \tilde{\mathbf{U}}, \tilde{t}) + \omega_0(\tilde{\mathbf{R}}, \tilde{\mathbf{U}}, \tilde{t}) + \mathcal{O}(\epsilon). \tag{A.8}$$

We can now solve Eq. (A.2) for terms with similar ϵ order. For the lowest order ($\mathcal{O}(1/\epsilon)$) we get

$$\omega_{-1}\frac{\partial \tilde{\mathbf{u}}_0}{\partial \phi} = \tilde{\mathbf{u}}_0 \times \tilde{\mathbf{B}} + \tilde{\mathbf{U}}_0 \times \tilde{\mathbf{B}}. \tag{A.9}$$

Applying the continuity condition results in

$$\tilde{\mathbf{U}}_0 \times \tilde{\mathbf{B}} = 0. \tag{A.10}$$

This means that the 0^{th} order velocity is parallel to field ($\tilde{\mathbf{U}}_0 = \tilde{U}_{0\|}\tilde{\mathbf{b}}$). However this term is undetermined at this order. Subtracting Eq. (A.10) from (A.9) gives

$$\omega_{-1}\frac{\partial \tilde{\mathbf{u}}_0}{\partial \phi} = \tilde{\mathbf{u}}_0 \times \tilde{\mathbf{B}}. \tag{A.11}$$

The solution to this equation can be found by constructing a standard basis ($\mathbf{e}_1, \mathbf{e}_2, \tilde{\mathbf{b}} \equiv \tilde{\mathbf{B}}/\tilde{B}$),

$$\tilde{\mathbf{u}}_0 = \mathbf{c} + \tilde{u}_\perp \left[\mathbf{e}_1 \sin(\tilde{B}\phi/\omega_{-1}) + \mathbf{e}_2 \cos(\tilde{B}\phi/\omega_{-1})\right]. \tag{A.12}$$

The periodicity condition requires $\omega_{-1}(\tilde{\mathbf{R}}, \tilde{\mathbf{U}}, \tilde{t}) = \tilde{B}$ and $c = 0$. Also from the normalization we have $\tilde{u}_{\perp} = \frac{v_0}{v_0} = 1$. Therefore the phase evolution can be found to the first order in ϵ by solving Eq. (A.8),

$$\begin{aligned} \phi(\tilde{t}) &= \frac{\tilde{B}}{\epsilon}\tilde{t} + \phi_0 \\ &= \frac{eB(t)}{\gamma m}t + \phi_0 \\ &= \Omega_c t + \phi_0. \end{aligned} \tag{A.13}$$

To find ρ we use the lowest order in Eq. (A.7),

$$\frac{1}{\epsilon}\omega_{-1}\frac{\partial \tilde{\boldsymbol{\rho}}_{\mathbf{0}}}{\partial \phi} = \tilde{\boldsymbol{u}}_{\mathbf{0}}. \tag{A.14}$$

Integrating over Eq. (A.14) gives,

$$\tilde{\boldsymbol{\rho}}_{\mathbf{0}} = \tilde{\rho}_c \left[-\mathbf{e}_1 \cos(\Omega_c t + \phi_0) + \mathbf{e}_2 \sin(\Omega_c t + \phi_0)\right], \tag{A.15}$$

where $\tilde{\rho}_c = \frac{\epsilon}{\tilde{B}}$. Note that periodicity condition requires no constant in the solution.

These terms can be rewritten in the unnormalized coordinate,

$$\begin{aligned} \boldsymbol{\rho}_{\mathbf{0}} &= \rho_c \left[-\mathbf{e}_1 \cos(\Omega_c t + \phi_0) + \mathbf{e}_2 \sin(\Omega_c t + \phi_0)\right] \\ \mathbf{u}_0 &= v_0 \left[\mathbf{e}_1 \sin(\Omega_c t + \phi_0) + \mathbf{e}_2 \cos(\Omega_c t + \phi_0)\right], \end{aligned} \tag{A.16}$$

in which $\rho_c \Omega_c = v_0$.

Now let us consider the second order set of terms in ϵ,

$$\frac{d\boldsymbol{U}_0}{d\tilde{t}} + \frac{d\boldsymbol{u}_0}{d\tilde{t}} + \omega_0 \frac{d\boldsymbol{u}_0}{d\phi} + \omega_{-1}\frac{d\boldsymbol{u}_1}{d\phi} = \frac{1}{\epsilon}\left[(\boldsymbol{U}_1 + \boldsymbol{u}_1) \times \tilde{\boldsymbol{B}} + (\boldsymbol{U}_0 + \boldsymbol{u}_0) \times (\tilde{\boldsymbol{\rho}}_0 \cdot \boldsymbol{\nabla})\tilde{\boldsymbol{B}}\right] \tag{A.17}$$

Applying the periodicity condition reduce Eq. (A.17) to,

$$\frac{d\tilde{\boldsymbol{U}}_0}{d\tilde{t}} = \frac{1}{\epsilon}\left[\tilde{\boldsymbol{U}}_1 \times \tilde{\boldsymbol{B}} + \langle \tilde{\boldsymbol{u}}_0 \times (\tilde{\boldsymbol{\rho}}_0 \cdot \boldsymbol{\nabla})\tilde{\boldsymbol{B}}\rangle\right] \tag{A.18}$$

Replacing the 0^{th} order solution from Eq. (A.15) and Eq. (A.12), we can show

$$\langle \tilde{\boldsymbol{u}}_0 \times (\tilde{\boldsymbol{\rho}}_0 \cdot \boldsymbol{\nabla})\tilde{\boldsymbol{B}}\rangle = \frac{\tilde{\rho}_c}{2}\left[\mathbf{e}_1 \times (\mathbf{e}_2 \cdot \boldsymbol{\nabla})\tilde{\boldsymbol{B}} - \mathbf{e}_2 \times (\mathbf{e}_1 \cdot \boldsymbol{\nabla})\tilde{\boldsymbol{B}}\right]. \tag{A.19}$$

Calculating the first term in this equation gives

$$\begin{aligned} \mathbf{e}_1 \times (\mathbf{e}_2 \cdot \boldsymbol{\nabla})\tilde{\boldsymbol{B}} &= (\mathbf{e}_2 \times \tilde{\mathbf{b}}) \times (\mathbf{e}_2 \cdot \boldsymbol{\nabla})\tilde{\boldsymbol{B}} \\ &= \tilde{\mathbf{b}}(\mathbf{e}_2 \cdot (\mathbf{e}_2 \cdot \boldsymbol{\nabla})\tilde{\boldsymbol{B}}) - \mathbf{e}_2(\tilde{\mathbf{b}} \cdot (\mathbf{e}_2 \cdot \boldsymbol{\nabla})\tilde{\boldsymbol{B}}) \\ &= \tilde{\mathbf{b}}(\mathbf{e}_2 \cdot (\mathbf{e}_2 \cdot \boldsymbol{\nabla})\tilde{\boldsymbol{B}}) - \boldsymbol{e}_2(\boldsymbol{e}_2 \cdot \boldsymbol{\nabla}\tilde{B}). \end{aligned} \tag{A.20}$$

In which we make use of

$$\begin{aligned} \tilde{\mathbf{b}} \cdot (\mathbf{e}_2 \cdot \boldsymbol{\nabla})\tilde{\boldsymbol{B}} &= \tilde{\mathbf{b}} \cdot (\mathbf{e}_2 \cdot \boldsymbol{\nabla})(\tilde{B}\tilde{\mathbf{b}}) \\ &= \tilde{B}\left(\tilde{\mathbf{b}} \cdot (\mathbf{e}_2 \cdot \boldsymbol{\nabla}\tilde{\boldsymbol{b}})\right) + \tilde{\mathbf{b}} \cdot (\mathbf{e}_2 \cdot \boldsymbol{\nabla}\tilde{B}\tilde{\boldsymbol{b}}) \\ &= \frac{\tilde{B}}{2}\boldsymbol{e}_2 \cdot \boldsymbol{\nabla}(\tilde{\boldsymbol{b}} \cdot \tilde{\boldsymbol{b}}) + (\mathbf{e}_2 \cdot \boldsymbol{\nabla}\tilde{B})(\tilde{\boldsymbol{b}} \cdot \tilde{\boldsymbol{b}}) \\ &= \mathbf{e}_2 \cdot \boldsymbol{\nabla}\tilde{B}, \end{aligned} \tag{A.21}$$

Since $\tilde{\boldsymbol{b}} \cdot \tilde{\boldsymbol{b}} = 1$. The same line of reasoning can be made to show

$$\mathbf{e}_2 \times (\mathbf{e}_1 \cdot \boldsymbol{\nabla})\tilde{\boldsymbol{B}} = -\tilde{\mathbf{b}}(\mathbf{e}_1 \cdot (\mathbf{e}_1 \cdot \boldsymbol{\nabla})\tilde{\boldsymbol{B}}) + \boldsymbol{e}_1(\boldsymbol{e}_1 \cdot \boldsymbol{\nabla}\tilde{B}). \tag{A.22}$$

Adding the Maxwell equation for magnetic field's divergence,

$$\boldsymbol{\nabla} \cdot \tilde{\boldsymbol{B}} = (\boldsymbol{e}_1 \cdot \boldsymbol{\nabla})\tilde{\boldsymbol{B}} + (\boldsymbol{e}_2 \cdot \boldsymbol{\nabla})\tilde{\boldsymbol{B}} + (\tilde{\boldsymbol{b}} \cdot \boldsymbol{\nabla})\tilde{\boldsymbol{B}} = 0, \tag{A.23}$$

results in

$$\begin{aligned} \frac{2}{\tilde{\rho}_c}\langle \tilde{\boldsymbol{u}}_0 \times (\tilde{\boldsymbol{\rho}}_0 \cdot \boldsymbol{\nabla})\tilde{\boldsymbol{B}} \rangle &= \tilde{\mathbf{b}}\left(\mathbf{e}_1 \cdot (\mathbf{e}_1 \cdot \boldsymbol{\nabla})\tilde{\boldsymbol{B}} + \mathbf{e}_2 \cdot (\mathbf{e}_2 \cdot \boldsymbol{\nabla})\tilde{\boldsymbol{B}}\right) - \boldsymbol{e}_1(\boldsymbol{e}_1 \cdot \boldsymbol{\nabla}\tilde{B}) - \boldsymbol{e}_2(\boldsymbol{e}_2 \cdot \boldsymbol{\nabla}\tilde{B}) \\ &= \tilde{\mathbf{b}}\left(-\tilde{\mathbf{b}} \cdot (\tilde{\mathbf{b}} \cdot \boldsymbol{\nabla})\tilde{\boldsymbol{B}}\right) - \boldsymbol{e}_1(\boldsymbol{e}_1 \cdot \boldsymbol{\nabla}\tilde{B}) - \boldsymbol{e}_2(\boldsymbol{e}_2 \cdot \boldsymbol{\nabla}\tilde{B}) \\ &= -\tilde{\mathbf{b}}(\tilde{\mathbf{b}} \cdot \frac{\partial \tilde{\boldsymbol{B}}}{\partial s}) - \boldsymbol{e}_1(\boldsymbol{e}_1 \cdot \boldsymbol{\nabla}\tilde{B}) - \boldsymbol{e}_2(\boldsymbol{e}_2 \cdot \boldsymbol{\nabla}\tilde{B}) \\ &= -\tilde{\mathbf{b}}\frac{\partial \tilde{B}}{\partial s} - \boldsymbol{e}_1(\boldsymbol{e}_1 \cdot \boldsymbol{\nabla}\tilde{B}) - \boldsymbol{e}_2(\boldsymbol{e}_2 \cdot \boldsymbol{\nabla}\tilde{B}) \\ &= -\boldsymbol{\nabla}\tilde{B}. \end{aligned} \tag{A.24}$$

Hence the second order equation of motion can be written as,

$$\frac{d\tilde{\boldsymbol{U}}_0}{d\tilde{t}} = \frac{1}{\epsilon}\left[\tilde{\boldsymbol{U}}_1 \times \tilde{\boldsymbol{B}} - \frac{\tilde{\rho}_c}{2}\boldsymbol{\nabla}\tilde{B}\right]. \tag{A.25}$$

Replacing the value of $\tilde{\rho}_c$ and going back to the unnormalized quantities gives the equation for the secular motion,

$$\frac{d\boldsymbol{U}_0}{dt} = \frac{e}{\gamma m}\,\boldsymbol{U}_1 \times \boldsymbol{B} - \frac{\mu}{\gamma m}\,\boldsymbol{\nabla} B. \tag{A.26}$$

Where the magnetic moment vector is defined as

$$\boldsymbol{\mu} = \frac{m\gamma^2 v_0^2}{2B}\boldsymbol{b} \tag{A.27}$$

It can be shown that magnetic moment is a constant of motion [46]. Utilizing the fact that $\boldsymbol{U}_0$ is parallel to the magnetic field, we can solve Eq. (A.26). For the velocity component parallel to the field we get

$$\gamma m\,\frac{dU_0}{dt} = -\boldsymbol{\mu} \cdot \boldsymbol{\nabla} B, \tag{A.28}$$

in which we make use of the fact that $\boldsymbol{b} \cdot d\boldsymbol{b}/dt = 0$. This equation illustrates that there is an effective force exerted to the electron via the gradients in magnetic field. This is the basic force which explains the fundamentals of magnetic trapping. The component of velocity perpendicular to the field can also be found from Eq. (A.26),

$$\boldsymbol{U}_{1\perp} = \frac{\boldsymbol{b}}{\Omega_c}\left[\frac{d\boldsymbol{U}_0}{dt} + \frac{\mu}{\gamma m}\,\boldsymbol{\nabla} B\right] \tag{A.29}$$

Replacing the value of $\boldsymbol{U}_0$ results in,

$$\boldsymbol{U}_{1\perp} = \frac{\mu}{\gamma m \Omega_c}\boldsymbol{b} \times \boldsymbol{\nabla} B + \frac{U_{0\parallel}}{\Omega_c}\boldsymbol{b} \times \frac{d\boldsymbol{b}}{dt} \tag{A.30}$$

For a stationary magnetic field we get

$$\frac{d\boldsymbol{b}}{dt} = \gamma U_{0\parallel}(\boldsymbol{b} \cdot \boldsymbol{\nabla})\boldsymbol{b}. \tag{A.31}$$

Replacing this result in Eq. (A.30) gives,

$$\boldsymbol{U}_{1\perp} = \frac{\mu}{\gamma m \Omega_c}\boldsymbol{b} \times \boldsymbol{\nabla} B + \gamma\frac{U_{0\parallel}^2}{\Omega_c}\boldsymbol{b} \times (\boldsymbol{b} \cdot \boldsymbol{\nabla})\boldsymbol{b}. \tag{A.32}$$

In the absence of current in the trap, the second term can be rewritten using the identity,

$$\begin{aligned}(\boldsymbol{b} \cdot \boldsymbol{\nabla})\boldsymbol{b} &= \boldsymbol{\nabla}(\boldsymbol{b} \cdot \boldsymbol{b}) - \boldsymbol{b} \times (\boldsymbol{\nabla} \times \boldsymbol{b}) = -\boldsymbol{b} \times (\boldsymbol{\nabla} \times \boldsymbol{b}) \\ &= -\boldsymbol{b} \times \frac{1}{B}[\boldsymbol{\nabla} \times \boldsymbol{B} - \boldsymbol{\nabla} B \times \boldsymbol{b}] \\ &= \frac{\boldsymbol{\nabla}_\perp B}{B}.\end{aligned} \tag{A.33}$$

Therefore the drift velocity can be written as,

$$\boldsymbol{U}_{1\perp} = \gamma \frac{u^2/2 + U_{0\parallel}^2}{B\Omega_c} \boldsymbol{b} \times \boldsymbol{\nabla} B. \tag{A.34}$$

Appendix B

PROPERTY OF THE FOURIER COEFFICIENTS IN A SYMMETRIC TRAP

In a trap where the magnetic field distortion is symmetric with respect to the center of the trap, we expect the same amplitude of radiation to propagate in both directions in the waveguide. This means that we need to show that the coefficients in Eq. 3.56 satisfy

$$\left|a_n(-k_\lambda)\right|^2 = \left|a_n(k_\lambda)\right|^2. \tag{B.1}$$

Two useful expressions in symmetric traps assist us in deriving this relation. The first one is from the periodicity of the electron's position, z_0, in a symmetric trap, given by

$$-(z_0(t) - z_t) = z_0\left(t + \frac{T_a}{2}\right) - z_t, \tag{B.2}$$

in which z_t is the axial position of the center of the trap. Furthermore, a symmetric trap forces the cyclotron frequency to be periodic, with period equal to half of the axial motion's period. Therefore the cyclotron phase satisfies

$$\Phi_c\left(t + \frac{T_a}{2}\right) = \Omega_0 \frac{T_a}{2} + \Phi_c(t). \tag{B.3}$$

Utilizing Eq. (B.2) for $\Phi_c(t)$ and Eq. (B.3) to rewrite $k_\lambda z_0(t)$, we can write

$$\begin{aligned} \Phi_c(t) - k_\lambda z_0(t) = \Phi_c\left(t + \frac{T_a}{2}\right) - \Omega_0 \frac{T_a}{2} \\ + k_\lambda z_0\left(t + \frac{T_a}{2}\right) - 2k_\lambda z_t. \end{aligned} \tag{B.4}$$

Therefore we have

$$e^{i\Phi_c(t) - ik_\lambda z_0(t)} = e^{-i\Omega_0 \frac{T_a}{2} - 2ik_\lambda z_t} e^{i\Phi_c(t+\frac{T_a}{2}) + ik_\lambda z_0(t+\frac{T_a}{2})}. \tag{B.5}$$

Using Eq. (3.56), we expand the second exponent to get

$$\begin{aligned} e^{i\Phi_c(t)-ik_\lambda z_0(t)} &= e^{-2ik_\lambda z_t - i\Omega_0 \frac{T_a}{2}} \sum_{n=-\infty}^{\infty} a_n(k_\lambda) e^{i(\Omega_0+n\Omega_a)(t+\frac{T_a}{2})} \\ &= e^{-2ik_\lambda z_t} \sum_{n=-\infty}^{\infty} (-1)^n a_n(k_\lambda) e^{i(\Omega_0+n\Omega_a)t}. \end{aligned} \tag{B.6}$$

By equating the coefficients with those of the first expression in Eq. (3.58), we arrive at the form,

$$a_n(-k_\lambda) = (-1)^n e^{-2ik_\lambda z_t} a_n(k_\lambda), \tag{B.7}$$

which is consistent with our expectation of equal power propagating in both directions, since

$$|a_n(-k_\lambda)|^2 = |a_n(k_\lambda)|^2 . \tag{B.8}$$

Appendix C

$P_{0,\lambda}$ CALCULATION FOR TWO SPECIFIC WAVEGUIDE GEOMETRIES

The power amplitude, $P_{0,\lambda}$, was introduced in Eq. (3.61) as a measurement of an electron's coupling to a waveguide mode. The calculation details for two particularly relevant cases are shown here.

C.0.1 Rectangular waveguide TE_{10} mode

The first example is the fundamental mode of a rectangular waveguide. For such a waveguide, with w being its longer dimension (defined to be along the x axis) and h the smaller one (along the y axis), the electric field has the form

$$E_y(x) = K\cos\left(\frac{\pi x}{w}\right)\hat{y}. \tag{C.1}$$

Eq. (3.30) can now be used to find the normalization factor, giving

$$\int_{\mathcal{A}} K^2\cos^2\left(\frac{\pi x}{w}\right)\mathrm{d}x\mathrm{d}y = 1 \Rightarrow K = \sqrt{\frac{2}{wh}}. \tag{C.2}$$

With the normalized field, the expression for $P_{0,TE10}$ follows from the definition in Eq. (3.61) and is found to be

$$\begin{aligned} P_{0,TE_{10}} &= \frac{Z_{10}e^2v_0^2}{8}\left(\sqrt{\frac{2}{wh}}\cos\left(\frac{\pi x_c}{w}\right)\right)^2 \\ &= \frac{Z_{10}e^2v_0^2}{4wh}\cos^2\left(\frac{\pi x_c}{w}\right). \end{aligned} \tag{C.3}$$

C.0.2 Circular waveguide TE_{11} and TM_{01} mode

The second example to consider is that of a circular waveguide with radius R. The TE_{11} mode has the lowest cutoff frequency in a circular waveguide and the associated wavenumber is $k_c = \frac{1.841}{R}$. This mode consists of two degenerate modes for which the electric field can be found in [50],

$$\begin{aligned} E_{1\rho}(\rho,\phi) &= K\frac{-i\omega\mu}{k_c^2\rho}\cos(\phi)J_1(k_c\rho), \\ E_{1\phi}(\rho,\phi) &= K\frac{i\omega\mu}{k_c}\sin(\phi)J_1'(k_c\rho), \\ E_{1z}(\rho,\phi) &= 0 \end{aligned} \tag{C.4}$$

and

$$\begin{aligned} E_{2\rho}(\rho,\phi) &= K'\frac{-i\omega\mu}{k_c^2\rho}\sin(\phi)J_1(k_c\rho), \\ E_{2\phi}(\rho,\phi) &= K'\frac{i\omega\mu}{k_c}\cos(\phi)J_1'(k_c\rho), \\ E_{2z}(\rho,\phi) &= 0. \end{aligned} \tag{C.5}$$

The same technique is used to find the normalized fields,

$$\begin{aligned} 1 &= \int_{\mathcal{A}} \left[E_{1\rho}^2(\rho,\phi) + E_{1\phi}^2(\rho,\phi)\right] \rho \mathrm{d}\rho \mathrm{d}\phi \\ &= -K^2\pi\frac{\omega^2\mu^2}{2k_c^2}\int_0^R \left[\frac{J_1^2(k_c\rho)}{k_c^2\rho^2} + J_1'^2(k_c\rho)\right]\rho\mathrm{d}\rho. \end{aligned} \tag{C.6}$$

Hence the normalization factor can be found to be

$$K = K' = \frac{ik_c}{\omega\mu\sqrt{\pi\alpha}} \tag{C.7}$$

in which

$$\alpha = \int_0^R \left[\frac{J_1^2(k_c\rho)}{k_c^2\rho^2} + J_1'^2(k_c\rho)\right]\rho\mathrm{d}\rho \ = \frac{1}{2k_c^2}(p_{11}'^2 - 1)J_1^2(k_cR) \simeq \ 0.108858R^2. \tag{C.8}$$

The calculation of the coefficients $P_{0,TE_{11}}$ follows the rectangular waveguide calculation with one difference. That is, to find the power in the waveguide, the two degenerate modes' powers should be added together. This gives us

$$\begin{aligned} P_{0,TE_{11}} &= \frac{Z_{11}e^2v_0^2}{8}\left[E_{1\phi}^2 + E_{1\rho}^2 + E_{2\phi}^2 + E_{2\rho}^2\right] \\ &= \frac{Z_{11}e^2v_0^2}{8\pi\alpha}\left(J_1'^2(k_c\rho_c) + \frac{1}{k_c^2\rho_c^2}J_1^2(k_c\rho_c)\right). \end{aligned} \tag{C.9}$$

The TM_{01} mode is the second mode in a circular waveguide. The cutoff frequency for this mode is $k_c = \frac{2.405}{R}$ and the field components are

$$\begin{aligned} E_\rho(\rho,\phi) &= M\frac{-i\sqrt{k^2-k_c^2}}{k_c}J_0'(k_c\rho), \\ E_\phi(\rho,\phi) &= 0, \\ E_z(\rho,\phi) &= MJ_0(k_c\rho). \end{aligned} \tag{C.10}$$

The same normalization technique can be used to find the M constant

$$M = \frac{ik_c}{\sqrt{k^2-k_c^2}\mu\sqrt{2\pi\beta}}, \tag{C.11}$$

in which

$$\beta = \int_0^R J_0'^2(k_c\rho)\rho d\rho \simeq 0.426741R^2. \tag{C.12}$$

The coefficient $P_{0,TM_{01}}$ can now be calculated. We get

$$\begin{aligned} P_{0,Tm_{01}} &= \frac{Z_{11}e^2v_0^2}{8}E_\rho^2 \\ &= \frac{Z_{10}e^2v_0^2}{16\pi^2\beta}J_0'^2(k_c\rho). \end{aligned} \tag{C.13}$$

Appendix D

SIDEBAND ANALYSIS

The first phase of the project 8 experiment utilizes the rectangular waveguide for the gas cell. It also uses a reflector to gain better signal to noise ratios. The presence of this reflector causes the formation of interference patterns discussed in Chapter 3. Furthermore, the better signal to noise ratio makes it possible to detect secondary peaks in the form of sidebands. Mislabeling these tracks as the main track leads to incorrect electron energy measurement. In this appendix we discuss these tracks and the methods by which we can distinguish them from the main tracks.

D.1 Analyzing the CRES Data in the Presence of Sidebands

The sidebands are mainly detectable in bathtub trap geometry. In this section we discuss the conversion electron data from the K, L, and M shells of ^{83m}Kr atom recorded in a 1 Amps deep bathtub trap. The bathtub trap geometry is formed by applying currents to two separate trapping coils in a way that their field is parallel to the background field.

The frequency histogram recorded in the three frequency regions of interest is plotted in Fig. D.1. The plotted frequency histogram represents a complicated structure. It is obvious that converting these frequency measurements into energy values results in a drastically invalid energy measurement.

The constructed knowledge in Chapter 3 can assist us to interpret this data. The power and slope distribution is an effective way to start this analysis. Fig. D.2 illustrates the measured values of power and slope for electrons from the K, L, and M shells of ^{83m}Kr. The power-slope plots for the L and M shell electrons represent a clear structure in which three distinct batches can be seen. Plotting these different power-slope characteristics in the

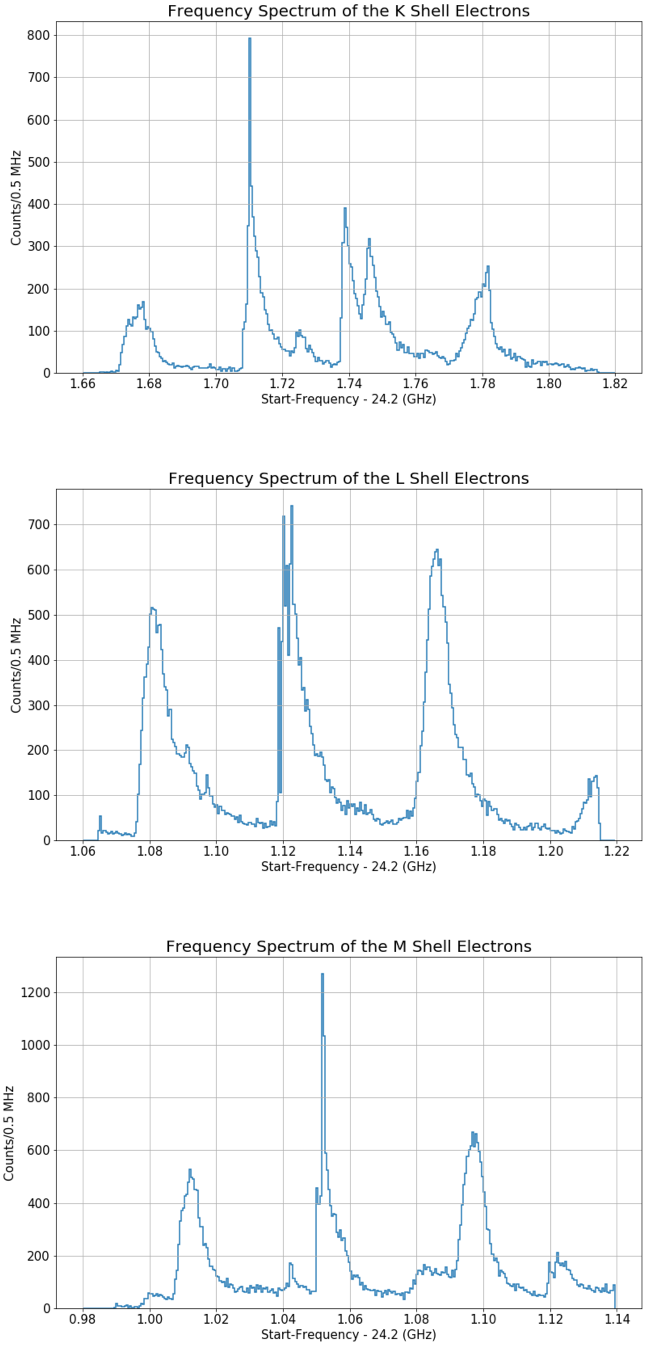

Figure D.1: Frequency histograms of the conversion electrons from the K, L, and M (upper, middle, and lower plots respectively) shells of the ^{83m}Kr.

frequency histogram helps to unravel the complexity in the spectrum.

Fig. D.3 illustrates these different batches of data in power-slope plot in the frequency histogram. The power vs. frequency plots in Fig. D.4 clearly links this data with the discussions presented in Chapter 3. As it was mentioned, electrons with higher pitch angle traverse in the lower field regions of the magnetic trap. Therefore the average magnetic field observed by them is lower compared with lower pitch-angle electrons. This results in a lower start frequency for higher pitch angles. In Sec. 3.2 we illustrate that the main track's power has also pitch angle dependency. The data presented in Fig. D.4 is consistent with the expected behaviour predicted in Sec. 3.2. The high pitch angle events (dark green in Fig. D.4, D.3, and D.4) have a smaller start frequencies. Decreasing the pitch angle decreases the main peak's power until it is no longer detectable. Further decrease in the pitch angle increases the power above the detectable floor. This causes the emergence of the second group of events with lower pitch angles and higher start frequencies (navy in Fig. D.4, D.3, and D.4).

Decreasing the pitch angle also enhances the power emitted into the secondary peaks which form the sidebands in the event spectrograms. Sidebands are tracks parallel to the main track with frequency separation which equals the axial frequency of electron motion inside the trap. The dark red dots in Fig. D.3 and Fig. D.4 indicate the events for which at least one sideband is detectable.

There are two more structures in the M shell plot in Fig. D.3 which needs further explanation. First there is a peak at 25.24 GHz which is the signature of the conversion electrons from the N shell of ^{83m}Kr atom. Moreover, the structure apparent at higher frequencies is the result of L shell conversion electrons which are detectable at the edge of the data acquisition window.

So far we successfully explained the spectral features of L and M shell conversion electrons. The structures caused by the conversion electrons from the K shell of the ^{83m}Kr atom need some further discussion. Note that the K shell electrons have the closest energy to the endpoint value of the tritium and hence have the most valuable features for study. The

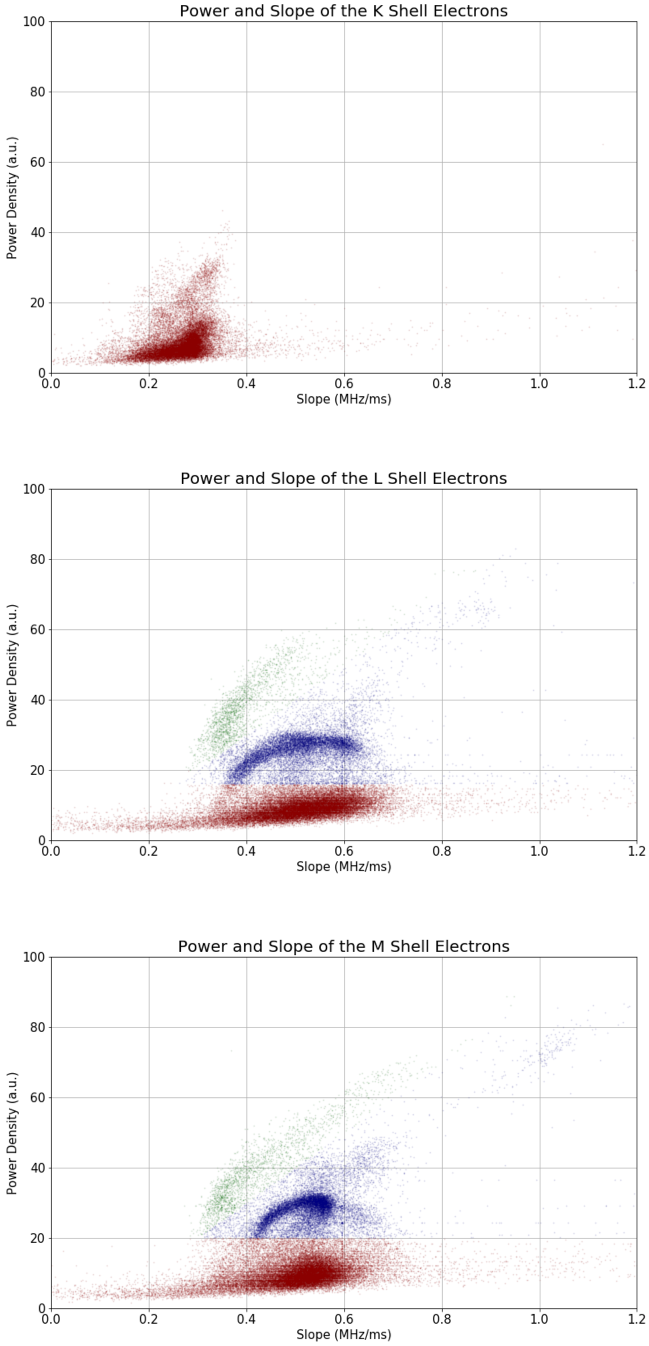

Figure D.2: Power-Slope plot of the conversion electrons from the K, L, and M (upper, middle, and lower plots respectively) shells of the ^{83m}Kr.

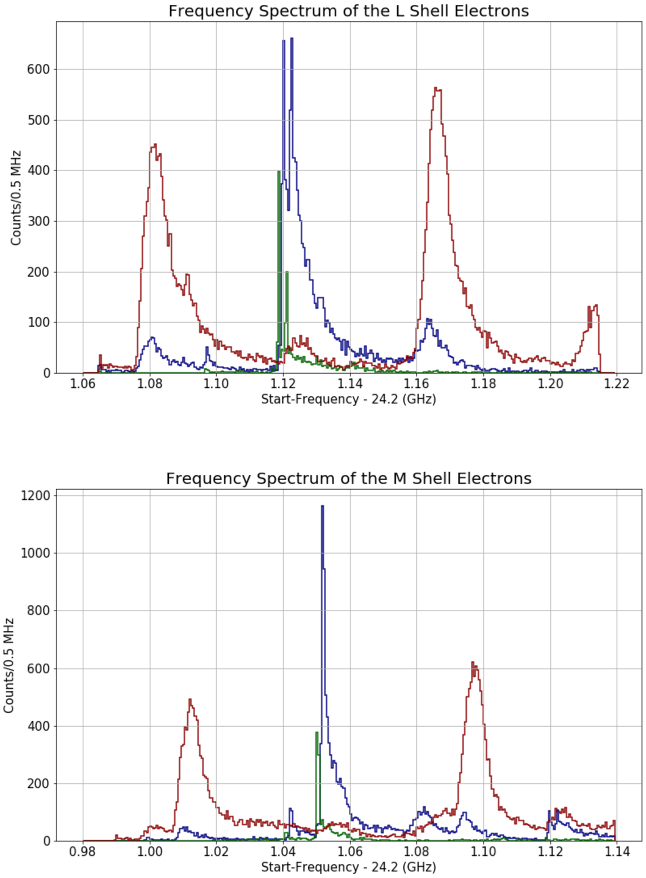

Figure D.3: Frequency histograms of the conversion electrons from the L and M (upper and lower plots respectively) shells of the ^{83m}Kr with different power-slope behaviour plotted separately. The color coding is similar to the one used in Fig. D.2.

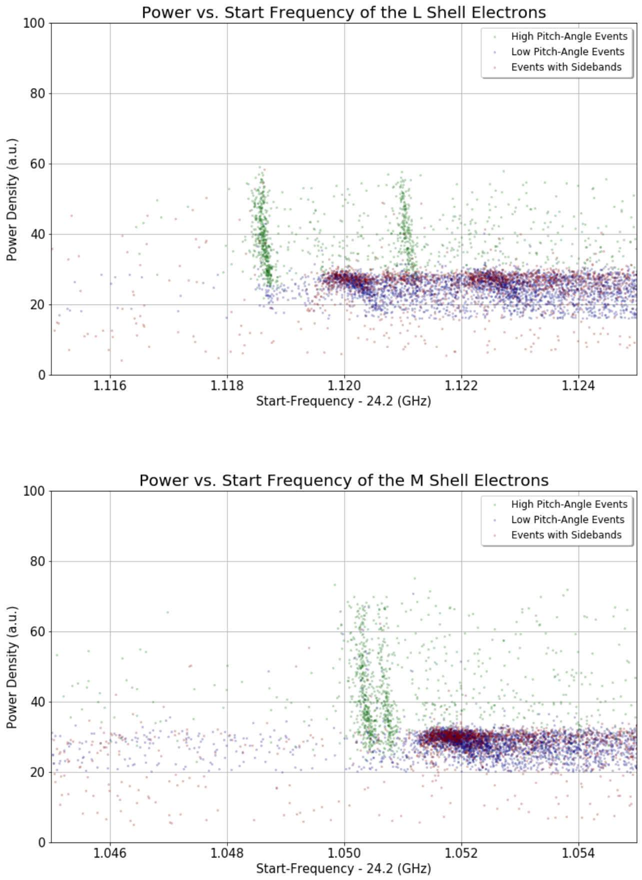

Figure D.4: Power density vs. frequency plot of the conversion electrons from the L and M (upper and lower plots respectively) shells of the ^{83m}Kr.

power-slope plot for the K shell electrons in Fig. D.2 does not represent the three distinct batches observable in power-slope plots of L and M shell electrons. The reason is that the main peak, for either high or low pitch angles, is not detectable for the K shell electrons. The interference pattern caused by the reflector, makes a destructive superposition of the radiated and reflected wave at the frequency of K shell electrons' main track. Therefore the frequency spectrum shown in Fig. D.1 is entirely made up of the sideband tracks. A more through study of this spectrum is presented in the next section.

At the end of this section, it should be considered that the algorithm for choosing different batches in the power-slope plots is an over-simplified model. A more sophisticated model based on machine learning algorithm is presented in [18].

D.2 Energy Resolution Using the High Pitch-Angle Electrons

As it was discussed, electron pitch angle has an effect on the observed start frequency of the tracks. Therefore, the pitch-angle variation would result in a broadening effect for the line shapes. Choosing high pitch angle electrons for which the start frequency shift is minimal can produce high resolution lines. We can use the power and slope information to choose the high pitch-angle events as it was discussed in the last section. Fig. D.5 presents the frequency histogram for the L and M shell electrons with a high pitch-angle cut. The fit performed in the histograms uses Voigt distributions with the Lorentzian width fixed to the values in Tbl. 4.1.

D.3 Explaining the Frequency Histogram of the K Shell Electrons

In Chapter 3 we showed that the secondary peaks in the CRES spectrum originate in electron's axial motion inside the trap. The frequency difference between these peaks, which manifest themselves in the form of parallel tracks in the spectrogram, is equal to the electron's axial motion. Electrons with different pitch angles have different axial motions and therefore different frequency spacing between their parallel tracks. The difference in the pitch angle modifies the distribution of power between the main track and its sidebands. For

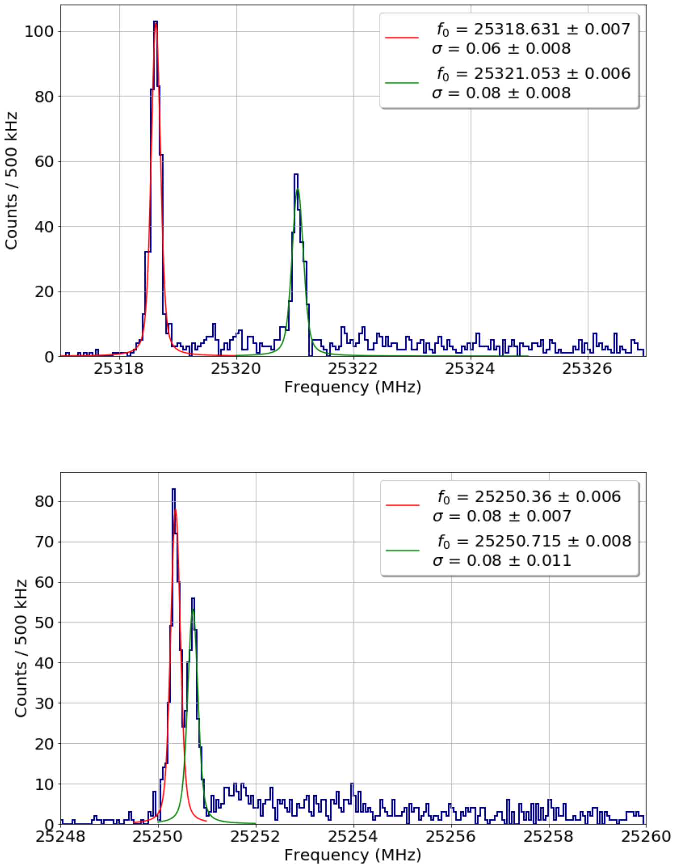

Figure D.5: Frequency histograms of the conversion electrons from the L and M (upper and lower plots respectively) shells of the ^{83m}Kr. The power and slope information is used to cut the electron events with high values of pitch-angle.

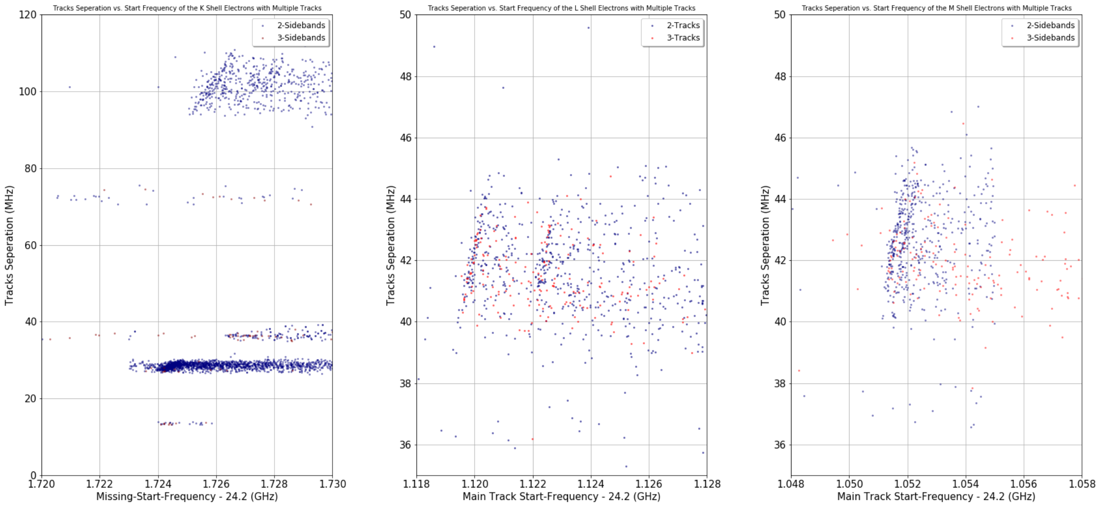

(a) K shell electrons (b) L shell electrons (c) M shell electrons

Figure D.6: Track separation vs. start-frequency for electron events with multiple tracks.

a range of pitch angle values, these sidebands are detectable above the noise level.

In a bathtub trap electrons with smaller pitch angles have a larger axial frequency. Fig. D.6 shows how this effect is represented in the data. In this plot the x-axis is the start-frequency of the main track, while the y-axis shows the track separation. Blue dots are the events with two tracks (main track and one sideband) and the red dots are the events with three parallel tracks (main track and two sidebands). Lower pitch angle electrons have a higher start frequency because they traverse inside a higher average field in the trap. Moreover, since these electrons have a higher axial frequency, they represent larger track separations. Hence, the electrons with higher start-frequencies have higher track separations in the bathtub trap. This can be clearly seen in Fig. D.6.

Since the main track for the K shell electrons cannot be detected due to the destructive interference caused by the RF reflector, the study of sidebands have a crucial role in their energy measurement. To investigate the complex spectrum of K Shell electrons, we use events with parallel tracks. Then we histogram these events based on the track separation in Fig. D.7.

There exist a small number of counts for which the main peak and the sidebands with track separation of approximately 13 MHz, are detectable (blue in Fig. D.7). These events are generated by electrons with large values of pitch-angle close to 90 degrees. For electrons with a slightly lower value of pitch angle, the two sidebands are detectable with a separation value of 30 MHz (orange in Fig. D.7). Decreasing the pitch angle reduces the power in this sidebands. Further decrease of the pitch-angle value makes the sidebands to reappear above the noise level. As a result of this decrease in the pitch angle, the axial frequency increases and therefore the track separation jumps to 37 MHz (green in Fig. D.7). For some events in this range of pitch angles, the detectable sidebands are not centered around the main peak. This explains the events with 37 MHz track separation which are at 1.67 GHz and 1.79 GHz in Fig. D.7. These sidebands are detected with the tracks at 1.71 and 1.75 GHz. The next group of events have track separation of 75 MHz (red in Fig. D.7). These events happen with the similar values of pitch-angle to the last group. Although instead of detecting two adjacent sideband, sidebands with more separations are observed. The last group are the tracks with 100 MHz separation. These sidebands are present at higher multiples of axial frequency. Fig. D.7 shows how these five groups construct the whole spectrum. Note that the spectrum has more counts than the sum of separated groups. That is due to the missing second tracks in most of the cases. However the structure in the spectrum is now fully understood.

Fig. D.6 shows these different groups in the plot representing track separation vs. start-frequency. The start-frequency is calculated by reconstructing the main track's position based on what we discussed. Fig. D.8 shows the frequency histogram for the conversion electrons from the K shell of ^{83m}Kr. The fit function is again a Voigt distribution with the Lorentzian width fixed to the value in Tbl. 4.1.

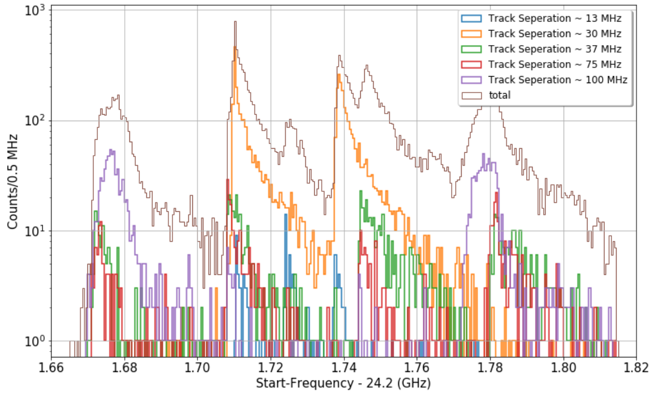

Figure D.7: Frequency histogram for the K shell electrons. Events with parallel tracks are plotted separately based on their track separation.

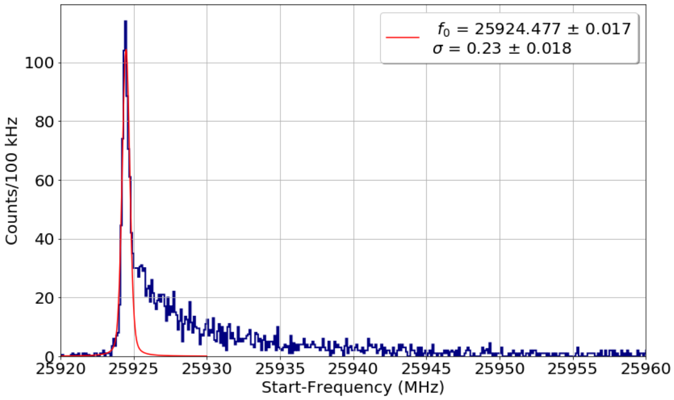

Figure D.8: Frequency histogram of the main track for K shell electrons. The frequency of the missing track is reconstructed based on the knowledge about the sideband tracks.

Appendix E

CONSTRUCTING A CHI-SQUARE FOR POINTS WITH ERRORS IN BOTH THE DEPENDANT AND INDEPENDENT VARIABLES

In this appendix we lay down a technique to construct chi-square that include the error in the independent variable [1]. We assume that the dependant variable y is related to the independent value x via,

$$y = f(x). \tag{E.1}$$

The uncertainty in y and x are respectively δy and δx. Using the Tailor series we have,

$$\begin{aligned} y + \delta y &= f(x_0) + \left(\frac{\mathrm{d}f}{\mathrm{d}x}\right)_{x=x_0} \delta x + \mathcal{O}(\delta x^2) \\ &= a_0 + a_1 \delta x + \mathcal{O}(\delta x^2). \end{aligned} \tag{E.2}$$

If we neglect the higher terms and assume that δx and δy are following multivariate Gaussian distribution with variances σ_x and σ_y and zero covariance, the chi-square can be written as,

$$\chi^2 = \sum_i \left(\frac{\delta x_i^2}{\sigma_{x_i}^2} + \frac{\delta y_i^2}{\sigma_{y_i}^2} \right). \tag{E.3}$$

To find the best fit the chi-square should be minimized subjected to the constraints,

$$g_i(\delta x_i, \delta y_i) = y_i + \delta y_i - a_{0i} - a_{1i}\delta x_i = 0. \tag{E.4}$$

To solve this optimization problem we use the Lagrange multipliers technique where,

$$\begin{aligned} \frac{\partial \chi^2}{\partial \delta x_i} + \sum_j \lambda_j \frac{\partial g_j(\delta x_j, \delta y_j)}{\partial \delta x_i} &= 0 \\ \frac{\partial \chi^2}{\partial \delta y_i} + \sum_j \lambda_j \frac{\partial g_j(\delta x_j, \delta y_j)}{\partial \delta y_i} &= 0, \end{aligned} \tag{E.5}$$

---

[1] This appendix follows closely the discussion presented in the 6th chapter of [16].

and λ_j are Lagrange multipliers. The partial derivatives in Eq. (E.5) can be easily calculated using Eq. (E.4),

$$\begin{aligned}\frac{\partial g_j(\delta x_j, \delta y_j)}{\partial \delta x_i} &= -a_{1i}\delta_j^i \\ \frac{\partial g_j(\delta x_j, \delta y_j)}{\partial \delta y_i} &= \delta_j^i.\end{aligned} \tag{E.6}$$

Therefore Eq. (E.5) can be rewritten as

$$\begin{aligned}2\frac{1}{\sigma_{x_i}^2}\delta x_i - a_{1i}\lambda_i = 0 \\ 2\frac{1}{\sigma_{y_i}^2}\delta x_i + \lambda_i = 0.\end{aligned} \tag{E.7}$$

Next δx and δy can be written in terms of the Lagrange multipliers,

$$\begin{aligned}\delta x_i &= \frac{1}{2}a_{1i}\sigma_{xi}^2\lambda_i \\ \delta y_i &= -\frac{1}{2}\sigma_{y_i}^2\lambda_i\end{aligned} \tag{E.8}$$

Replacing these values in Eq. (E.4) results in,

$$y_i - \frac{1}{2}\sigma_{y_i}^2\lambda_i = a_{0i} + a_{1i}\left(\frac{1}{2}a_{1i}\sigma_{x_i}^2\lambda_i\right). \tag{E.9}$$

Solving this equation gives the desired values of Lagrange multipliers,

$$\lambda = \frac{2}{\sigma_{y_i}^2 + a_{1i}^2\sigma x_i^2}(y_i - a_{0i}). \tag{E.10}$$

With the Lagrange multipliers, the error in x and y can be evaluated,

$$\begin{aligned}\delta x_i &= \frac{a_{1i}\sigma_{xi}^2}{\sigma y_i^2 + a_{1i}^2\sigma_{x_i}^2}(y_i - a_{0i}) \\ \delta y_i &= -\frac{\sigma_{yi}^2}{\sigma_{y_i}^2 + a_{1i}^2\sigma_{x_i}^2}(y_i - a_{0i})\end{aligned} \tag{E.11}$$

Finally the values of δx_i and δy_i can be replaced in Eq. (E.3) to find the Chi-square value,

$$\chi^2 = \sum_i \frac{1}{\sigma_{y_i}^2 + a_{1i}^2\sigma_{x_i}^2}(y_i - a_{0i})^2. \tag{E.12}$$